ASPECTS OF SOME NEW PHYSICS SCENARIOS
CONTAINING DARK MATTER

By
AVIRUP GHOSH

PHYS08201405003

Harish-Chandra Research Institute, Prayagraj

A thesis submitted to the

Board of Studies in Physical Sciences

In partial fulfillment of requirements

for the Degree of

DOCTOR OF PHILOSOPHY

of

HOMI BHABHA NATIONAL INSTITUTE

April, 2021

Homi Bhabha National Institute[1]

Recommendations of the Viva Voce Committee

As members of the Viva Voce Committee, we certify that we have read the dissertation prepared by Avirup Ghosh entitled "Aspects of some new physics scenarios containing Dark Matter" and recommend that it may be accepted as fulfilling the thesis requirement for the award of Degree of Doctor of Philosophy.

Chairman – Prof. Pinaki Majumdar		Date: 10-08-2021
Guide / Convener – Prof. Santosh Kumar Rai		Date: 10-08-2021
Examiner – Prof. Srubabati Goswami		Date: 10-08-2021
Member 1- Prof. Asesh Krishna Datta		Date: 10-08-2021
Member 2- Prof. Anirban Basu		Date: 10-08-2021
Member 3- Prof. Ujjwal Sen		Date: 10-08-2021
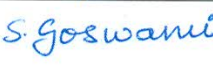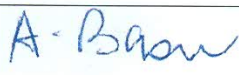
Final approval and acceptance of this thesis is contingent upon the candidate's submission of the final copies of the thesis to HBNI.

I/We hereby certify that I/we have read this thesis prepared under my/our direction and recommend that it may be accepted as fulfilling the thesis requirement.

Date: 10.08.2021
Place: Prayagraj

Prof. Santosh Kumar Rai
Guide

---

[1] This page is to be included only for final submission after successful completion of viva voce.

STATEMENT BY AUTHOR

This dissertation has been submitted in partial fulfillment of requirements for an advanced degree at Homi Bhabha National Institute (HBNI) and is deposited in the Library to be made available to borrowers under rules of the HBNI.

Brief quotations from this dissertation are allowable without special permission, provided that accurate acknowledgement of source is made. Requests for permission for extended quotation from or reproduction of this manuscript in whole or in part may be granted by the Competent Authority of HBNI when in his or her judgment the proposed use of the material is in the interests of scholarship. In all other instances, however, permission must be obtained from the author.

Avirup Ghosh

Avirup Ghosh

DECLARATION

I, hereby declare that the investigation presented in the thesis has been carried out by me. The work is original and has not been submitted earlier as a whole or in part for a degree / diploma at this or any other Institution / University.

Avirup Ghosh

Avirup Ghosh

List of Publications arising from the thesis

Journal

1. "Heavy stable charged tracks as signatures of non-thermal dark matter at the LHC : a study in some non-supersymmetric scenarios", Avirup Ghosh, Tanmoy Mondal, Biswarup Mukhopadhyaya, *JHEP*, **2017**, *12*, 136.

2. "Long-lived stau, sneutrino dark matter and right-slepton spectrum", Shankha Banerjee, Genevi`eve B'elanger, Avirup Ghosh, Biswarup Mukhopadhyaya, *JHEP*, **2018**, *09*, 143.

3. "Gamma-ray signals from multicomponent scalar dark matter decays", Avirup Ghosh, Alejandro Ibarra, Tanmoy Mondal, Biswarup Mukhopadhyaya, *JCAP*, **2020**, *01*, 011.

4. "Search for decaying heavy dark matter in an effective interaction framework: a comparison of γ-ray and radio observations", Avirup Ghosh, Arpan Kar, Biswarup Mukhopadhyaya, *JCAP*, **2020**, *09*, 003.

List of Publications not included in the thesis

Journal

1. "Right sneutrino with $\Delta L = 2$ masses as nonthermal dark matter", Avirup Ghosh, Tanmoy Mondal, Biswarup Mukhopadhyaya, *Phys. Rev. D*, **2019**, *99*, 035018.

2. "Asymmetric dark matter from semi-annihilation", Avirup Ghosh, Deep Ghosh, Satyanarayan Mukhopadhyay, *JHEP*, **2020**, *08*, 149.

Preprint

1. "Models of decaying FIMP dark matter : potential links with the Neutrino sector", Laura Covi, Avirup Ghosh, Tanmoy Mondal, Biswarup Mukhopadhyaya, arXiv : 2008.12550.

Conferences

1. Presented a talk "Non-thermal dark matter with stable charged particles: a study in some non-supersymmetric scenarios", SUSY, 2017, TIFR, Mumbai, India.

2. Presented a talk "Long-lived stau, sneutrino dark matter and reconstruction of right-handed slepton masses", XXIII DAE-BRNS HEP Symposium, 2018, IIT Madras, India.

Avirup Ghosh

Dedicated to

Ma, Baba and Didi

ACKNOWLEDGEMENTS

CONTENTS

SUMMARY

In this thesis we explore the phenomenological implications of some 'unusual' dark matter scenarios where the DM-visible sector interactions are suppressed either by a high-scale or ultra-small renormalizable couplings.

We consider two theoretical scenarios, each including a Z_2-odd sector and leading to an elementary dark matter candidate. The first one is a variant of the Type-III seesaw model where one lepton triplet is Z_2-odd, together with a heavy sterile neutrino. It leads to a fermionic dark matter, along with the charged component of the triplet being a quasi-stable particle which decays only via a higher-dimensional operator suppressed by a high scale. The second model consists of an inert scalar doublet together with a Z_2-odd right-handed Majorana neutrino dark matter. A tiny Yukawa coupling delays the decay of the charged component of the inert doublet into the dark matter candidate, making the former long-lived in the scale of collider detectors. The parameter space of each model has been constrained by big-bang nucleosynthesis, and also by the contribution to the relic density through freeze-out of the long-lived charged particle as well the freeze-in production of the dark matter candidate. We consider two kinds of signals at the Large Hadron Collider (LHC) for each of the scenarios and perform a detailed analysis using event selection criteria consistent with the current experimental programmes to estimate the required integrated luminosity for discovering such signals.

We contemplate the minimal supersymmetric (SUSY) standard model augmented by three right chiral sneutrinos ($\tilde{\nu}$MSSM) where one such sneutrino may serve as the lightest supersymmetric particle and a non-thermal dark matter candidate, especially if neutrinos have Dirac masses only. In such cases, if the lightest MSSM particle is a stau, the signal of SUSY at the LHC consists in stable charged tracks which are distinguishable from backgrounds through their time delay between the inner tracker and the muon chamber. We show how to determine in such scenarios the mass hierarchy between the lightest neutralino and right sleptons of the first two families up to 5-10% accuracy, using the techniques of neutralino reconstruction available in the literature.

We study a multicomponent scalar dark matter scenario, where novel gamma-ray signals may arise from the decay of the heavier dark matter component into the lighter via the decay $\phi_2 \to \phi_1 \gamma\gamma$ since the decay $\phi_2 \to \phi_1 \gamma$ is forbidden by the conservation of angular

momentum. We determine the width and photon energy spectrum generated in the decay, employing an effective theory approach, and in UV complete models where the scalar dark matter components interact with heavy or light fermions. We calculate limits on the inverse width from current data of the isotropic diffuse photon flux, both for a hierarchical and a degenerate dark matter spectrum followed by a brief discussion on the prospects of observing such diphoton signals from sneutrino decay in the minimal supersymmetric standard model extended with right-handed neutrino superfields ($\tilde{\nu}$MSSM).

Lastly we investigate and compare the possibilities of observing decaying dark matter (DM) in γ-ray and radio telescopes. The special emphasis of the study is on a scalar heavy DM particle with mass in the trans-TeV range. DM decays, consistent with existing limits on the lifetime, are assumed to be driven by higher dimensional effective operators. We consider both two-body decays of a scalar dark particle and a dark sector having three-body decays, producing two standard model particles. It is found that the Fermi-LAT data on isotropic γ-ray background provide the best constraints so far, although the CTA telescope may be more effective for decays where one or two photons are produced as primary decay products. However, in all cases, deeper probes of the effective operators are possible in the upcoming radio telescope SKA.

List of Figures

4

5

List of Tables

Chapter 1

Introduction

The hunt for the basic building blocks of nature had started with Rutherford's experiment and was succeeded by a number of experiments at different energy scales, ultimately leading to the current understanding, that all of the visible matter content of our universe is made up of a handful of sub-atomic particles. In addition, nearly 26% of the energy content of our universe is attributed to an invisible component called dark matter (DM) It is widely felt that such dark matter is constituted by some unknown elementary particle(s) which interact atmost weakly with the known constituents of the universe.' If so, then it is important to understand how do they interact with the known set of particles, which interact among themselves according to the Standard Model of particle physics.

1.1 The Standard Model of particle physics

The Standard Model (SM) of particle physics is by far the most complete description of nature with substantial experimental evidences in its favour [1–3]. The SM is an unified framework governing three fundamental interactions of nature, namely, strong, weak and electromagnetic interactions mediated by gluons (g), weak gauge bosons $(W^{\pm}, Z)$ and photon (γ), respectively. The requirements of Lorentz invariance and local gauge invariance dictate the form of the interactions among all the SM particles and the corresponding lagrangian, invariant under the SM gauge group $(\mathcal{G}_{\mathrm{SM}} = \mathrm{SU}(3)_{\mathrm{c}} \times \mathrm{SU}(2)_{\mathrm{L}} \times \mathrm{U}(1)_{\mathrm{Y}})$, can be expressed as:

$$\mathcal{L}_{\mathrm{SM}} = \mathcal{L}_{\mathrm{gauge}} + \mathcal{L}_{\mathrm{fermion}} + \mathcal{L}_{\mathrm{scalar}} + \mathcal{L}_{\mathrm{Yukawa}}. \tag{1.1.1}$$

- *Gauge sector:* The SM gauge fields, viz., gluons $(G^{a,\mu}$ with $a = 1, ..., 8)$, weak isospin gauge bosons $(W^{a,\mu}$ with $a = 1, 2, 3)$ and hypercharge gauge boson (B^{μ}), which con-

11

stitute the gauge sector of the SM, transform under the adjoint representations of the gauge groups $SU(3)_c$, $SU(2)_L$ and $U(1)_Y$, respectively. $\mathcal{L}_{gauge}$ in eqn. 1.1.1 contains only the SM gauge invariant kinetic terms for the gauge fields, quadratic in the corresponding field strength tensors, i.e.,

$$B^{\mu\nu} = \partial^\mu B^\nu - \partial^\nu B^\mu, \tag{1.1.2}$$

$$W^{a,\mu\nu} = \partial^\mu W^{a,\nu} - \partial^\nu W^{a,\mu} + g_W \epsilon^{abc} W^{b,\mu} W^{c,\nu}, \tag{1.1.3}$$

$$G^{a,\mu\nu} = \partial^\mu G^{a,\nu} - \partial^\nu G^{a,\mu} + g_s f^{abc} G^{b,\mu} G^{c,\nu}, \tag{1.1.4}$$

but no mass terms.

- *Fermion sector:* The fermionic sector of SM consists of six quarks and six leptons, divided into three generations in each case. In the quark sector, a left-chiral up-type quark (u_L) pairs up with a left-chiral down-type quark (d_L) of the same generation and transform as a $SU(2)_L$-doublet, while the right-chiral quarks of both up (u_R) and down (d_R) types transform as $SU(2)_L$-singlets. For the leptons, in each generation a left-chiral charged lepton (l_L) and the corresponding left-chiral neutrino (ν_L) constitute a $SU(2)_L$-doublet while the right-chiral charged lepton (l_R) of each generation transforms as a singlet under $SU(2)_L$-transformations. Thus the ith family of fermion can be grouped as:

$$Q_{i,L} = \begin{pmatrix} u_{i,L} \\ d_{i,L} \end{pmatrix}, u_{i,R}, d_{i,R}, L_{i,L} = \begin{pmatrix} \nu_{i,L} \\ l_{i,L} \end{pmatrix}, l_{i,R}. \tag{1.1.5}$$

The transformation properties under the $U(1)_Y$ gauge group are determined by the hypercharges (Y) of the $SU(2)_L$-doublet or singlet fermions which in turn dictate the corresponding electric charge, Q, via the relation, $Q = T_3 + Y$, where T_3 is the weak isospin quantum number associated with the fermion under consideration. For a fermionic doublet $T_3 = 1/2$ or $-1/2$ implying $Q = Y \pm 1/2$, while for a fermionic singlet $T_3 = 0$ and hence $Q = Y$. The transformation properties of the fermionic fields are tabulated in tab. 1.1. Unlike $SU(2)_L$, under $SU(3)_c$ both left as well as right-chiral components of each of the six quarks transform as a triplet while all the leptons transform as $SU(3)_c$-singlets. The chiral nature of $SU(2)_L$ gauge group prohibits any mass terms for the fermions and hence $\mathcal{L}_{fermion}$ in eqn. 1.1.1 represents only the corresponding kinetic terms which are invariant under $SU(3)_c \times SU(2)_L \times U(1)_Y$ transformations.

- *Scalar sector:* The scalar sector of the SM is composed of a complex scalar $SU(2)_L$-doublet Φ, with hypercharge $Y = 1/2$, which is a singlet under $SU(3)_c$ gauge group. Φ

Fields	Spin	$SU(3)_c \times SU(2)_L \times U(1)_Y$
$Q_{i,L} = \begin{pmatrix} u_{i,L} \\ d_{i,L} \end{pmatrix}$	1/2	(3, 2, 1/6)
$u_{i,R}$	1/2	(3, 1, 2/3)
$d_{i,R}$	1/2	(3,1,-1/3)
$L_{i,L} = \begin{pmatrix} \nu_{i,L} \\ l_{i,L} \end{pmatrix}$	1/2	(1 , 2 , -1/2)
$l_{i,R}$	1/2	(1 , 1 , -1)
$G_\mu^{1,2,3,4,5,6,7,8}$	1	(8 , 1 , 0)
$W_\mu^1, W_\mu^2, W_\mu^3$	1	(1 , 3 , 0)
B_μ	1	(1 , 1 , 0)
$\Phi = \begin{pmatrix} \phi^+ \\ \phi^0 \end{pmatrix}$	0	(1 , 2 , 1/2)

Table 1.1: Field content of the SM and corresponding gauge quantum numbers.

has four real degrees of freedom, one of which acquires a vacuum expectation value (*vev*) via the Higgs mechanism [4, 5], thereby causing the breakdown of $SU(2)_L \times U(1)_Y$ to $U(1)_{EM}$, which is a symmetry respected by the chosen vacuum $\langle \Phi \rangle$. When the gauge invariant kinetic terms for Φ, contained in $\mathcal{L}_{scalar}$, are expanded about the vacuum $\langle \Phi \rangle$, generate mass terms for some particular linear combinations of the electroweak gauge bosons $(W^{1,\mu}, W^{2,\mu}, W^{3,\mu}, B^\mu)$, namely, $W^{\pm,\mu} = \frac{1}{\sqrt{2}}(W^{1,\mu} \mp i\, W^{2,\mu})$ and $Z^\mu = \cos\theta_W\, W^{3,\mu} - \sin\theta_W\, B^\mu$, whereas the massless state $A^\mu = \sin\theta_W\, W^{3,\mu} + \cos\theta_W\, B^\mu$ is dubbed as photon (γ). On the other hand, three out of four real degrees of freedom of Φ behave as massless Goldstone bosons, while the remaining one degree of freedom emerges as a real massive scalar, higgs (h). The massless Goldstone bosons can be made to disappear by proper gauge choice while h is a physical state, recently discovered in the LHC [6].

It should also be noted that, the requirement of local gauge invariance forces one to write the kinetic terms for fermions as well as for Φ in terms of the corresponding

covariant derivatives,

$$D_\mu = \partial_\mu - ig_s \frac{\lambda^a}{2} G_\mu^a - ig_W \frac{\sigma^a}{2} W_\mu^a - ig_Y Y B_\mu, \qquad (1.1.6)$$

instead of ordinary derivatives. These are responsible for interaction of the matter sector with the gauge sector.

- *Yukawa sector:* Interactions among a left-chiral fermionic doublet $(Q_{i,L}, L_{i,L})$, a right-chiral fermionic singlet $(u_{i,R}, d_{i,R}, l_{i,R})$ and the $\mathrm{SU(2)_L}$-doublet scalar Φ or its conjugate $\tilde{\Phi} \equiv i\sigma_2 \Phi^*$ (with hypercharge $Y = -1/2$) are represented by $\mathcal{L}_{\mathrm{Yukawa}}$. It is the mere presence of Φ (or $\tilde{\Phi}$) that allows one to write interaction terms involving left and right-chiral components of a SM fermion in a gauge invariant way. After electroweak symmetry breaking (EWSB), i.e., $\mathrm{SU(2)_L} \times \mathrm{U(1)_Y} \to \mathrm{U(1)_{EM}}$, Dirac type mass terms proportional to $\langle \Phi \rangle$ are generated for the up and down type quarks as well as for the charged leptons. Neutrinos, on the other hand, still remain massless, due to the absence of any right-chiral counterpart. However, in view of the current evidences in favour of neutrino masses, the existence of right-handed neutrinos may turn out to be a reality, though, this does not significantly alter the structure or the phenomenology of the standard model. The off-diagonal nature of the Yukawa coupling matrices introduce mixings between different quark families which ultimately give rise to the CKM matrix governing inter-generation charged current interactions in the quark sector.

The field content of the SM is summarized in tab. 1.1.

Shortcomings of the Standard Model

In spite of its enormous success in predicting the outcome of several physical phenomena with unprecedented accuracy, the SM fails to elucidate certain unresolved issues of nature. For example, the Naturalness problem, existence of only three generations of chiral fermions and their mass hierarchy, observed matter-antimatter asymmetry of the universe are some of these issues which can not be explained within the purview of the SM and hence one is forced to look for physics beyond standard model (BSM). In addition, non-zero masses for the SM neutrinos and an eligible candidate contributing appreciably to the dark matter (DM) energy density of the universe, can not be realized within the framework of the SM.

The current understanding of the DM of our universe will be briefly discussed in the following section.

1.2 Dark matter of the universe

Various astrophysical as well as cosmological observations suggest that an appreciable fraction of the total energy density of our universe is attributed to an invisible form of matter, known as dark matter (DM). For example,

(i) F. Zwicky studied the velocity of galaxies inside the galaxy cluster Coma, which is a stable bound system and expected to obey the Virial theorem. Assuming the Coma cluster to be spherical and applying Virial theorem to it, Zwicky realized that the galaxies move too fast compared to what is expected from its luminous matter content [7] which should have destabilized the cluster unless a large amount of non-luminous matter is present within it.

(ii) According to Newton's law the centripetal force on the stars rotating a galaxy is provided by the gravitational attraction and consequently the velocity is expected to decrease as the radial distance increases beyond the periphery of the visible part of the galaxy. However, the measured radial velocity distribution of stars orbiting a galaxy was found to approach a constant value for larger distances from the center of the galaxy [8]. A possible explanation for such a trend of the galactic rotation curve at large distances is provided by assuming the visible part of the galaxy to be immersed in a bigger halo of dark matter with a density profile decreasing as inverse square of the distance, so that even if one recedes from the luminous part, the mass contained within a sphere of a given radius increases linearly with the radius, thereby keeping the velocity constant.

(iii) The observation of Bullet cluster [9], which is a system of two colliding clusters, is considered to be the strongest evidence in favour of DM. The X-ray emission from the hot intra-cluster gas is used to determine the distribution of luminous matter inside the cluster while the total mass distribution is inferred using gravitational lensing. A study of these distributions suggest that the luminous parts of the two subclusters interact while crossing but the non-luminous components pass through each other without any appreciable interactions thereby pointing towards the collisionless nature of the non-luminous DM.

(iv) Although DM does not interact directly with the cosmic soup of photons, gravitational interactions of DM with the baryons leave their footprints in the Cosmic Microwave Background (CMB) during recombination which are manifested in the CMB angular power spectrum. Moreover, estimates of baryonic matter density as well as total matter density as obtained from the peaks of CMB power spectrum give most accurate estimate of the DM density of our universe [10].

(v) The observed matter power spectrum, a measure of the matter density distribution of

our universe, can be correctly reproduced only in presence of DM [11]. This is yet another evidence in favour of the existence of DM.

Given the above-mentioned observations, supporting the presence of DM in both galactic as well as cosmological scales, it is an interesting proposal that the DM of our universe is a particle. If it is indeed a particle, then it has to be massive, electrically neutral and also non-baryonic. Simulations of structure formation show that the DM particle has to be 'cold', i.e., non-relativistic when matter energy density starts to dominate over the radiation energy density of our universe, which in turn also implies that the DM mass must be greater than a few keV if it had a thermal origin [12, 13]. In addition, DM also has to be stable or must have a lifetime larger than the age of the universe and should correctly reproduce the observed relic density. It is intriguing that the SM can not provide a viable cold dark matter candidate for our universe and compels one to think of scenarios beyond standard model.

All the evidences of the DM, obtained till date, bear only the information about its gravitational interactions. However, if the DM is a particle then it is equally important to know how it interacts with the visible particles, other than through gravity. This is because such interactions not only govern the production mechanism of the DM candidate in the early universe, but also determine its present day signatures. One should note that, the non-luminous and non-baryonic natures of the DM particle forbid its couplings to photon and gluon, respectively. However, it can interact with the weakly interacting particles of the SM. In fact, it was realized long ago that such a particle with $\sim$GeV-TeV scale mass and electroweak scale couplings to the SM particles can satisfactorily reproduce the observed relic density of cold dark matter and is known as *Weakly Interacting Massive Particle* (WIMP).

1.2.1 WIMP paradigm

WIMPs are the most widely studied candidates for the DM of our universe [14, 15]. Due to their weak scale interaction strengths with the SM particles they remain in thermal equilibrium in the early universe via the scatterings, $\chi\chi \to \text{SM SM}$, where χ refers to the WIMP candidate of mass m_χ and SM represents a standard model particle lighter than χ. As long as χ is relativistic, both the forward as well as the backward reaction rates are equal, thereby maintaining the comoving number density of χ to a constant value. As soon as the temperature of the universe drops below m_χ, i.e., $T \lesssim m_\chi$, SM particles do not have enough kinetic energy to produce χ and hence the backward reaction stops which causes the comoving number density of χ to decrease. At an even smaller temperature, called the *freeze-out* temperature (i.e., $T_f \simeq m_\chi/20$), the forward reaction rate drops below the Hubble

expansion rate (H) of the universe, as a result of which the comoving number density of χ freezes, ultimately leading to the observed relic density of the DM χ. The evolution of χ number density (n_χ) is governed by the Boltzmann eqn:

$$\frac{dn_\chi}{dt} + 3Hn_\chi = -\langle \sigma v \rangle_{\chi\chi \to \text{SM SM}} \left(n_\chi^2 - n_{\chi,\text{eq}}^2 \right), \tag{1.2.1}$$

where $\langle \sigma v \rangle_{\chi\chi \to \text{SM SM}}$ is the thermally averaged cross-section for the process $\chi\chi \to \text{SM SM}$ and $n_{\chi,\text{eq}}$ refers to the equilibrium number density of χ, which is given by the Maxwell-Boltzmann distribution. On solving eqn. 1.2.1, one obtains the relic density $(\Omega_\chi h^2)$ of χ as a function of m_χ and $\langle \sigma v \rangle_{\chi\chi \to \text{SM SM}}$. However, it is interesting to note that $\Omega_\chi h^2$ depends only mildly on m_χ and the correct relic density, i.e., $\Omega_\chi h^2 = 0.12$, is obtained for $\langle \sigma v \rangle_{\chi\chi \to \text{SM SM}} \simeq 3 \times 10^{-26} \, \text{cm}^3/\text{s}$. Surprisingly, such a value of $\langle \sigma v \rangle_{\chi\chi \to \text{SM SM}}$ matches with the weak scale cross-section of a particle of mass $\sim 100 \, \text{GeV}$, which justifies the name WIMP miracle.

Examples of WIMP DM

Being the most popular candidate for the cold dark matter of our universe, there exists numerous examples of WIMPs in the literature. Generically, it is conceivable that such a WIMP candidate can either be a SM singlet or non-trivially charged under the electroweak gauge group, still being electrically neutral. For example,

- *SM singlet :* If the DM particle is a SM singlet scalar (χ) or fermion (ψ) [1], odd under an imposed Z_2 symmetry, it can couple to the SM sector via the higgs (h) [18,19] or the Z-boson [20]. The DM χ couples to higgs via the renormalizable quartic interaction $\lambda_\chi^h \chi^* \chi \, \Phi^\dagger \Phi$, while in the fermionic case such an interaction is only generated at the dimension-5 level, i.e., $\frac{\lambda_\psi^h}{\Lambda} \bar\psi\psi \, \Phi^\dagger \Phi$. After EWSB, interaction terms of the form DM-DM-h are generated in both the cases and the DM interacts with the SM fermions as well as the gauge bosons via h-mediated Feynman diagrams. In a similar spirit, a SM singlet DM can also interact with the SM sector particles via Z-boson exchange. The required DM-DM-Z couplings are generated from the dimension-6 interaction terms of the forms $\frac{\lambda_\chi^Z}{\Lambda^2} \Phi^\dagger \overleftrightarrow{D}_\mu \Phi \, \chi^* \overleftrightarrow{\partial}_\mu \chi$ (for scalar DM) or $\frac{\lambda_\psi^Z}{\Lambda^2} \Phi^\dagger \overleftrightarrow{D}_\mu \Phi \, \bar\psi\gamma^\mu(a + b\gamma_5)\psi$ (for fermionic DM), after EWSB.

- *Electroweak multiplet :* In principle, DM can be the neutral component of a scalar or a fermionic multiplet, non-trivially charged under the $\text{SU}(2)_\text{L} \times \text{U}(1)_\text{Y}$ gauge group. For example, refs. [21,22] have shown that the neutral component of either a fermionic

---

[1]In principle, fields with higher spins can also serve as the DM candidate of our universe [16,17]. However, we shall abstain from discussing such DM candidates in this thesis.

$SU(2)_L$ quintuplet with a mass $m_{DM} \simeq 4.4\,\text{TeV}$ or a scalar $SU(2)_L$ septuplet with a mass $m_{DM} \simeq 8.5\,\text{TeV}$, can serve as the DM candidate with $Y = 0$ in both the cases. The DM relic density in these cases are determined via the co-annihilations of the DM candidate with the charged partners belonging to the same multiplet, nearly degenerate in mass.

Moreover, the DM candidate can also be a suitable admixture of a SM singlet and the $Q = 0$ component of an electroweak multiplet (for instance, see [23]).

Results of WIMP searches

Since WIMPs have appreciable interactions with the SM particles, they are expected to leave observable signatures in various experiments. There exists three extensively used strategies to detect them:

- *Direct detection :* As Earth moves through the Milky Way halo, filled with WIMP DM particles [24], nuclei of the terrestrial detectors are expected to get bombarded with these DM particles. The DM particles while elastically scattering off these nuclei transfer certain amount of momentum to them, leading to nuclear recoil events, observations of which can be used to establish the particle nature of DM. Such detection strategy is known as direct detection of dark matter and several experiments, e.g., XENON [25], LUX [26], PandaX [27], DarkSide [28], CRESST [29], have been set worldwide to detect WIMPs using this technique. These detectors are usually placed deep underground in order to eliminate the backgrounds caused by the cosmic-ray particles. DM particles on the other hand, having negligible interactions pass through the Earth and hit such detectors. DM scattering against the nucleus can occur via scalar or vector couplings (i.e., spin independent interactions) as well as via axial couplings (i.e., spin dependent interactions) to the nucleons, depending on the DM model considered. Existing upper-limits on the DM-nucleon spin independent cross-section is shown in fig. 1.1 as a function of the DM mass. One can clearly see from fig. 1.1 that the strongest upper-limit on the spin-independent DM-nucleon scattering cross-section for WIMP masses in the range $\sim 10\,\text{GeV} - 1\,\text{TeV}$ is offered by XENON experiment. Additionally, it should also be noted that the constraints weaken significantly for WIMP masses below ~ 10 GeV and also while approaching a TeV. The decrease in the local number density of DM particles for higher DM masses causes drastic reduction in the number of signal events and hence the corresponding limit weakens. On the other hand, such a loss of sensitivity for lower DM masses is due to the fact that the energy of the
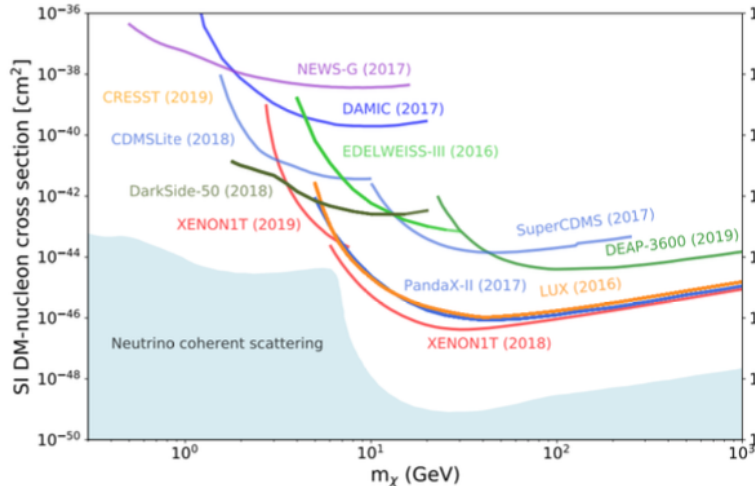
Figure 1.1: Upper-limits on the DM-nucleon spin independent cross-section as a function of DM mass. Figure is taken from internet.

recoiled nucleus is too small to overcome the threshold energy required for detection. However, for lower mass ranges (i.e., below $\sim 10\,\mathrm{GeV}$) relevant limits are offered by the experiments with comparatively lower energy thresholds, like DarkSide, CRESST etc. In fig. 1.1 the light blue region represents the irreducible background arising from neutrino-nucleus coherent scattering. In case of DM-proton spin dependent scattering most stringent limit till date is posed by PICO [30] while for DM-neutron spin dependent scattering XENON1T provides the strongest constraint; see ref. [31] for recent compilations on direct search limits of WIMP DM.

- *Indirect detection :* As discussed earlier, the thermal evolution of WIMP DM relies upon the assumption that DM annihilates substantially to SM particles. Based on this assumption, it is expected that the stable detectable particles (i.e., γ, ν, $e^{\pm}$, $p/\bar{p}$) produced from the primary products of DM annihilations in the highly dense regions of the galaxies would leave their signatures in the terrestrial detectors. In particular, γ-rays are simple to observe since they travel along straight lines between the source and the observer, thereby keeping the spectral information of the associated γ-ray source intact. Several space-based (e.g., Fermi-LAT [32], INTEGRAL [33], AGILE [34]) as well as ground-based (e.g., HESS [35], VERITAS [36], MAGIC [37]) gamma-ray observations have provided important information regarding the properties of WIMP annihilations in last two decades. For example, Fermi-LAT observation of Milky Way

19
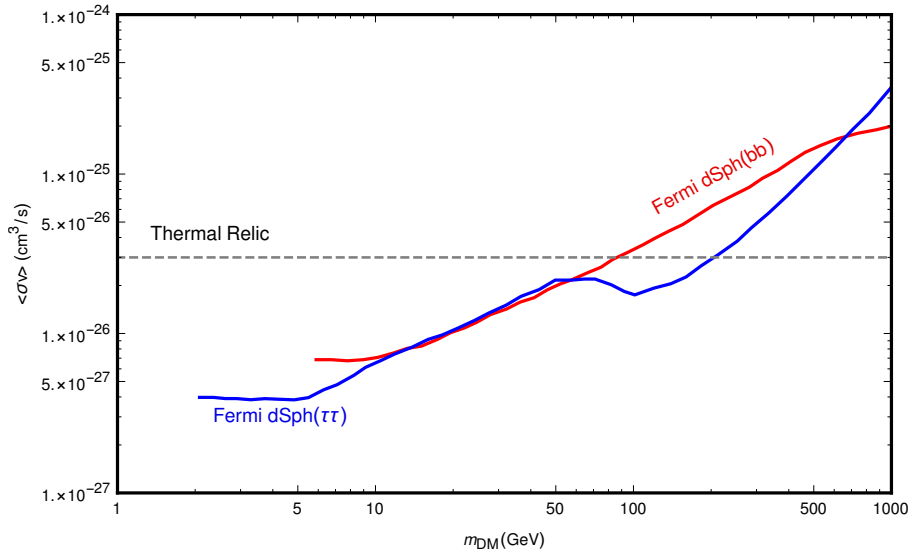
Figure 1.2: Constraints obtained from Fermi-LAT observation of dSph [32] in the DM annihilation cross-section vs. DM mass plane.

dwarf spheroidal galaxies (dSphs) have put strong constraints on the DM annihilation rate ($\langle \sigma v \rangle$) for $\sim 1\,\mathrm{GeV}$- $1\,\mathrm{TeV}$ DM masses (m_{DM}). In fig. 1.2, we have shown the limits obtained by analyzing Fermi-LAT dSph data, for DM annihilations in the channels $b\bar{b}$ and $\tau^+\tau^-$. As can be clearly seen the thermal relic cross-section $\langle \sigma v \rangle \sim 3 \times 10^{-26}\,\mathrm{cm^3 s^{-1}}$ is ruled out for $m_{\mathrm{DM}} \lesssim 100\,\mathrm{GeV}$ when DM annihilations occur dominantly in the $b\bar{b}$ or $\tau^+\tau^-$ channels. Searches for anti-matter particles, like e^+, $\bar{p}$, though subjected to uncertainties related to the propagation parameters, e.g., diffusion coefficient, energy loss rates, several cosmic-ray experiments, PAMELA [38], AMS-02 [39, 40] etc., have measured the $p/\bar{p}$-ratio as well as the positron fraction with fairly high accuracy and provided limits on the $\langle \sigma v \rangle - m_{\mathrm{DM}}$ plane, which are competitive with the constraints obtained from γ-ray observations.

- *Collider searches :* A complementary search strategy for WIMP DM is to produce them inside colliders. Unlike visible particles, WIMPs, when produced inside the colliders, leave no observable signature due to their insignificant interaction strengths with the detector materials. The only possible way to ascertain the production of such WIMP particles is to study the accompanying visible final state particles. In particular, the transverse missing energy ($\not{E}_T$), defined as the magnitude of the unbalanced total transverse momenta (p_T) of all the visible final state particles produced in asso-
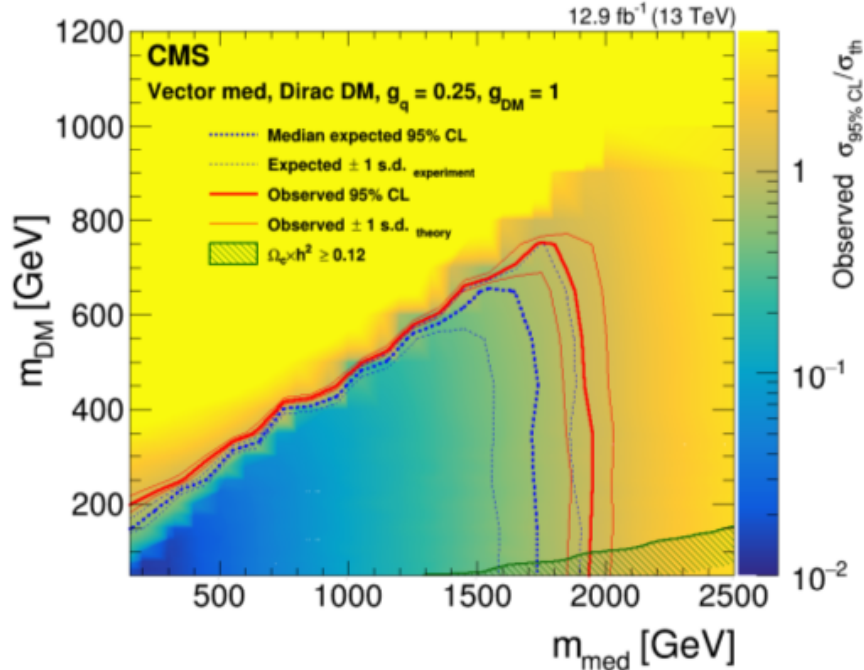
Figure 1.3: LHC constraints in the DM mass vs. vector mediator mass plane. Figure is taken from [41].

ciation with the WIMP, has been proven to be a good discriminator in the context of hadronic colliders, e.g., Tevatron, Large Hadron Collider (LHC). In LHC, the presence of a WIMP particle is usually searched for in the events with final state $\not{E}_T + X$, where X represents a QCD jet produced from initial state radiation (ISR), Z, h or γ. Requirement of high $\not{E}_T$ and high p_T jets are used to distinguish potential $\not{E}_T$+jets signals of WIMPs from SM backgrounds, e.g., $Z(\nu\bar{\nu})$+jets, $W(l\nu)$+jets. Non-observations of any excesses of events over the expected SM backgrounds are used to constrain the parameter space of the relevant DM model. For example, one such result provided by the CMS experiment is shown in fig. 1.3, which corresponds to a p-p collision with 13 TeV center-of-mass energy and $12.9\,fb^{-1}$ of integrated luminosity. The DM production considered here, occurs via the mediation of a vector mediator which couples to quarks (with coupling $g_q = 0.25$) on one side, while to the WIMPs (with coupling $g_{DM} = 1$) on the other. The exclusion region obtained by requiring $\not{E}_T > 200\,\text{GeV}$ and $p_T^{jet} > 100\,\text{GeV}$, in the parameter space spanned by the DM mass (m_{DM}) and the mediator mass (m_{med}), is bounded by the red solid line in the center, while other red lines indicate associated 1σ theoretical uncertainty. From fig. 1.3, it can be clearly

inferred that for an electroweak scale WIMP (i.e., $m_{\mathrm{DM}} \sim 200\,\mathrm{GeV}$) a vector mediator as heavy as $\sim 2\,\mathrm{TeV}$ is ruled out. Such exclusion plots for other mediators (e.g., axial vector, scalar, pseudo scalar) [41] and for different visible final state particles [42, 43] are also available. Additionally, if WIMP mass is lower than half of the higgs mass or that of the Z-mass, then the corresponding invisible decay width of h or Z can also be used to put limits on the DM parameters [44, 45].

All in all, though WIMPs as the possible candidates for DM of our universe is not completely impossible, they are not as probable as one would have thought a few years ago. Therefore, one should think of alternative candidates eligible for serving as DM.

1.2.2 Alternatives to WIMPs

A few non-WIMP DM candidates, which have gained popularity in recent times, are summarized below:

- *Strongly Interacting Massive Particles (SIMP)* : SIMP refers to a scenario where the DM abudance in today's universe is set by 3DM $\rightarrow$ 2DM annihilations in the DM sector [46] instead of DM + DM $\rightarrow$ SM + SM annihilations, as in the case of WIMPs. However, similar to the case of WIMPs, here, too, the DM remain in kinetic equilibrium with the SM plasma via elastic scattering processes, i.e., DM + SM $\rightarrow$ DM + SM, during freeze-out, so that the DM distribution still follows the Maxwell-Boltzmann distribution. Such a hierarchy among different scattering rates can be easily achieved by setting the DM self-interaction coupling larger than the DM-SM couplings. Smallness of the DM-SM couplings, though suppress the $2 \rightarrow 2$ annihilations of the DM, the elastic scattering rate is larger due to the higher abundance of SM particles during freeze-out. Such scenarios suggest a MeV scale thermal DM with DM-SM coupling $\lesssim 10^{-6}$ but with $\mathcal{O}(1)$ self-interaction coupling.

- *ELastically DEcoupling Relic (ELDER)* : In the ELDER scenarios, similar to the case of SIMPs, the $2 \rightarrow 2$ DM pair-annihilations are suppressed, while the DM + SM $\rightarrow$ DM + SM elastic scattering processes decouple earlier than the 3DM $\rightarrow$ 2DM self-scatterings [47]. Therefore, the thermal contact between the DM sector and the SM sector is lost prior to the decoupling of the DM self-scatterings which maintains the chemical equilibrium in the dark sector. In this epoch, 3DM $\rightarrow$ 2DM processes inject entropy to the dark sector thereby causing a slower rate of decrease of the temperature

of the DM sector, which is known as 'cannibalization'. Since the dark sector temperature, set by the decoupling of the elastic scatterings, dictates the DM number density, the relic density, too, strongly depends on the rate of these elastic scatterings. Such scenarios also predict DM particles of $\mathcal{O}(\text{MeV})$ masses but with larger self-interactions and even smaller DM-SM interactions compared to SIMPs.

- *Feebly Interacting Massive Particles (FIMP) :* FIMP paradigm represents the class of scenarios where DM particle is assumed to be out-of thermal equilibrium through out the evolution of the universe [48]. DM production in such cases occur either from the decay or scattering of heavier particles present in the spectrum, which themselves remain in thermal equilibrium with the SM plasma. One usually start with negligible abundance of the DM in the early universe, and DM production dominantly occurs either around the thermal decoupling of the parent species (known as IR freeze-in) or the hightest temperature, i.e., reheating temperatiure (T_R), of the SM plasma (called UV freeze-in). In these class of scenarios, the requirement of correct relic density constrains DM-visible sector couplings to $\lesssim 10^{-9}$ while the DM mass is rather unconstrained.

Although this is only a small subset of the plethora of non-WIMP DM models, one common feature of all the aforementioned DM scenarios is the smallness of the DM-SM interaction strengths, which in turn helps these scenarios to evade the direct, indirect and collider search bounds, discussed in the previous section.

Chapter 2

Feebly interacting dark matter

As mentioned in chapter 1, though WIMPs are the most attractive candidates accounting for the dark matter energy density of the universe, all terrestrial and extra-terrestrial efforts of detecting such DM candidates have gone in vain, till date [25, 32, 49–51]. Therefore, it is imperative to think of alternative scenarios, where dark matter particles interact only very weakly with the visible sector particles. Strongly interacting massive particles (SIMPs) [46], feebly interacting massive particles (FIMPs) [48] etc. have thus gained attention in recent times. In this thesis we shall concentrate on the FIMP paradigm and their possible signatures in collider as well as astrophysical experiments.

2.1 Freeze-in production of dark matter

In contradiction to SIMP scenarios, where DM particles interact *strongly* with the dark sector particles and thus thermalise within the dark sector itself, FIMP frameworks are based on the assumption that DM particles interact *superweakly* with all the particles present in the spectrum. Thus such FIMP candidates never reach thermal equilibrium during the evolution of the universe. In general, the production of FIMP DM candidates takes place from the decay of heavier particles present in the spectrum, which themselves may have larger interaction strength with the SM sector and thus remain in thermal equilibrium. As an example, let us consider a scenario where the FIMP DM χ is produced from the decay $A \to B\,\chi$, where A and B are either interacting appreciably with the SM or they themselves belong to the SM particle spectrum. The evolution of χ number density n_χ is governed by

the Boltzmann eqn.,

$$\dot{n}_\chi + 3\,H\,n_\chi = \int d\Pi_\chi\, d\Pi_A\, d\Pi_B (2\pi)^4 \delta^4\,(p_\chi + p_B - p_A)$$
$$\left[|\mathcal{M}|^2_{A \to B\chi} f_A(1 \pm f_B)(1 \pm f_\chi) - |\mathcal{M}|^2_{B\chi \to A} f_B f_\chi (1 \pm f_A) \right], \quad (2.1.1)$$

with the Hubble parameter $H(T) = \sqrt{\pi^2/90}\, g_*^{1/2}\, T^2/M_{\mathrm{Pl}}$ [52], where T is the temperature of the thermal bath, g_* is the relativistic degrees of freedom in thermal equilibrium and M_{Pl} is the Planck mass. Usually it is assumed that the χ density is small enough during the evolution of the universe and thus the backward reaction can be neglected in the r.h.s of eqn. 2.1.1. Additionally, we also assume $(1 \pm f_B), (1 \pm f_\chi) \simeq 1$ to obtain,

$$\frac{dY_\chi}{dx} = \frac{106.72}{\pi^5} \frac{g_A}{g_*^{3/2}} \left(\frac{M_{\mathrm{Pl}}\, \Gamma_{A \to B\chi}}{m_A^2} \right) x^3\, K_1(x), \quad (2.1.2)$$

where we have used $Y_\chi = n_\chi/s$, $x = m_A/T$, g_A is the number of degrees of freedom of A and $f_A \simeq e^{-E_A/T}$, i.e., A remains in thermal equilibrium. In the definition of the yield variable Y_χ we have used $s(T) = (2\pi^2/45)g_*\, T^3$, the comoving entropy density of the universe. Integrating eqn. 2.1.2 from $x_{min} = 0$ to $x_{max} = \infty$ one obtains,

$$Y_\chi = 1.64 \times \frac{g_A}{g_*^{3/2}} \times \left(\frac{M_{\mathrm{Pl}}\, \Gamma_{A \to B\chi}}{m_A^2} \right), \quad (2.1.3)$$

which gives the freeze-in relic density as follows,

$$\Omega_{FI} h^2 = 1.09 \times 10^{27} \frac{g_A}{g_*^{3/2}} \times \left(\frac{m_\chi\, \Gamma_{A \to B\chi}}{m_A^2} \right). \quad (2.1.4)$$

From Eqn. 2.1.4 one finds that for $g_A = 1$, $m_A = 1\,\mathrm{TeV}$ and $m_\chi = 1\,\mathrm{GeV}$, correct relic density requires $\Gamma^{-1}_{A \to B\chi} \simeq 5.43\,\mu s$, which clearly suggests that if the only decay mode of A is into χ, then A is fairly long-lived. Moreover, such a small decaywidth is necessarily a consequence of a small coupling between A and χ. In passing we would like to mention that in principle scattering of particles in thermal bath may also produce FIMP DM χ when the stabilising symmetry does not allow any decay process which dominates the χ production (see ref. [48] for details).

Till now we have calculated the abundance of χ produced from the decay of particles in thermal equilibrium, such as A. In principle, A will freeze-out as soon as the scattering processes which keep it in equilibrium fail to compete against the expansion rate of the universe. The frozen-out abundance of A also decays afterwards to produce χ. This *superweak* contribution to χ relic density is estimated as [53],

$$\Omega_{SW} h^2 = B_{A \to B\chi} \frac{m_\chi}{m_A} \Omega_A h^2, \quad (2.1.5)$$

where $B_{A\to B\chi}$ is the branching ratio for the decay $A \to B\chi$ and $\Omega_A h^2$ is the frozen-out density of A.

Eqn. 2.1.2 suggests that the FIMP production dominates at $x \sim 1$, i.e., $T \simeq m_A$, which is a characteristic of freeze-in via renormalizable interactions, commonly known as IR freeze-in. On the other hand, smallness of FIMP DM interactions can also be achieved via higher-dimensional operators. In these cases, FIMP production dominantly takes place at the highest temperature of the cosmic bath, i.e., reheating temperature (T_R) and the DM yield is directly proportional to T_R. These kind of freeze-in is known as UV freeze-in (see ref. [48] for details).

However, in all these cases FIMP DMs are unlikely to be detected via usual strategies of WIMP detection. Unlike the case of WIMPs, the signatures of FIMP DM depend strongly on the specifications of the model. Presence of a FIMP DM may give rise to variety of signatures involving heavy stable charged particles, displaced vertices, disappearing charged tracks etc. [54], in collider experiments. Scenarios involving multiple FIMP DM [55, 56] or decaying FIMP DM [57, 58] are also possible which can leave observable signatures in astrophysical observations. We discuss some of these possibilities in the subsequent sections.

2.2 Heavy stable charged particles

Heavy stable charged particles (HSCPs) refer to exotic charged particles of masses in the GeV-TeV range, which are stable in the scale of collider detectors. Stability of these candidates are either attributed to minuscule interaction strengths or near-degeneracy in mass with their decay products. Several well-motivated BSM constructions have the possibility to leave their signatures in the forms of such HSCPs, viz. :

- In supersymmetric (SUSY) scenarios with a neutralino ($\tilde{\chi}_1^0$) as the lightest SUSY particle (LSP), lightest stop ($\tilde{t}_1$) [59] or stau ($\tilde{\tau}_1$) [60] can be the next-to-lightest SUSY particle (NLSP), with $m_{\mathrm{NLSP}} - m_{\mathrm{LSP}} \sim \mathcal{O}(\mathrm{MeV})$, in the parameter region where co-annihilations determine the relic density of $\tilde{\chi}_1^0$ DM. Lightest stop or stau can be the NLSP in scenarios with right-handed sneutrino ($\tilde{\nu}_R$) LSP [61, 62] or gravitino ($\tilde{G}$) LSP [63, 64], too. In the formar case, the NLSPs are long-lived in the collider scales due to kinematic suppression, while in the latter cases such quasi-satbility is attributed to superweak interaction strengths with the LSP. In case of $\tilde{\nu}_R$ LSP, NLSP decays via Dirac neutrino Yukawa (Y_ν) suppressed interactions, while for the $\tilde{G}$ LSP the corresponding decayrates are M_{Pl} suppressed. Such NLSPs when produced inside LHC, will

leave their footprints in the form of stable charged tracks of R-hadrons (for $\tilde{t}_1$) or $\tilde{\tau}_1$s, both in the tracking chamber as well as the muon spectrometer.

- Production of FIMP DM candidates require presence of fairly long-lived states, like A in sec. 2.1, with a typical decaylength $c\tau_A \sim \mathcal{O}(\text{m})$. For example, ref. [54] have considered the possiblity of a vector like charged fermion F serving as a parent to a scalar FIMP, s, and leaving it's signature in the LHC as a hadronic or a leptonic HSCP, depending on it's SM gauge quantum numbers. Signatures of stable charged scalars $H^{\pm}$, acting as a mother to a SM singlet fermionic FIMP N_1, have also been studied in [65].

Collider signatures

Heavy charged particles with decaylength $c\tau \gtrsim 10\,\text{m}$ [66, 67], when produced inside LHC, will pass through the detector without being decayed meanwhile. Such charged particles loose their energy via collisions with the electrons of detector material thereby giving rise to tracks. Only standard model particle with similar property being muons, they constitute the most dominant background for HSCP searches. Note that, such HSCPs are usually produced with high transverse momentum (p_T) and propagate with a velocity (β) significantly smaller than that of light, which can be used for the purpose of background discrimination.

The mean rate of energy loss of a charged particle is given by the Bethe-Bloch formula [68]:

$$\left\langle -\frac{dE}{dx} \right\rangle = \kappa \frac{Z}{A} \rho \frac{Q^2}{\beta^2} \left[\ln \left(\frac{2m_e}{I} \frac{E^2 - M^2}{M\sqrt{M^2 + 2m_e E + m_e^2}} \right) - \beta^2 \right], \qquad (2.2.1)$$

where Z is the atomic number, A is the mass number, ρ corresponds to the density and I signifies the mean excitation energy of the detector material while E, M and Q are the energy, mass and electric charge of the particle, respectively. The constant $\kappa = 0.307\,\text{MeV}\,\text{g}^{-1}\,\text{cm}^2$ and $\beta = \sqrt{1 - M^2/E^2}$ is the velocity of the charged particle. The density effect correction to energy losses has been neglected in eqn. 2.2.1. Eqn. 2.2.1 suggests that as the energy (E) increases or the velocity (β) decreases, $\left\langle -dE/dx \right\rangle$ increases. Therefore, a HSCP candidate suffers higher rate of energy loss compared to SM muons due to their larger p_T and smaller β, thereby giving rise to highly ionizing tracks. This characteristic of HSCP has been used to put constraints on their masses by CMS [66] and ATLAS [67].

Moreover, heavy particles travel much slower than the SM muons and take more time to reach the muon spectrometer, which can also be used to distinguish them from muons. The time-of-flight (TOF) to reach calorimeter cells and muon spectrometer is measured by averaging over the timing information of each of the hits associated with the candidate

track, thereby determining the mean speed β. For the SM muons β-distribution has a mean $\bar{\beta} = 0.999$ and resolution $\sigma_\beta = 0.24$ [67], while for a HSCP candidate β is usually in the range $\sim 0.4 - 0.8$. In addition to efficient background rejection, measurement of β can be combined with the particle momentum information obtained from the tracking detectors to estimate the mass of the HSCP candidate [69].

However, in this thesis we will refrain ourselves from going into the sophisticated analysis technologies used by several experimental collaborations [66, 67] and simply put a hard cut on p_T as well as on β of the HSCP candidate to achieve desired signal sensitivity by removing the SM muon background produced via Drell-Yan or from the decay of weak gauge bosons (for instance, see chapters 3 and 4). In addition, cosmic-ray muons, too, can enter the detector and reconstructed as displaced muons in the muon spectrometer. Cosmic-ray muons will typically appear as two back-to-back muons inside the muon spectrometer and can be rejected with a simple veto on the back-to-back dimuons. Furthermore, pions with large momentum may not deposit all of its energy in HCAL and enter the muon chamber. Despite very low $\pi \rightarrow \mu$ misidentification rate of muon chamber, such misidentified μ too contribute to the backgrounds for HSCP searches.

As we have so far discussed, a HSCP candidate can be pinned down via it's high rate of energy loss and low velocity. However, in order to gain insight about the interactions of the HSCP one needs to study it's decay, too. HSCPs with decaylength $\mathcal{O}(10\mathrm{m})$ do not decay inside the periphery of the main detector, but use of massive stoppers placed outside of CMS or ATLAS cavern can serve this purpose [70]. A HSCP candidate with small velocity will suffer enormous energy loss and come to rest inside the stopping material, e.g., iron. The stopper should be able to distinguish a potential HSCP candidate from the track of muon via $\langle -dE/dx \rangle$ measurement. Furthermore, it will record the stopping time, decay time as well as the stopping position of each HSCP candidate and thus will be able to detect all the decay products originating from stopping position of the parent HSCP candidate. Using such stopper one can even distinguish the decay $\tilde{\tau}_1 \rightarrow \tilde{a}\tau\gamma$ from $\tilde{\tau}_1 \rightarrow \tilde{G}\tau\gamma$ [71], when $\tilde{\tau}_1$ behaves as HSCP candidate.

BBN constraints

The agreement between the predicted abundances of the light elements, e.g., D [72], ^{3}H [73], ^{4}He [74] and the corresponding abundances observed, is a remarkable success of the standard cosmological model. However, predicted value of the ^{7}Li abundance is more than 4σ higher than the observed abundance which is commonly known as ^{7}Li problem [75]. The abundances of the light elements produced during big-bang nucleosynthesis (BBN) strongly

depend on the baryon to photon ratio (η), number of relativistic degrees of freedom (g_*) present in the thermal bath as well as the neutron lifetime ($\tau_{1/2}^n$). Quasistable states, with lifetime $\tau \gtrsim \tau_{1/2}^n$, decay during BBN and can significantly alter these predictions via complicated neuclear processes (non-thermal BBN) induced by energy injection into the plasma. For HSCP candidates decaying into photons or $e^\pm$ such constraints are severe for lifetimes exceeding $\sim 10^6$s, since these particles scatter of the thermal photon bath and undergo pair-production which causes photo-dissociation of produced light neuclei. However, if the HSCP candidate decays hadronically they may alter the $n \leftrightarrow p$ equilibrium via produced mesons and thereby change the primordial abundances by significant amount. Constraints obtained on the parameter space of $\tilde{\nu}_R$ LSP [76] as well as $\tilde{G}$ LSP [64] have shown that the assumption $\tau_{\mathrm{HSCP}} \lesssim 100\,\mathrm{s}$ almost always evades the constraints coming from BBN. Moreover, ref. [77] has shown that it is possible to destruct some of the ^{7}Li abundance by the late decay of HSCP and thus the prediction matches with the observed abundance. However, in chapters 3 and 4 of this thesis we have assumed $\tau_{\mathrm{HSCP}} \lesssim 100\,\mathrm{s}$ which is consistent with all the constraints that could possibly come from BBN predictions.

2.3   Multicomponent dark sector

Multicomponent dark matter arises quite naturally in scenarios where DM belongs to a multiplet of a dark sector gauge group [78]. The dark sector gauge symmetry breaking not only causes the associated gauge bosons to gain mass but also a small mass difference is created among the particles belonging to the same multiplet (e.g., proton and neutron are nearly degenerate due to mild breaking of isospin symmetry). The generation of such states, closely spaced in mass, has a variety of interesting phenomenological implications including co-annihilations [79] in the early universe, up-scattering [80,81] or down- scattering [82,83] in the context of DM direct detection as well as decay of the heavier dark sector state to the lighter one along with visible SM particles [84]. A few example scenarios allowing such decays among the dark sector particles are discussed below:

- Ref. [85] have considered a two-component dark sector comprising χ_1, χ_2 (with $m_{\chi_2} - m_{\chi_1} \simeq \mathcal{O}(\mathrm{MeV})$), where the decay $\chi_2 \to \chi_1 e^- e^+$ occurring inside of our galaxy gives rise to 511 keV γ-ray line signal observed by INTEGRAL [86,87].

- A two-component dark sector having the decay $\chi_2 \to \chi_1 + l$, where l is a relativistic final state, have been assumed in [88], in order to alleviate the small scale structure

problem of the ΛCDM model. Such decays heat up the DM halo via energy injection and thereby cause them to expand, which in turn soften the central cusps and disrupt the small halos [89–93].

Though, the DM components are WIMP candidates in the examples discussed till now, multicomponent FIMP scenarios are also not inconceivable. For example, in [55] two Z_2-odd SM singlet fermions, i.e., N_2, N_3, oppositely charged under $U(1)_{L_\mu - L_\tau}$ symmetry have been considered. Such a charge assignment allows only off-diagonal mass term between N_2 and N_3, which in turn forces them to remain degenerate as long as $L_\mu - L_\tau$ symmetry preserves. When the $L_\mu - L_\tau$ symmetry breaks, a small mass difference is created between the two FIMP DM candidates, N_2 and N_3. For a mass difference, $\Delta M \simeq 3.5$ keV, the decay $N_2 \to N_3 \gamma$ can explain the 3.5 keV X-ray signal observed by XMM- Newton [94] as well as Chandra telescopes [95].

2.4   Decaying dark matter

The stability of proton (p) and electron (e) are attributed to the conservation of baryon-number (B) and electric charge (Q), respectively. However, there exist several BSM scenarios including Grand Unified Theories (GUTs) as well as R-parity violating Minimal Supersymmetric Standard Model (MSSM), where B violating interactions can drive the decay of proton, but with a lifetime $\tau_{\text{proton}} \lesssim 8.2 \times 10^{33}$ yr [96]. In case of DM, though the existence of galactic halos surrounding us only require the DM candidate to have a lifetime larger than the age of the universe, many BSM scenarios predict the DM to be absolutely stable. Stability of DM candidates are usually achieved via the imposition of some continuous global symmetries or discrete symmetries like Z_2, which are the manifestations of a global symmetry breaking. Interestingly, it has been pointed out that such continuous global symmetries are expected to break down at the Planck Scale (M_{Pl}) [97–99] and hence DM may decay very slowly via higher-dimensional operators. Decaying dark matter can quite naturally arise in scenarios of freeze-in due to the smallness of the associated coupling strengths. Some of the well-motivated and widely discussed scenarios of decaying DM are as follows:

- The smallness of the QCD CP-violating θ parameter is often explained by invoking a global, chiral $U(1)$ symmetry, known as Peccei-Quinn ($U(1)_{\text{PQ}}$) symmetry [100], which is spontaneously broken by the *vev* of a scalar field at the scale f_{PQ} giving rise to a massless goldstone boson called axion (a). For the astrophysically permissible

range of values, $10^9\,\mathrm{GeV} \lesssim f_{\mathrm{PQ}} \lesssim 10^{12}\,\mathrm{GeV}$ [101], axion (a) acquires a mass $m_a \sim \Lambda_{\mathrm{QCD}}^2/f_{\mathrm{PQ}} \simeq 10^{-2} - 10^{-5}\,\mathrm{eV}$, via QCD anomaly. Axions, produced via misalignment mechanism [102] may serve as the non-thermal cold dark matter (CDM) of the universe and can also decay to two monochromatic photons with a lifetime much larger than the age of the universe [103], due to it's f_{PQ} suppressed interaction with electromagnetic field strength tensor.

- In supersymmetric theories, which also incorporate PQ symmetry as a possible solution to the strong-CP problem of QCD, axinos ($\tilde{a}$), the spin-1/2 superpartner of axions (a) are inevitable. Being charge and colour neutral, axinos ($\tilde{a}$) with masses in the keV-GeV range, can serve as the cold dark matter of the universe. Though axinos themselves can not be in thermal equilibrium due to f_{PQ} suppressed interactions, they are produced in the early universe via scatterings among coloured particles [104], or from the decay of heavier superparticles [105], in thermal bath.

  Similarly, gravitino ($\tilde{G}$), arises when supersymmetry is coupled to gravity in supergravity or superstring models. In case of gravitino the interactions are suppressed by Planck scale (M_{Pl}) and hence they are also produced via scatterings or decay of heavier superparticles present in the cosmic soup. Gravitinos in the keV-GeV mass range can account for the observed relic density of cold dark matter [106, 107].

  In scenarios of R-parity violation both $\tilde{a}$ and $\tilde{G}$ decay to a monochromatic photon (γ) in association with a neutrino (ν) via neutralino-neutrino mixing. The decay rates are suppressed in both cases, by f_{PQ} and M_{Pl}, respectively, resulting in a lifetime much larger than the age of the universe [108–110].

Astrophysical signals

Decays of DM particles inside galactic as well as extragalactic structures lead to observable signals in terms of antimatter, gamma-rays, neutrinos etc., originating from cascade decays of SM particles, produced as primary decay products. Among these, gamma-rays are particularly interesting because they do not undergo diffusion or energy losses like antimatter particles [1] and hence the spectral and spatial information of the decay processes are preserved. There are two main components of the prompt gamma-ray fluxes of a decaying DM, viz., galactic contribution and extragalactic contribution.

---

[1] The gamma-rays produced from the inverse Compton scatterings (ICS) of $e^{\pm}$ on the inter-steller radiation field (ISRF), suffer the effect of diffusion and energy losses and will be discussed in the proper place.

- *Galactic Contribution:* The differential flux of gamma-ray photons originating from the DM decay inside our galaxy is given by [111],

$$\frac{d\Phi_{\text{Gal}}}{dE_\gamma}(\Omega) = \frac{\Gamma}{4\pi\, m_{\text{DM}}}\sum_f B_f \frac{dN_\gamma^f}{dE_\gamma}\int_0^\infty ds\, \rho_{\text{DM}}[r(s,\Omega)] \qquad (2.4.1)$$

where Γ and m_{DM} are the decaywidth and mass of the decaying DM particle, respectively, B_f and dN_γ^f/dE_γ are the branching ratio and the photon energy spectrum corresponding to the final state f and $\rho_{\text{DM}}[r(s,\Omega)]$ is the DM distribution inside our galactic halo. DM distribution is usually determined by N-body simulations (*e.g.*, NFW [112], Einasto [113]) or by the observations of galactic rotation curves (*e.g.*, Isothermal [114], Burkert [115]). Though N-body simulations including the effects of baryons suggest profiles comparatively steeper towards the galactic center [116], we shall use standard NFW profile in this thesis. Another important point to note that, gamma-ray flux in a decaying DM scenario shows weaker angular dependence as well as comparatively less amplification from regions of higher DM density due to it's linear dependence on $\rho_{\text{DM}}[r(s,\Omega)]$, in contrast to the quadratic dependence in case of DM annihilations. This is reflected in the fact that most stringent constraints on decaying DM parameter space is obtained from the observation of isotropic gamma-ray background (IGRB).

- *Extragalactic Contribution:* The extragalactic distribution of dark matter is usually assumed to be homogeneous and isotropic, i.e., $\rho_{\text{DM}} = \Omega_{\text{DM}}\rho_c$ and the corresponding flux is given by [111],

$$\frac{d\Phi_{\text{EG}}}{dE_\gamma} = \frac{\Gamma}{4\pi\, m_{\text{DM}}}\Omega_{\text{DM}}\rho_c\int_0^\infty dz\, \frac{1}{H(z)}\sum_f B_f \frac{dN_\gamma^f}{dE_\gamma}[(z+1)E_\gamma]\, e^{-\tau(E_\gamma,z)} \qquad (2.4.2)$$

where $\rho_c = 4.9\times 10^{-6}\,\text{GeV}\,\text{cm}^{-3}$ is the critical energy density of the universe, $H(z) = H_0\sqrt{\Omega_\Lambda + \Omega_{\text{m}}(z+1)^3}$ is the redshift dependent Hubble parameter with Ω_Λ, Ω_{m} and Ω_{DM} being the relative energy density of cosmological constant, matter and dark matter, respectively. The integration over redshift z takes into account the gamma-ray fluxes produced from DM decay all along the evolution of the universe and the Hubble parameter converts the redshift interval to a proper distance interval. The effects of energy losses via pair production on baryonic matter or background radiation of photons (PBR) as well as photon-photon scatterings with PBR are incorporated in $e^{-\tau(E_\gamma,z)}$. For photon energy $E_\gamma \sim \text{keV}$, attenuation is dominantly due to photoionizations, while in the MeV - GeV range it is dictated by Compton losses followed by the dominance of pair production processes in the GeV - TeV energy range [117].

33

In case of DM decay of a multicomponent dark sector, fluxes in eqn. 2.4.1 and eqn. 2.4.2 will be multiplied with the fraction of the DM density accounted for by the decaying component (for example, see chapter 5 and chapter 6).

Chapter 3

Heavy stable charged tracks as signatures of non-thermal dark matter at the LHC : a study in some non-supersymmetric scenarios

3.1 Introduction

As we have seen in chapter 1, efforts are on to observe any elementary particle(s) that are potential constituents of the dark matter (DM) content of our universe. Such efforts include direct search experiments, possible collider signals and also indirect signals from extra-terrestrial sources. All these search strategies, however, are contingent upon the fact that the DM particle has a minimum interaction strength with SM particles.

Somewhat more remarkable are situations where the DM candidate is far too feebly interacting for all heavier particles to decay into it with noticeable rates within the periphery of collider detectors [118], a case in point being a feebly interacting frozen-in DM particle. One does not have any events with missing transverse energy ($\slashed{E}_T$) in such situations. On the other hand, the next heavier particle, if charged, which has the DM candidate in the final state as the only channel of its decay, becomes stable or long-lived on the scale of collider detectors[1]. The characteristic signal of such a scenario turns out to be highly ionizing

---

[1]This is also possible if the dark matter candidate is closely degenerate with a charged particle in the

charged tracks, as discussed in chapter 2, bearing the footprints of heavy particles, which can be noticed in both the tracking chambers and the muon detector.

The collider signals of such stable charged tracks are rather conspicuous is general. Following our discussions in chapter 2, however, muons produced from the decay of SM particles or the cosmic-ray muons need to be differentiated from such heavy charged particles. In general, it is found that the stable charged particles of the aforementioned kind carry much higher p_T than muons as well as they are much slower, too, if their mass is on the higher side (about 500 GeV or higher). Additional criteria such as the rate of energy loss of the charged object can, expectedly, buttress the selection criteria.

These discussions generally fit in rather appropriately into a R-parity conserving SUSY scenario where one not only has a stable R-odd FIMP DM candidate but also some additional charged NLSP [62, 120–126]. However, given the fact that we are yet to see any signature of the strongly interacting superparticles at the LHC, it is desirable to explore theoretical possibilities where the DM candidate arises via augmentation of just the electroweak sector, but is again very feeble in its interactions with other particles due to some characteristic feature of the model. Two such models are discussed in this chapter, where stable charged tracks may occur at the LHC through the production of some particle that decay into the DM candidate, but only outside the detector. We have a spin-1/2 DM, produced upon the decay of a charged fermion, in one of these illustrative cases. In the other, the Z_2-odd sector consists of an inert scalar doublet in addition to a heavy right-handed Majorana neutrino dark matter. We show in the next few sections how one expects signals of both these scenarios in the form of heavy charged tracks. In addition, the special characteristics of the individual models are reflected in some additional observations. These are, for example, the number of single charged track events vs that of a pair of charged tracks, or same-sign vs opposite-sign charge tracks. We emphasize that such observations enable one to find out the actual nature of the new physics scenario by analyzing the stable charged track signals.

Since we illustrate our point with two disparate scenarios, a little extra care needs to be taken in deriving the constraints obtained from the frozen-out quasi-stable (charged) particle density scaled appropriately. If the decaywidth of such particles is such that a non-negligible DM density is created even before the freeze-out of the former, then this latter, too, contribute to the relic. Here we have included both of these contributions, coming from in- as well as out-of-equilibrium decay of the quasi-stable charged particles.

It is important to identify regions in the parameter space of each relevant model, where

---

'dark sector', as discussed, for example, in [119].

signals of the above kinds can be observed. Keeping this in mind, we obtain the regions where the lifetime of the quasi-stable charged particle, while being less than 100 sec, in order to be consistent with light-element abundances predicted by BBN, ensure decays outside the detector, and is consistent with relic density bounds following the constraints stated above. This is in essence the space spanned by the mass difference between the quasi-stable particle and the DM candidate and the coupling pertinent to the decay of the former [2].

Organization of the chapter goes as follows: Section 3.2 contains a brief description of the models and also various constraints leading to the feebly interacting DM candidates. Strategies for LHC-based analyses, including those directed at minimising backgrounds, are incorporated in section 3.3. Section 3.4 contains our numerical results and an account of the discovery potential for such scenario. We summarize and conclude in section 3.5.

3.2 Models and constraints

In this section we outline two (non-supersymmetric) new physics scenarios. A quasi-stable charged particle is envisioned in each of them, which decays very slowly into the DM particle. We also mention the constraints to which each model is subjected.

3.2.1 Type III seesaw with sterile neutrino

We consider, in addition to the SM particles, three fermionic SU(2) triplets Σ_{jR} of zero hypercharge, each composed of three right-handed Weyl Spinors of zero U(1) hypercharge. Each Σ_{jR} has the components $(\Sigma_{jR}^1, \Sigma_{jR}^2, \Sigma_{jR}^3)$. Out of them one can construct the charged and neutral triplets $(\Sigma_{jR}^+, \Sigma_{jR}^0, \Sigma_{jR}^-)$ where (j = 1-3), represented by the 2×2 matrix

$$\Sigma_{jR} = \begin{bmatrix} \Sigma_{jR}^0/\sqrt{2} & \Sigma_{jR}^+ \\ \Sigma_{jR}^- & -\Sigma_{jR}^0/\sqrt{2} \end{bmatrix}, \tag{3.2.1}$$

where the fields $(\Sigma_{jR}^+, \Sigma_{jR}^0, \Sigma_{jR}^-)$ have been defined as

$$\Sigma_{jR}^+ = \tfrac{1}{\sqrt{2}}(\Sigma_{jR}^1 - i\Sigma_{jR}^2),\ \Sigma_{jR}^- = \tfrac{1}{\sqrt{2}}(\Sigma_{jR}^1 + i\Sigma_{jR}^2),\ \Sigma_{jR}^0 = \Sigma_{jR}^3,$$

In addition, we consider a Z_2 symmetry to ensure the stability of DM, under which the SM fields as well as two of the fermionic triplets are even. These fields are free to mix

---

[2]There can, in principle, also be regions where the next-to-lightest (charged) particle decays within the detector, thus leading to signals with disappearing tracks. Such signals are not considered in this study.

amongst themselves. Thus one generates two tree-level neutrino masses through the Type III seesaw mechanism and hence explains the observed mass-squared differences as suggested by neutrino oscillation experiments. On the other hand, the remaining triplet does not contribute to neutrino mass generation, because it is *odd under imposed Z_2 symmetry*. The neutral component of the Z_2-odd triplet mixes with a Z_2-odd singlet sterile neutrino ν_{sR} (another right-handed Weyl fermion) to produce a dark matter candidate. If ν_{sR} be light enough compared to Σ_{3R} and its mixing with Σ_{3R}^0 be small enough, the ν_{sR}-dominated mass eigenstate can be a viable SuperWIMP Dark Matter candidate.

Thus, over and above the SM part, the Lagrangian contains the following renormalizable terms [127–129] (written in terms of Weyl spinors):

$$
\begin{aligned}
\mathcal{L} &= \operatorname{Tr}\left[\bar{\Sigma}_{jR} i \slashed{D} \Sigma_{jR}\right] - \frac{1}{2} \operatorname{Tr}\left[\bar{\Sigma}_{jR} M_\Sigma \Sigma_{jR}^c + h.c\right] - \left(\sqrt{2}\bar{L}_{Lj} Y_\Sigma \Sigma_{\alpha R} \tilde{\Phi} + h.c\right) \\
&\quad + \frac{i}{2} \bar{\nu}_{sR} \slashed{\partial} \nu_{sR} - \frac{1}{2}\left(\bar{\nu}_{sR} M_{\nu_s} \nu_{sR}^c + h.c\right),
\end{aligned}
\tag{3.2.2}
$$

where $L_L \equiv (\nu_L, l_L)^T$, $\Phi \equiv (\phi^+, (v + H + i\phi_0)/\sqrt{2})^T$, $\tilde{\Phi} = i\tau_2 \Phi$, $\Sigma_{jR}^c = (\Sigma^c)_{jL} = C\bar{\Sigma}_{jR}^T$ and summation over j and α are implied. One has j = 1, 2, 3 and α = 1, 2, denoting generation indices for the SM and triplet fermions, respectively, involved in interactions with the Higgs doublet. It should be noted that in eqn.(3.2.2), the Yukawa coupling terms for Z_2-odd triplet Σ_{3R} as well as sterile neutrino ν_{sR} are prohibited due to the Z_2 symmetry. As the hypercharges of Σ_{3R} and ν_{sR} are both zero and in addition $T_3 = 0$ for Σ_{3R}, they have no Z-interaction, thus evading direct search constraints on a DM candidate potentially emerging out of them.

The smallness of $\nu_{sR} - \Sigma_{3R}^0$ mixing can be justified using dimension-five interaction terms. One may assume that such terms are artifacts of some new physics at a higher scale Λ, encapsulated in the effective Lagrangian [23]

$$
\mathcal{L}_5 = \left(\frac{\alpha_{\Sigma\nu_s}}{\Lambda} \Phi^\dagger \bar{\Sigma}_{3R} \Phi \nu_{sR}^c + \frac{\alpha_{\Sigma\nu_s}}{\Lambda} \Phi^\dagger \bar{\Sigma}_{3R}^c \Phi \nu_{sR} + \frac{\alpha_{\nu_s}}{\Lambda} \Phi^\dagger \Phi \bar{\nu}_{sR} \nu_{sR}^c + \frac{\alpha_\Sigma}{\Lambda} \Phi^\dagger \bar{\Sigma}_{3R} \Sigma_{3R}^c \Phi\right) + h.c.,
\tag{3.2.3}
$$

Though the various Wilson coefficients $(\alpha_{\Sigma\nu_s}, \alpha_\Sigma, \alpha_{\nu_s})$ shown above are formally mentioned in the discussion that follows they have been all set to unity in our numerical calculation, keeping Λ as the single parameter characterising all dimension-5 terms. This simplification does not affect our results qualitatively.

The fields in the triplet-singlet sector in the four-component notation include the charged Dirac fermions

$$
\eta_j^- = \Sigma_{jR}^- + \Sigma_{jR}^{+c}, \quad \eta_j^+ = \Sigma_{jR}^{-c} + \Sigma_{jR}^+,
$$

which have a definite mass $(M_\Sigma - \frac{\alpha_\Sigma v^2}{2\Lambda})$ for $j = 3$. One also has in this sector the Majorana fermions

$$\eta_j^0 = \Sigma_{jR}^0 + \Sigma_{jR}^{0c} , \quad N^0 = \nu_{sR}^0 + \nu_{sR}^{0c}.$$

The triplets of the first two families (corresponding to j = 1,2) can of course mix with the SM leptons once electroweak symmetry is broken.

In terms of the Dirac and Majorana fermions, eqn.(3.2.2) can be rewritten (in terms of the individual components of SU(2) doublets and triplets) as

$$
\begin{aligned}
\mathcal{L} &= \bar{\eta}_j i\partial\!\!\!/\eta_j + \frac{1}{2}\bar{\eta}_j^0 i\partial\!\!\!/\eta_j^0 - \bar{\eta}_j M_\Sigma \eta_j - \frac{1}{2}\bar{\eta}_j^0 M_\Sigma \eta_j^0 + g(\bar{\eta}_j^0 W_\mu^+ \gamma^\mu \eta_j + h.c) - g\bar{\eta}_j W_\mu^3 \gamma^\mu \eta_j \\
&\quad - [\Phi_0 \bar{\eta}_\alpha^0 Y_\Sigma \nu_{Lj} + \sqrt{2}\Phi_0 \bar{\eta}_\alpha Y_\Sigma l_{Lj} + \phi^+ \bar{\eta}_\alpha^0 Y_\Sigma l_{Lj} - \sqrt{2}\phi^+ \bar{\nu}_{Lj}^c Y_\Sigma \eta_\alpha + h.c.] \\
&\quad + \frac{i}{2}\bar{N}^0 i\partial\!\!\!/N^0 - \frac{1}{2}\bar{N}^0 M_{\nu_s} N^0,
\end{aligned}
\tag{3.2.4}
$$

while the dimension-5 terms are,

$$
\begin{aligned}
\mathcal{L}_5 &= \frac{\alpha_{\Sigma\nu_s}}{\Lambda}\left(\frac{1}{\sqrt{2}}\phi^-\phi^+\bar{\eta}_3^0 N^0 + \phi^-\Phi_0\bar{\eta}_3 N^0 + \phi^+\Phi_0^*\bar{N}^0\eta_3 + \frac{1}{\sqrt{2}}\Phi_0^*\Phi_0\bar{N}^0\eta_3^0\right) + h.c. \\
&\quad (\phi^+\phi^- + \Phi_0\Phi_0^*)\left[\frac{\alpha_{\nu_s}}{\Lambda}\bar{N}^0 N^0 + \frac{\alpha_\Sigma}{\Lambda}\left(\frac{1}{2}\bar{\eta}_3^0\eta_3^0 + \bar{\eta}_3\eta_3\right)\right],
\end{aligned}
\tag{3.2.5}
$$

where $\Phi_0 = (v + H + i\phi_0)/\sqrt{2}$, the neutral component of the SM scalar doublet.

The $N^0 - \eta_3^0$ mass matrix is,

$$
\begin{bmatrix}
M_{\nu_s} - \frac{\alpha_{\nu_s} v^2}{\Lambda} & \frac{\alpha_{\Sigma\nu_s} v^2}{\sqrt{2}\Lambda} \\
\frac{\alpha_{\Sigma\nu_s} v^2}{\sqrt{2}\Lambda} & M_\Sigma - \frac{\alpha_\Sigma v^2}{2\Lambda}
\end{bmatrix},
$$

which, when diagonalized, yields the following mass eigenstates,

$$\chi = \cos\beta \, N^0 - \sin\beta \, \eta_3^0, \tag{3.2.6}$$

$$\psi = \sin\beta \, N^0 + \cos\beta \, \eta_3^0, \tag{3.2.7}$$

where χ is the lighter state with mass,

$$
\begin{aligned}
M_\chi &= \frac{1}{2}\Bigg(\left(M_{\nu_s} - \alpha_{\nu_s} v^2/\Lambda + M_\Sigma - \alpha_\Sigma v^2/2\Lambda\right)^2 \\
&\quad - \sqrt{\left(M_\Sigma - \alpha_\Sigma v^2/2\Lambda - M_{\nu_s} + \alpha_{\nu_s} v^2/\Lambda\right)^2 + 4\left(\alpha_{\Sigma\nu_s} v^2/\Lambda\right)^2/2} \Bigg),
\end{aligned}
\tag{3.2.8}
$$

and β is the mixing angle given by

$$\tan 2\beta = \frac{(\alpha_{\Sigma\nu_s} v^2)/\sqrt{2}\Lambda}{(M_\Sigma - \alpha_\Sigma v^2/2\Lambda - M_{\nu_s} + \alpha_{\nu_s} v^2/\Lambda)}. \tag{3.2.9}$$

If we consider the new physics scale Λ to be high enough, being on the order of 10^{14} GeV or above, the dimension-5 couplings become very small and hence χ interacts very weakly with the rest of the particles in the spectrum. Moreover, we can assume $M_\chi \simeq M_{\nu_s}$. One can safely assume that χ has never been in thermal equilibrium with the thermal soup during the evolution of the universe and hence is a viable candidate for *SuperWIMP* (non-thermal) dark matter. In such a scenario, χ may be produced from the decay of next-to-lightest odd particle(s) (NLOP) viz., η_3^+, η_3^- and ψ. The discussion that follows depends on the NLOP $\eta_3^\pm$ being effectively degenerate with the state ψ, something that is responsible for its quasi-stable character. This may in principle be threatened by electromagnetic radiative corrections raising the $\eta_3^\pm$ mass [21]. Such an issue can be alleviated by allowing the possibility of further mixing between $\eta_3^\pm$ and some additional Z_2-odd fermion(s) as outlined in appendix A.1.

The production of χ occurs from the decay of NLOPs $\eta^\pm$ and ψ and the yield of the DM χ is calculated by solving the coupled Boltzmann equations [130, 131],

$$
\frac{dY_{NLOP}}{dx} = -\sqrt{\frac{\pi}{45G}}\frac{g_*^{1/2}M_\Sigma}{x^2}\langle\sigma v_{Mol}\rangle(Y_{NLOP}^2 - Y_{NLOP}^{eq2}) - \sqrt{\frac{45}{\pi^3G}}\frac{x}{2\sqrt{g_{eff}}M_\Sigma^2}\langle\Gamma\rangle Y_{NLOP},
$$

$$
\frac{dY_\chi}{dx} = \sqrt{\frac{45}{\pi^3G}}\frac{x}{2\sqrt{g_{eff}}M_\Sigma^2}\langle\Gamma\rangle Y_{NLOP}, \tag{3.2.10}
$$

where Y_{NLOP} and Y_χ are the yield of NLOP and DM, respectively, and $x = M_\Sigma/T$. The parameter g_* is defined as the effective degrees of freedom of all the relativistic species still in thermal equilibrium when the NLOP freezes out. $\langle\Gamma\rangle$ is the thermally averaged decaywidth of NLOP into DM and G is the gravitational constant.

In the right panel of Figure 3.1 we depict the evolution of the NLOP (red) as well as the DM (blue) as a function of temperature of the Universe. The plot has been generated considering $M_\Sigma = 1$ TeV, $M_{\nu_s} = 500$ GeV and $\Lambda \sim 10^{14.5}$ GeV. The equilibrium yield is shown by the brown curve. We can clearly see that the NLOP depart from the equilibrium and then further decays to the DM depending on its lifetime. The larger the lifetime, later the decay of NLOP and then the yield of NLOP vanishes. For the DM the freeze-in yield increases as the temperature decreases and becomes constant after some time ($x \sim 10$). The freeze-in yield is dominant when $x \sim 1$, i.e., when the NLOP freezes-out. The inset shows that the DM yield gets an additional contribution from the NLOP decay after freeze-out. The relative contribution in the total DM relic density coming from the decay of NLOP depends on the masses of the NLOPs and the DM particle.
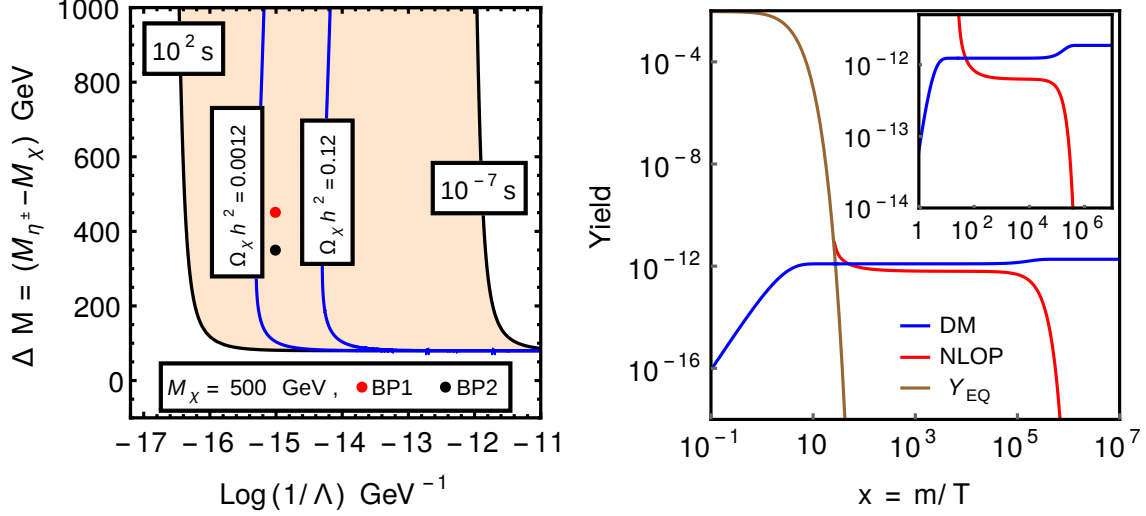
Figure 3.1: Contours of life time of HSCP candidates(Black) and freeze-in relic density(Blue) of DM candidate χ as a function of mass difference between NLOP and DM candidates and scale of new physics Λ for Type III Seesaw model with sterile neutrino is shown in the left plot. Lower limit of the lifetime (10^{-7} sec) is coming from the fact that the charged particle has to decay outside the detector whereas the upper limit of 100 sec is coming from BBN constraints. The current data of CDM relic density put constraints on the parameter space. The benchmark points we have used for the collider analysis are represented as the black and red points. Right panel shows the yield of the DM candidate (Blue) and NLOP (Red) as a function of ($x = \frac{m}{T}$), where m is the mass of the NLOP. We have assumed $M_\Sigma = 1$ TeV and $M_{\nu_s} = 500$ GeV. The brown curve shows the equilibrium distribution of the NLOP. The effects after freeze-out of NLOP is magnified in the inset.

The decaywidth of $\eta_3^\pm$ into χ is given by

$$\Gamma_{\eta_3^\pm \to \chi W^\pm} = \frac{g^2 \sin^2 \beta \sqrt{E_w^2 - M_w^2}}{4\pi M_\Sigma^2} \left(M_\Sigma(M_\Sigma - E_w) - 3M_{\nu_s} M_\Sigma + \frac{2M_\Sigma E_w}{M_w^2}(M_\Sigma E_w - M_w^2) \right),$$
(3.2.11)

where $E_w = \frac{M_\Sigma^2 - M_{\nu_s}^2 + M_w^2}{2M_\Sigma}$. For $M_\Sigma = 1$ TeV, $M_{\nu_s} = 500$ GeV and $\Lambda = 10^{15}$ GeV the lifetime of $\eta_3^\pm$ is 0.167 s. For a comparable choice of parameters ψ has a lifetime of 0.169 s for the decay $\psi \to \chi H$. Thus $\eta_3^\pm$ or ψ never decays inside the LHC detector for such masses and, more importantly, scale of new physics which is at the origin of the dimension-5 terms. The allowed parameter space is explored in the left plot of Figure 3.1. One can thus see $\eta_3^+ \eta_3^-$

41

produced in proton-proton collision via the Drell-Yan process, showing up as charged tracks all the way up to the muon chamber. The existing mass limit on such a quasi-stable particle is 730 GeV from the LHC data till now [132]. Since Σ_{3R} has zero hypercharge, ψ is only produced in association with $\eta_3^\pm$ via W-mediation. Such final states have the characteristic signature of single heavy stable charged track + missing transverse energy (MET). In the following sections we discuss discovery prospects of both of these signals at the LHC.

An important constraint in this study comes from the light nuclei abundances produced during Big-Bang Nucleosynthesis (BBN), discussed in detail in chapter 2. In our study we have considered an upper bound of the lifetime of $\eta_3^\pm$ or ψ to be $\simeq 100$ sec in order to respect the constraint imposed by deuterium abundances during BBN [126]. Left panel of Figure 3.1 shows variation of lifetime of the NLOP as a function of its mass difference with DM candidate and with the scale of new physics Λ. It is evident from eqn. 3.2.9 that if we increase the new physics scale, the coupling $\sin\beta$, which governs the decay of NLOP into DM decreases resulting a increase of the lifetime. The light colored region is the allowed parameter space for the Type III seesaw model with sterile neutrinos to spot a HSCP at the LHC. The blue curves in the left panel of Figure 3.1 shows two different contours of relic density coming from the freeze-in contribution only. As Λ increases, the decaywidth decreases, yielding less DM relic coming from freeze-in production. Since the freeze in contribution can not exceed the total CDM relic density the right side of the right blue contour is disallowed.

3.2.2 Inert doublet model (IDM) with right-handed Majorana neutrino

In this model, the SM particles are postulated to be supplemented with an additional scalar doublet (Φ_2) with hypercharge 1 and three right-handed SU(2) singlet Majorana neutrinos (N_{iR}) [133–135]. Once more we consider a Z_2-symmetry to ensure stability of what will emerge as the DM candidate. Under the Z_2, two of the Majorana neutrinos are even and mix with the SM particles to generate neutrino masses through Type-I seesaw mechanism. The third Majorana neutrino, denoted as N_{3R} as well as the additional scalar doublet Φ_2 is Z_2-odd [3]. As a result, Φ_2 never acquires a vacuum expectation value (vev) and is called the *inert doublet.*

---

[3]Some variants of such a model, postulating all right-handed Majorana neutrinos to be Z_2-odd, have been studied in [65, 136].

The scalar potential in this case is

$$
\begin{aligned}
V(\Phi_1, \Phi_2) &= \lambda_1(\Phi_1^\dagger\Phi_1)^2 + \lambda_2(\Phi_2^\dagger\Phi_2)^2 + \lambda_3(\Phi_1^\dagger\Phi_1)(\Phi_2^\dagger\Phi_2) + \lambda_4(\Phi_2^\dagger\Phi_1)(\Phi_1^\dagger\Phi_2) \\
&\quad + \left[\frac{\lambda_5}{2}(\Phi_1^\dagger\Phi_2)^2 + h.c\right] + \mu_1\Phi_1^\dagger\Phi_1 + \mu_2\Phi_2^\dagger\Phi_2,
\end{aligned}
\tag{3.2.12}
$$

where all parameters are real and Φ_1 is the SM scalar doublet. The two doublets can be expressed in terms of their components as

$$
\Phi_1 = \begin{bmatrix} G^+ \\ \frac{1}{\sqrt{2}}(v + h + iG^0) \end{bmatrix}, \quad \Phi_2 = \begin{bmatrix} H^+ \\ \frac{1}{\sqrt{2}}(H^0 + iA^0) \end{bmatrix},
$$

where, v = 246 GeV, is the electroweak vev. After spontaneous symmetry breaking, one obtains five physical states $(h, H^0, A^0, H^\pm)$ and three Goldstone bosons $(G^0, G^\pm)$, where h corresponds to the physical SM-like Higgs field, with mass around 125 GeV. The CP-even (H^0), CP-odd (A^0) and charged $(H^\pm)$ scalars arise from the inert doublet, since the discrete symmetry prevents mixing between Φ_1 and Φ_2. The physical scalar masses are given by,

$$
M_{H^\pm}^2 = \mu_2 + \frac{1}{2}\lambda_3 v^2, \tag{3.2.13a}
$$

$$
M_{H^0}^2 = \mu_2 + \frac{1}{2}\lambda_L v^2, \tag{3.2.13b}
$$

$$
M_{A^0}^2 = \mu_2 + \frac{1}{2}\lambda_A v^2, \tag{3.2.13c}
$$

where $\lambda_{L/A} = (\lambda_3 + \lambda_4 \pm \lambda_5)$ and λ_1 is determined using M_h=125 GeV. Note that it is possible to have substantial mass splittings among H^0, A^0 and $H^\pm$, since λ_3, λ_L and λ_A are *a priori* unrelated. The scalar potential is bounded from below if it does not turn negative for large field values along any possible field direction. In this case, stability of the electroweak vacuum is ensured at the electroweak scale and just above, if the following vacuum stability conditions are satisfied [137–140]:

$$
\lambda_1 > 0, \;\; \lambda_2 > 0, \;\; \lambda_3 + \sqrt{\lambda_1\lambda_2} > 0, \;\; \lambda_3 + \lambda_4 - |\lambda_5| + \sqrt{\lambda_1\lambda_2} > 0. \tag{3.2.14}
$$

In addition, we have also ensured that values of the quartic interactions used in the phenomenological analyses below are consistent with the perturbativity bounds, namely,

$$
\lambda_i < 4\pi, i = 1, \cdots, 5. \tag{3.2.15}
$$

The relevant Yukawa interactions and Majorana mass terms are

$$
\mathcal{L}_Y = y_{\nu j}\bar{N}_{3R}\tilde{\Phi}_2^\dagger L_{Lj} + y_{\alpha j}\bar{N}_{\alpha R}\tilde{\Phi}_1^\dagger L_{Lj} + \frac{M_j}{2}\bar{N}_{jR}^c N_{jR} + h.c, \tag{3.2.16}
$$

43
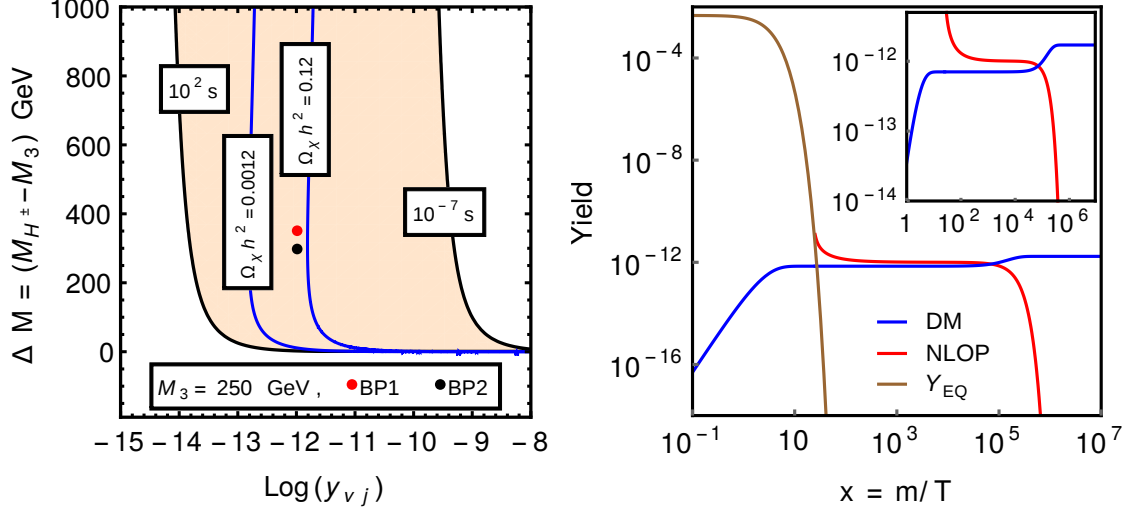
Figure 3.2: Contours of lifetime of HSCP candidates(Black) and freeze-in relic density of DM candidate χ (Blue) as a function of mass difference between NLOP and DM candidate and minuscule coupling $y_{\nu j}$ for inert doublet model with right handed Majorana neutrino in the left hand side plot. Detector length restricts the lower limit of lifetime to be 10^{-7} sec and the BBN constrains the lifetime to be less than 100 sec. Current data of CDM relic density further constrains the parameter space. The benchmark points we have used for the collider analysis are represented as the black and red points. The plot in the right depicts the yield of DM candidate χ in Blue and that of NLOP in red as a function of $x = \frac{m}{T}$, m being the mass of the NLOP. For this plot we have assumed $M_{H^\pm} = 500$ GeV and $M_3 = 250$ GeV. The brown curve shows the equilibrium distribution of the NLOP. The effects after freeze-out of NLOP is magnified in the inset.

where $\alpha = 1,2$ and $j = 1,2,3$ whereas $L_L = (\nu_L, l_L)^T$. The Yukawa couplings between the Z_2-even Majorana neutrinos and the SM scalar Φ_1 are responsible for generation of Dirac type neutrino masses, while the Yukawa coupling which combines N_{3R} and Φ_2 can only generate mass for the third neutrino at one-loop level.

If N_{3R} becomes the lightest in the Z_2-odd sector then the Majorana fermion $\chi = N_{3R} + N_{3R}^c$ can serve as a viable dark matter candidate. In addition, if the parameters $\mu_2, \lambda_3, \lambda_4,$ and λ_5 are such that $M_{A^0} \simeq M_{H^0} > M_{H^\pm}$ then the next-to lightest odd particle (NLOP) will be the charged scalar $H^\pm$.

The current neutrino data in principle allow one of the three light neutrinos to be ar-

bitrarily light. Hence $y_{\nu j}$ can be very tiny (for example, on the order of 10^{-12} while still being *technically natural*). Consequently the DM candidate χ will never equilibrate with the thermal soup and hence should be treated as a non-thermal DM. As we have discussed earlier here also we have computed the DM relic density coming from the freeze-in production as well as the later decay of NLOP $(H^{\pm})$ using eqn. 3.2.10 where the parameter M_{Σ} should be replaced by $M_{H^{\pm}}$.

In the right panel of Figure 3.2 we depict the evolution of the NLOP (red) as well as the DM (blue) as a function of temperature of the Universe. The plot has been generated considering $M_{H^{\pm}} = 500$ GeV, $M_3 = 250$ GeV and $y_{\nu j} \sim 10^{-12}$. The qualitative features of the yield of NLOP and DM are same as in the earlier model. The plot in the left panel of Figure 3.2 shows the allowed parameter region as a function of ΔM and $y_{\nu j}$ which is consistent with correct CDM relic density. Also in the left panel of Figure 3.2 we have pointed the benchmark points for the collider analysis.

The decaywidth of NLOP into the DM is given by,

$$\Gamma_{H^{\pm} \to \chi l^{\pm}} = \frac{y_{\nu j}^2 M_{H^{\pm}}}{4\pi} \left(1 - \frac{M_3^2}{M_{H^{\pm}}^2}\right)^2 . \qquad (3.2.17)$$

With $y_{\nu j}$ as small as $\simeq 10^{-12}$, $M_{H^{\pm}} = 500$ GeV and $M_3 = 250$ GeV, the lifetime of $H^{\pm}$ is 0.0297 s. Therefore, for suitable values of parameters as explored in Figure 3.2, $H^{\pm}$, once produced at the LHC decays outside the detector, leaving its signature in the form of a stable charged track. Since H^0 and A^0 are heavier than $H^{\pm}$, they may decay into $H^{\pm}$ inside the detector depending on the mass splitting. Consequently this scenario can be looked for both opposite-and same-sign heavy stable charged tracks ($H^{\pm}H^{\mp}$, $H^{\pm}H^{\pm}$).

In order to be consistent with the recent LHC bounds on long-lived charged particles obtained from Drell-Yan production [132], we have always used $M_{H^{\pm}} > 360$ GeV. As is already mentioned, following the constraint imposed by the light element abundances during BBN we have to ensure that the lifetime of our proposed LLP candidate be $\lesssim 100$ sec. The available parameter space is shown in Figure 3.2, as a function of NLOP mass difference with DM candidate and the Yukawa coupling.

3.3 Strategy for analysis

In the collider analysis we have used `FeynRules 2.0` [141] and the resulting UFO files are fed into `MadGraph5_aMC@NLO` [142] to generate our Signal events. Parton showering as well as hadronization is done using `Pythia 6` [143]. Finally the detector simulation is done using

`Delphes 3` [144] framework. For the signal generation we have used `CTEQ6L1` [145] as our Parton Distribution Function.

As we have mentioned in chapter 2, in order to distinguish such signals of heavy stable charged tracks from the tracks of SM muons, we put cuts on the transverse momentum (p_T) and β of the heavy charged tracks. The exact values of the cuts that are used in our analysis are given in Table 3.1.

Parameter	β	p_T	$|y(\mu_{1,2})|$	$\Delta R(\mu_1, \mu_2)$
Cut values	(A)[0.2, 0.95]	> 70 GeV	< 2.5	> 0.4
	(B)[0.2, 0.80]	> 70 GeV	< 2.5	> 0.4

Table 3.1: Basic selection cuts applied to analyze signals of heavy stable charged track.

Cut set (A) above corresponds exactly to the ATLAS specification [67]. In cut set (B), we have experimented a bit by inserting a stronger β-cut following [66], while keeping everything else unchanged. This stronger β-cut is somewhat more effective, since it removes all backgrounds by retaining enough signal events even at low luminosity. This is, especially true for 'single charged track events' studied later. In order to obtain a realistic velocity distribution of such heavy stable charged tracks we smeared the velocity (β) with a Gaussian resolution of mean $\bar{\beta} = p/E$ and $\sigma_\beta = 0.024$ [67]. For the SM muons, on the other hand, following ref [67] we have used $\bar{\beta} = 0.999$.

Next, we discuss the proposed benchmark points and backgrounds considered for each of the respective channels.

3.3.1 Type III seesaw with sterile neutrino

In this model we focus on the following channels, viz.

- Opposite-sign charge tracks:

$$p\,p \rightarrow Z^* \rightarrow \eta_3^\pm\,\eta_3^\mp.$$

- Single charge track + $\not{E}_T$:

$$p\,p \rightarrow W^{\pm*} \rightarrow \eta_3^\pm\,\psi.$$

We have chosen the benchmark points given in Table 3.2, which is well inside the available parameter space as explored in Figure 3.1. We have also set the Wilson coefficients $\alpha_{\Sigma\nu_s}$, α_Σ and α_{ν_s} to unity, as already stated.

Parameters	M_Σ (GeV)	M_{ν_s} (GeV)	Λ (GeV)
BP1	850	500	10^{15}
BP2	950	500	10^{15}

Table 3.2: Benchmark points for studying the discovery prospects of stable charged tracks of $\eta_3^\pm$ and ψ for Type III seesaw model at 14 TeV run of LHC.

In Figure 3.3 we have plotted production cross-section of $\eta_3^\pm \eta_3^\mp$ and $\eta_3^\pm \psi$ at 14 TeV LHC. The cross-section of $\eta_3^\pm \psi$ is larger due to the coupling with the W-boson.

Background Estimation

The SM background for opposite-sign charged tracks is muons coming mainly from Drell-Yan production of $\mu^\pm$, $\tau^\pm$ (computed at NNLO) [146] and $t\bar{t}$ (N^{3}LO) [147]. We have also considered the sub-dominant backgrounds coming from W^+W^-, WZ and ZZ final states (NLO) [148].

For analyzing the signal of single heavy stable charged track $+ \not{E}_T$, $W^\pm$ (NNLO) [146] and $t\bar{t}$ (N^{3}LO) [147] final states are the dominant backgrounds. Diboson (W^+W^-, WZ and ZZ) [148] final states are sub-dominant backgrounds which, too, have taken into account.

In order to be as realistic as possible, we have also considered the background coming from cosmic ray muons. Following the analysis of CMS, cosmic ray muon constitutes nearly 60% of total background in case of opposite-sign heavy charged tracks [66]. For single charged track$+\not{E}_T$ analysis, due to lack of available information in the literature, we have assumed the cosmic ray muon backgrounds is the same as in the case of opposite-sign charge tracks. However, even if we assume such background to be one order of magnitude larger than that in case of opposite-sign charged track pairs the net background cross-section changes by about 0.5% only. This is because the SM backgrounds arising from LHC processes dominates over the cosmic ray muon backgrounds, when it comes to a single observed tracks. Based on this observation, we believe that our background estimate is convergent and realistic.

The opposite sign dimuon background after the selection cuts (A) of Table 4.1 is 2.667 fb while the single muon track $+ \not{E}_T$ has a background cross-section 3368.6 fb. The single muon track $+ \not{E}_T$ background can be further reduced by applying a suitable $\not{E}_T$ cut as discussed later in section 3.4.1.

47
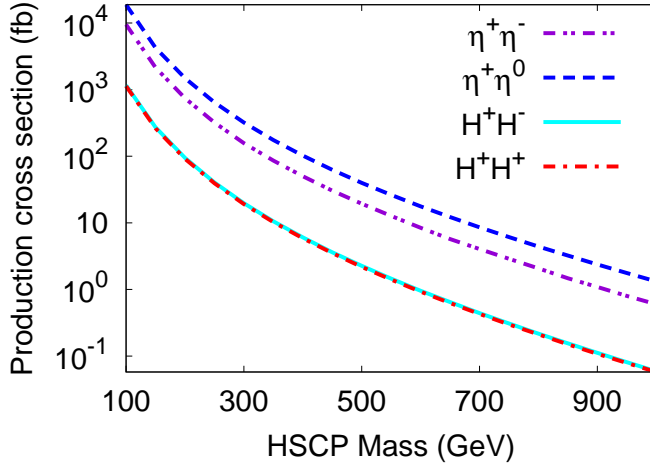
Figure 3.3: Production cross-section of heavy stable charged particles (HSCP) of Type III Seesaw model and IDM at the 14TeV LHC. Here dashed blue line also includes the production cross-section of $\eta^- \eta^0$ and dot-dashed red line shows the cross-section for $H^\pm H^\pm$.

3.3.2 Inert doublet model with right-handed Majorana neutrino

We have explored the following signals in this scenario :

- Opposite-sign charge tracks ($H^\pm H^\mp$)

- Same-sign charge tracks ($H^\pm H^\pm$)

The second channel is possible here because $H^0(A^0)$, being a self-conjugate particle, can decay into H^+ and H^- with equal probabilities. This is not expected in the previously considered scenario with $\eta_3^\pm$ and ψ being nearly-degenerate. The dominant production channel for these signals is the following

$$pp \to W^{\pm *} \to H^\pm H^0 \to H^\pm (H^\pm W^{*\mp}/H^\mp W^{*\pm}). \tag{3.3.1}$$

The production cross-sections of signal processes in the 14 TeV run of the LHC are shown in Figure 3.3. The opposite-sign charge track production also gets additional contribution from Z-mediation which is order of magnitude smaller than the dominant channel.

The benchmark points that are used in our analysis are tabulated in Table 3.3 are all allowed according to Figure 3.2, and also satisfy vacuum stability and perturbativity criteria given in eqns. 3.2.14 and eqn. 3.2.15.

48

Parameters	$M_{H^\pm}$(GeV)	M_{H^0}(GeV)	M_{A^0}(GeV)	M_3 (GeV)	λ_2	λ_L	$y_{\nu j}$
BP1	550	555	555	250	0.5	0.04	10^{-12}
BP2	600	605	605	250	0.5	0.04	10^{-12}

Table 3.3: Benchmark points for studying the discovery prospects of stable charged tracks of $H^\pm$ for IDM at 14 TeV run of LHC.

Background Estimation

For the signal corresponding to two opposite-sign heavy charged tracks we have considered the same backgrounds as is already discussed in section 3.3.1.

In case of the same-sign heavy stable charged tracks the dominant backgrounds (same sign dimuons) are coming from $t\bar{t}$ (N³LO) [147], $t\bar{t}W$ (NLO) [149] and diboson final states (NLO) [148]. We have also considered the sub-dominant backgrounds like $W^\pm\gamma$ and $WW + 2jets$. Cosmic ray muon background is considered to be the same as in the case of opposite-sign charged tracks in order to be conservative enough regarding background estimation.

3.4   Results and Discussions

In this section we have discussed the discovery prospects of heavy stable charged tracks in the considered benchmark points during 14 TeV runs of LHC. We compute the statistical significance of the proposed final states using the standard formula

$$\mathcal{S} = \frac{N_S}{\sqrt{N_S + N_B}}, \tag{3.4.1}$$

where N_S and N_B are respectively number of signal and background events passing the cuts.

3.4.1   Type III seesaw with sterile neutrino

Opposite-sign stable charged tracks of $\eta_3^\pm \eta_3^\mp$

We have presented in Figure 3.4 the p_T-and β-distribution of the harder charged track for the two benchmark points BP1(blue) and BP2(red) as in Table 3.2. We have also shown the background dimuon distribution in solid black histogram. The signal tracks tend to have higher p_T owing to the NLOP mass. At the same time, the fact that they are produced by
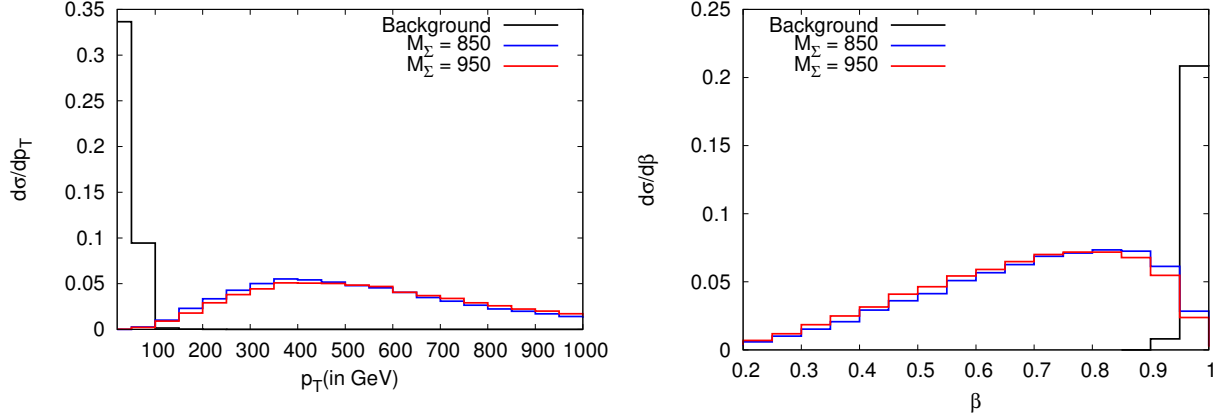
Figure 3.4: p_T-and β-distribution of the opposite sign stable charged tracks of $\eta_3^\pm \eta_3^\mp$ for Type III seesaw with sterile neutrino for the benchmark points BP1(blue) and BP2(red) as in Table 3.2. Background muon distribution is shown in black histogram.

Drell-Yan process close to kinematic threshold in the parton center-of-mass frame endows them with β well below unity. Thus one is able to distinguish NLOP tracks from muons using the p_T-and β-cuts listed in Table 4.1. The imposition of such cuts allows one to predict a statistical significance of 5σ for various integrated luminosities, as listed in Table 3.4.

In Figure 3.5 we have shown 3σ(blue) and 5σ(magenta) significance contours at the 14 TeV LHC, in terms of heavy charged particle and integrated luminosity. The horizontal lines represent integrated luminosities of 300 fb^{-1} and 3000 fb^{-1}. As we can see with the 14 TeV run of LHC this model can be probed up to $M_\Sigma = 1060(960)$ GeV with $3\sigma(5\sigma)$ significance with integrated luminosity of $300fb^{-1}$. Whereas at HL-LHC with $3000fb^{-1}$ data the model can be explored up to $\sim 1280(1190)$ GeV. The inset in Figure 3.5 depicts the projected significance for the BP1 as a function of integrated luminosity. For BP1 $3\sigma(5\sigma)$ significance can be achieved with integrated luminosity $\sim 35(100)fb^{-1}$.

Single stable charged tracks of $\eta_3^\pm + \not{E}_T$

The $\eta_3^\pm$ charged track $+ \not{E}_T$ also has appreciable production cross-section and at the same time suffers from a large background from $W^\pm$ production at the LHC [150]. One obviously has to go beyond the basic cuts listed in Table 4.1 in order to size down the background efficiently. However, one has an additional handle in the form of large $\not{E}_T$, since the production process is $pp \rightarrow \eta_3^\pm \psi$, and ψ is a massive neutral fermion whose decay rate is again suppressed by $\frac{1}{\Lambda^2}$. Thus we have put an additional cut $\not{E}_T > 150$ GeV to reduce the back-

50

Signal	Benchmark point	$\int \mathcal{L} dt$ for 5σ	N_S	N_B	N_S/N_B
Opposite Sign	BP1	92.95	92	248	0.37
Charged Track	BP2	263.23	146	702	0.21
Single Charged	BP1	(A)340.40	841	27436	0.030
Track $+ \not{E}_T$		(B) 24.81	46	40	1.150
	BP2	(A)1076.19	1485	86741	0.017
		(B) 56.60	62	91	0.681

Table 3.4: Integrated luminosity (fb^{-1}) required to attain 5σ statistical significance for opposite sign charged tracks and single charged track $+\not{E}_T$ signals for the considered Benchmark points of Table 3.2 in the Type III seesaw with a sterile neutrino model during 14 TeV run of LHC.

ground substantially. The $\not{E}_T$ distribution for background and signal events are shown in Figure 3.6. After putting the $\not{E}_T$ cut along with cut set A of Table 4.1 the background cross-section reduces to 80.6 fb.

The required integrated luminosities to reach 5σ statistical significance for this signal(using cut set (A)) during 14 TeV run of LHC for each of the benchmark points is tabulated in Table 3.4. If in addition we consider the cosmic ray muon background to be one order of magnitude larger than that with dimuons, even then one obtain 5σ statistical significance for BP1(BP2) with an integrated luminosity 343(1080) fb^{-1}. The difference is small because the SM background at LHC is dominant.

The production cross section for single charged track $+\not{E}_T$ is large compared to the opposite-sign charged track in Type III seesaw with sterile neutrino model. However, the huge single muon SM background pushes towards higher luminosities to reach 5σ statistical significance compared to the opposite sign stable charge track signal. If we impose the cut-set (B), which applies a more stringent cut on β, together with a $\not{E}_T$-cut of 150 GeV, the SM background can be reduced enormously. Thus one can probe this signal at a much lower value of integrated luminosity as shown in Table 3.4.

However, although cut-set (B) eliminates the SM background completely in all other cases, the results do not improve much, as the SM background in those cases is already small enough after the imposition of cut (A).

51
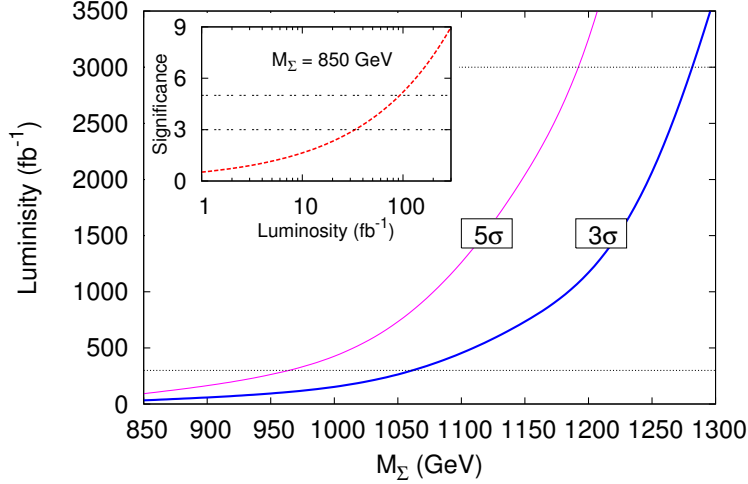
Figure 3.5: Projection of 3σ(blue) and 5σ(magenta) significance contours as a function of HSCP mass and integrated luminosity for the Type III seesaw with a sterile neutrino. Inset depicts the significance of BP1 with integrated luminosity during 14 TeV runs of LHC.

3.4.2 Inert doublet model with right-handed Majorana neutrino

Opposite-sign stable charged tracks of $H^{\pm}H^{\mp}$

The $H^{\pm}$ particles are massive and the strong p_T-and β-cuts as listed in Table 4.1 are quite effective in reducing the SM backgrounds drastically. Hence the lion's share of the background contribution comes from the cosmic ray muons. The required integrated luminosities for 5σ statistical significance for the considered benchmark points is shown in Table 3.5.

Signal	Benchmark point	$\int \mathcal{L} dt$ for 5σ	N_S	N_B	N_S/N_B
Opposite Sign	BP1	97.81	94	261	0.36
Charged Track	BP2	195.16	127	520	0.24
Same Sign	BP1	71.62	67	115	0.58
Charged Track	BP2	137.45	88	220	0.40

Table 3.5: Integrated luminosity(fb^{-1}) required to attain 5σ statistical significance for $H^{\pm} H^{\mp}$ signal for the considered benchmark points during 14 TeV run of LHC.
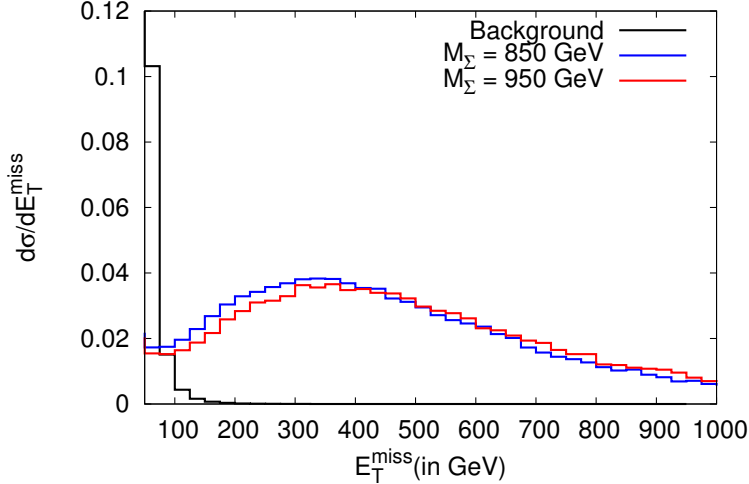
Figure 3.6: $\not{E}_T$ distribution of the single heavy stable charged tracks of $\eta_3^\pm + \not{E}_T$ for the benchmark points BP1(blue) and BP2(red) as in Table 3.2. Background $\not{E}_T$ distribution is shown in black.

The required integrated luminosities to obtain 5σ(magenta) and 3σ(blue) statistical significance for different values of $M_{H^\pm}$ is shown in figure 3.7. Clearly one can see that with $3000(300) fb^{-1}$ of integrated luminosity this model can be tested up to $M_{H^\pm} = 880(720)$ GeV with 3σ significance. The 5σ discovery limit for this model is $M_{H^\pm} = 800(630)$ GeV with integrated luminosity of $3000(300)\ fb^{-1}$. The slightly lower reach compared to the previous case can be attributed to the lack of enhancement via polarisation sum, when it comes to the production of the quasi-stable charged scalar. In spite of this small degree of suppression, it is clear that here, too, the high energy run of the LHC should reveal signals of such a scenario (as well as the previous one discussed here) even before the high luminosity run begins.

Same-sign stable charged tracks of $H^\pm H^\pm$

While single track events are not expected here because of the short-lived nature of $H^0(A^0)$, one anticipates same-sign charged track pairs in this case, as has been mentioned already. Here too, the p_T-and β-cuts (of the values (A)) suffice to suppress all SM background. However, we have also introduced a third-muon veto to further reduce such background. Since there is no Drell-Yan production of same-sign dimuons, these criteria eliminates the SM background almost completely, leaving only cosmic ray muons. Once more, we have

53
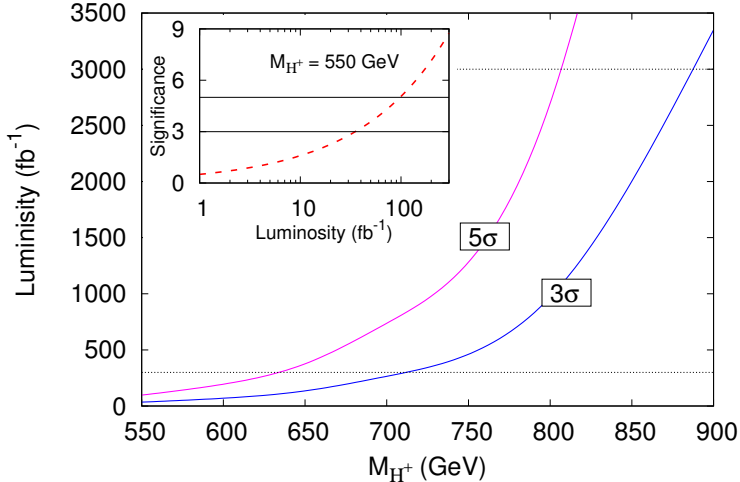
Figure 3.7: Projection of 3σ(blue) and 5σ(magenta) significance contours for the opposite-sign charged tracks as a function of HSCP mass and integrated luminosity for the IDM with a RH Majorana neutrino. Inset depicts the significance of BP1 with integrated luminosity during 14 TeV runs of LHC.

assumed the same rate as in the case of opposite sign charged track pairs. The required integrated luminosity for 5σ statistical significance for the considered benchmark points is shown in Table 3.5. The figures in that table indicate that the luminosity requirements for same-and opposite-sign tracks are comparable. This is because $pp \rightarrow H^0(A^0)H^\pm$ yields both type of track pairs. While the latter signal has additional contributions from s-channel H^+H^- production, the SM backgrounds for opposite track pairs are also more copious. This is mainly because large mass splittings between charged and neutral higgses is prohibited by the requirement of perturbative unitarity of scalar quartic couplings and also the fact that Z_2 symmetry prevents mixing between two higgs doublets. Thus we have only a minor excess of opposite-sign track pair events. The variation of statistical significance of this signal with integrated luminosity is shown in Figure 3.8.

The same-sign charged track pairs is a unique feature of this model and largely depends on the mass of heavy scalar and pseudoscalar. We found that for $M_{H^\pm} = 550$ GeV perturbative unitarity dictates $M_{H^0/A^0} \simeq 800$ GeV and the production cross-section for same sign track is 0.2 fb and can be discovered at 5σ with an integrated luminosity of 2500 fb^{-1}. Beyond this mass one has to rely on opposite-sign charged tracks to search for the IDM model with a RH Majorana neutrino with superweak interaction.
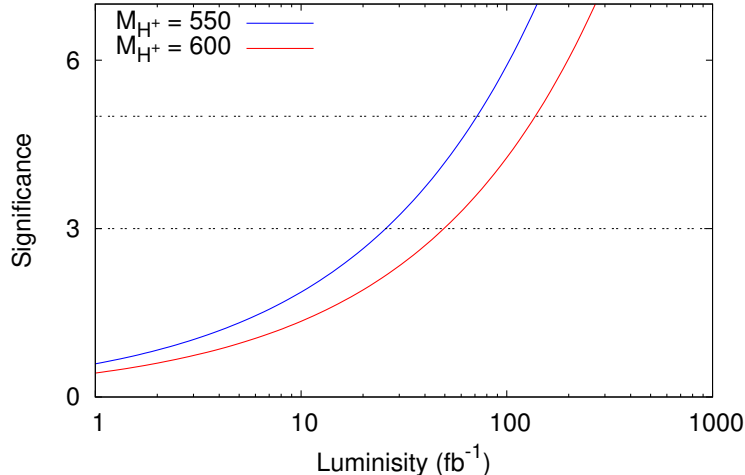
Figure 3.8: Variation of statistical significance of the considered benchmark points with integrated luminosity(fb^{-1}) for same-sign double charged tracks.

3.5 Conclusion

In this chapter we have presented two non-supersymmetric models of feebly interacting DM. These are a variant of Type III seesaw with a sterile neutrino and the inert doublet model (IDM) with at least one right-handed Majorana neutrino. We have analyzed and constrained the parameter space where the DM candidate is a *SuperWIMP* dark matter. In both the models the next-to-lightest-particle is electrically charged and long lived which decays to DM to yield correct CDM relic density. The lifetime of these NLOPs are large enough to pass through the detector but decays within 100 sec and do not disturb the BBN.

We have identified a few benchmark points within the constrained model parameter space and studied the collider prospect of the stable charged particles at the 14 TeV run of the LHC. For the Type III seesaw with sterile neutrino model we have considered the opposite sign charged track and also single charged track with large $\not{E}_T$. The IDM with right-handed Majorana neutrino model gives rise to both same-sign and opposite-sign charged tracks. These 'alternative' subsidiary signals may be helpful in differentiating between two theoretical frameworks, both of which admit a stable charged NLOP.

We have presented the discovery potential for two benchmark points for each scenario. The Type-III case allows one to probe higher mass ranges because of the enhancement of production cross-section via fermion polarization summation. We find that the extension of Type III Seesaw including a sterile neutrino can be probed about 960(1190)GeV with

300(3000) fb^{-1}, whereas the IDM with right-handed Majorana neutrino model can be explored up to 630(800)GeV. It should also be noted that the above results use leading order production rates for the NLOP, while the background rates used have taken into account higher order enhancements (NLO/NNLO/N^{3}LO). Thus the search limits predicted are on the conservative side, and one may expect even more optimistic results, once higher-order contributions to the signal(s) are included [151–153].

Chapter 4

Long-lived stau, sneutrino dark matter and right-slepton spectrum

4.1 Introduction

As we have discussed in considerable details in chapters 1 and 2, the suppressed interaction strength of a FIMP DM with rest of the particle spectrum disallows its detection in direct search experiments via DM-neucleon scatterings [1] or in indirect search experiments via the pair annihilations of such DM candidates. On the other hand, though such scenarios are unlikely to produce any $\not{E}_T$ signature in the colliders, there can be alternative signals coming in the form of heavy stable charged tracks. While two such examples of non-supersymmetric FIMP DM scenarios have already been studied in chapter 3, a case of study in this chapter is the MSSM augmented with right-chiral neutrino superfields, with a right-sneutrino becoming the DM candidate [157, 158] [2].

The above possibility is a natural extension of the MSSM. Consider, as the simplest example, a right-chiral neutrino superfield for each family, with just Dirac masses for neutrinos. Such a superfield, being a SM gauge singlet, has only Yukawa interactions with the rest of the extended MSSM spectrum. Recent neutrino data constrain such couplings to rather small values ($y_\nu \simeq 10^{-13}$) [163]. If the sfermion masses evolve down to the TeV-scale

---

[1]Note however that some future experiments will be able to probe typical FIMP-electron scattering cross-sections [154–156].

[2]It is important to note that a left-handed tau sneutrino, even when lighter than the lightest neutralino, will not serve as a thermal DM candidate, as it is excluded by direct detection experiments [26, 159–162].

from some high-energy values (not necessarily unified), then the mass parameters for all gauge non-singlet fields tend to go up through running induced by renormalisation group equations [164]. Running of the mass parameter corresponding to $\tilde{\nu}$, the superpartners of right-handed neutrinos, is, however, negligibly small. Thus one of the right-sneutrinos is very likely to become the lightest supersymmetric particle (LSP) and consequently a DM candidate in such a case. Moreover, the right stau ($\tilde{\tau}_R$) can quite conceivably become the next-to-lightest supersymmetric particle (NLSP) [3], since its Yukawa coupling is relatively large. The $\tilde{\nu}$, however, has extremely weak interactions with the rest of the MSSM spectrum, thus it typically does not reach thermal equilibrium with other particles in the early Universe.

As has been pointed out in a series of studies [62, 120–126], such a scenario leads to a very characteristic signal in collider detectors if the NLSP is indeed the right-chiral stau.All SUSY cascades at the LHC should then end up producing stau ($\tilde{\tau}_R$) pairs along with some SM particles. These stau ($\tilde{\tau}_R$)-pairs will not decay into $\tilde{\nu}$s within the detector due to the small y_ν and will travel all the way through, leaving their signature as massive charged tracks [4]. Such tracks can be distinguished from muonic tracks through event selection criteria such as track-p_T and the time delay between the inner tracker and the muon chamber [170], as discussed in chapter 2.

Since the signal and the SUSY spectrum here are both quite different from the well-studied case of a neutralino LSP, it is important to reconstruct the superparticle masses in a scenario of this kind. Apart from collider phenomenology, the knowledge about the spectrum can reveal clues on the SUSY-breaking mechanism that is operative here. The $\tilde{\nu}$ DM candidate, of course, is illusive, since it is not even produced within the detector. The mass reconstruction procedures for neutralinos, charginos and left-chiral sleptons have been worked out in earlier works [120, 121, 171, 172]. While the $\tilde{\tau}_R$-mass can be obtained from time-delay measurements, we pay special attention here to the mass reconstruction for the right-chiral smuon as well as the corresponding selectron, which thus yields a picture of the slepton flavour structure of the underlying theory.

In addition to the kinematic variables used earlier [62, 120, 121, 126, 171, 172], notably the

---

[3]In fact the second lightest sneutrino, which we will assume to be almost degenerate with the sneutrino LSP, is strictly speaking the NLSP. However, since the two additional sneutrinos have no impact on the collider phenomenology, we will loosely use NLSP to designate the lightest charged particle.

[4]Right-handed sneutrinos in certain simplified extensions of the MSSM can behave as WIMP DM candidates, which leave their footprints in the form of MET, in colliders [165–168]. Similar signatures are also obtained in supersymmetric $B - L$ extensions of the SM [169].

p_T of the hardest jet and missing energy, $\not{E}_T$, we have formulated event selection criteria based on additional quantities such as the stransverse mass, M_{T2} [173, 174], to gain some insight into the right slepton mass hierarchy. Our reconstruction procedure is applicable to right-smuons as well as selectrons for both the cases where they are heavier and lighter than the lightest neutralino ($\tilde{\chi}_1^0$).

This chapter is organised as follows: In section 4.2 we discuss the model considered along with the constraints imposed from both colliders results and cosmology. In section 4.3 we discuss the supersymmetric signals that we analyse, along with the strategy for the reconstruction of the slepton masses. Section 4.4 contains the benchmark points chosen for different case studies together with an analysis of the discovery prospects corresponding to the signatures considered in upcoming runs of LHC at an integrated luminosity of $\mathcal{L} = 3000$ fb^{-1}. The M_{T2} and slepton mass ($m_{\tilde{l}}$) distributions for the two different mass orderings considered are also studied in section 4.4. Finally we summarise and conclude in section 4.5.

4.2 The theoretical scenario, the spectrum and its constraints

We consider the MSSM supplemented with three families of right-handed (RH) neutrino superfields ($\hat{\nu}_R$) with Dirac mass terms for the neutrinos. Hence the superpotential (suppressing family indices) becomes

$$W = W_{MSSM} + y_\nu \, \hat{H}_u \, \hat{L} \hat{\nu}_R^c, \tag{4.2.1}$$

where W_{MSSM} is the superpotential of the MSSM, y_ν is the neutrino Yukawa coupling, $\hat{L} = (\hat{\nu}_L, \hat{l}_L)$ is the left-handed (LH) lepton superfield and H_u is the Higgs doublet that couples to the up-type quarks. The physical states dominated by right sneutrinos ($\tilde{\nu}$) have all their interactions proportional to y_ν. For simplicity, we consider a scenario where all (right) sneutrinos are degenerate and the sneutrino mass matrix is diagonal. After electroweak symmetry breaking, the neutrinos acquire masses as shown below

$$m_\nu = \frac{y_\nu}{\sqrt{2}} v \sin \beta, \tag{4.2.2}$$

where $v \simeq 246.2$ GeV and $\tan \beta = \frac{\langle H_u^0 \rangle}{\langle H_d^0 \rangle}$. Recent data from global fits on neutrino oscillation and cosmological bound on the sum of neutrino masses, constrain the largest Yukawa coupling in the range $2.8 \times 10^{-13} \lesssim (y_\nu \sin \beta) \lesssim 4.4 \times 10^{-13}$ [126]. The lower bound is taken from

a global fit on the neutrino oscillation parameters in the normal hierarchy scenario [163], while the upper bound is obtained from a combination of Planck, lensing and baryon acoustic oscillation data [10]. The latter bound can vary roughly by a factor of two depending on the set of cosmological data included in the fit [5].

Barring the right neutrino superfields, we consider the phenomenologically constructed MSSM (pMSSM) [176]. Thus the soft SUSY breaking terms are free parameters. The addition of the RH neutrino superfield entails the following additional soft terms in the MSSM Lagrangian:

$$-\mathcal{L}_{soft} \supset m_{\tilde{\nu}}^2 |\tilde{\nu}|^2 + (y_\nu A_\nu H_u \tilde{L} \tilde{\nu}^c + h.c.), \tag{4.2.3}$$

where A_ν plays a role in the left-right mixing in the sneutrino sector. The sneutrino mass matrix is defined as

$$\mathcal{M}_{\tilde{\nu}}^2 = \begin{bmatrix} m_{\tilde{\nu}_L}^2 & -y_\nu v \sin\beta \, (\mu \cot\beta - A_\nu) \\ -y_\nu^\dagger v \sin\beta \, (\mu^* \cot\beta - A_\nu^*) & m_{\tilde{\nu}}^2 \end{bmatrix} \tag{4.2.4}$$

where $m_{\tilde{\nu}_L}$ and $m_{\tilde{\nu}}$ are respectively the soft scalar masses for the left- and right-chiral sneutrinos and μ is the higgsino mass paremeter. One then finds that the left-right sneutrino mixing angle, $\tilde{\Theta}$, can be written as

$$\tan 2\tilde{\Theta} = \frac{2 \, y_\nu \, v \, \sin\beta \, |\mu \cot\beta - A_\nu|}{m_{\tilde{\nu}_L}^2 - m_{\tilde{\nu}}^2}, \tag{4.2.5}$$

thus implying that the admixture of $SU(2)$ doublets in the $\tilde{\nu}$-dominated mass eigenstates are limited by the neutrino Yukawa couplings.

As mentioned in sec. 4.1, the present study focuses on scenarios with the lighter stau ($\tilde{\tau}_1$) as the NLSP. Such a stau, upon production at the LHC, will eventually decay into the right sneutrino LSP through modes such as $\tilde{\tau}_1 \to W^{(*)}\tilde{\nu}$, driven, as expected, by the neutrino Yukawa coupling. For $m_{\tilde{\tau}_1} > m_{\tilde{\nu}} + m_W$, the width of the above two-body decay is given by

$$\Gamma_{\tilde{\tau}_1} \simeq \Gamma_{\tilde{\tau}_1 \to W\tilde{\nu}} = \frac{g^2 \tilde{\Theta}^2}{32 \, \pi} |U_{L1}^{(\tilde{\tau}_1)}|^2 \frac{m_{\tilde{\tau}_1}^3}{m_W^2} \left[1 - \frac{2(m_{\tilde{\nu}}^2 + m_W^2)}{m_{\tilde{\tau}_1}^2} + \frac{(m_{\tilde{\nu}}^2 - m_W^2)^2}{m_{\tilde{\tau}_1}^4} \right]^{3/2}, \tag{4.2.6}$$

where g is the $SU(2)_L$ gauge coupling, m_W the W-boson mass and $U^{(\tilde{\tau}_1)}$ parametrises the left-right mixing of the staus. Assuming A_ν is of the same order as the other trilinear couplings, the $\tilde{\tau}_1$s are fairly long-lived with a typical life-time of $\mathcal{O}(1)$ sec for all the benchmark points that we will consider in section 4.4. Thus, the decay length of $\tilde{\tau}_1$ is large compared to the

---

[5]For a recent compilation see Ref. [175].

typical collider scale. All processes at the LHC, which are initiated with the production of superparticles, will ultimately lead to the production of a pair of quasi-stable $\tilde{\tau}_1$s which will travel all the way up to the muon-chamber. In addition to making the NLSP stable at the collider scale, the smallness of y_ν also implies an out-of-equilibrium decay of the NLSP in the early universe into the $\tilde{\nu}$ LSP. The contribution to the $\tilde{\nu}$ relic density has two components. The first of which arises from the decay of the stau after it freezes out, and can be estimated from eqn. 2.1.5 (see chapter 2), by replacing $m_\chi \equiv m_{\tilde{\nu}}$ and $m_A \equiv m_{\tilde{\tau}_1}$,

$$\Omega_{\tilde{\nu}}^{FO} h^2 = \frac{m_{\tilde{\nu}}}{m_{\tilde{\tau}_1}} \Omega_{\tilde{\tau}_1} h^2, \tag{4.2.7}$$

where $\Omega_{\tilde{\tau}_1} h^2$ is the (thermal) relic density of the quasi-stable NLSP when it freezes out. The contribution $\Omega_{\tilde{\tau}_1} h^2$ can be calculated using a standard package such as `microOMEGAs` [177].

In addition to the contribution ensuing from the out-of equilibrium decay of the $\tilde{\tau}_1$ NLSP, the remaining heavy supersymmetric particles, *viz.*, the left-handed sleptons, left-handed sneutrinos, neutralinos, charginos etc., may also decay while still in thermal equilibrium (see appendix A.2). These latter contributions which arise from the freeze-in mechanism [48,178] can be obtained from eqn A.2.8

$$\Omega_{\tilde{\nu}}^{FI} h^2 \simeq \frac{1.09 \times 10^{27}}{g^{*\,3/2}} m_{\tilde{\nu}} \sum_i \frac{g_i \Gamma_i}{m_i^2} \tag{4.2.8}$$

where $g^* \approx 106.75$ [157], is the average number of effective degrees of freedom contributing to the thermal bath, and the sum runs over all the aforementioned relevant superparticles. Besides, Γ_i, m_i and g_i are respectively the decaywidth to $\tilde{\nu}$, mass, and degrees of freedom of the ith superparticle. The decaywidths of several such superparticles into $\tilde{\nu}$ are listed in Ref. [157] as well as in appendix A.2. Thus, the total relic density of the sneutrinos is given as

$$\Omega_{\tilde{\nu}} h^2 = \Omega_{\tilde{\nu}}^{FO} h^2 + \Omega_{\tilde{\nu}}^{FI} h^2 \tag{4.2.9}$$

We by and large assume the three right-handed sneutrinos to be mass degenerate. However, this assumption may not be realised in practice, and one may encounter small splittings among the three families. In such cases, the heavier right-handed mass eigenstates, *viz.*, $\tilde{\nu}^{e,\mu}$, may in principle be produced from the decay of heavier superparticles following equation (4.2.8). These $\tilde{\nu}^{e,\mu}$ when produced, will ultimately decay into the $\tilde{\nu}$ LSP. However, these decays are suppressed by two powers of the neutrino Yukawa coupling, and hence almost always have lifetimes greater than the present age of the universe (for example see chapter 5). Therefore, the two other $\tilde{\nu}$-dominated states will make a substantial contribution

to the relic density regardless of whether the the three $\tilde{\nu}$s are mass degenerate or not. Thus, the $\Omega_{\tilde{\nu}}^{FI} h^2$ must also include the abundances of $\tilde{\nu}^{e,\mu}$.

So far, we have discussed only about the $\tilde{\nu}$ LSP and $\tilde{\tau}_1$ NLSP. However, depending on the details of the SUSY breaking scheme, one can have various mass hierarchies in the non-strongly interacting superparticle sector, particularly in the masses of the right-chiral smuon and the selectron, which we assume to be degenerate and heavier than the stau NLSP, with respect to the lightest neutralino mass, $m_{\tilde{\chi}_1^0}$. Hence, one may encounter two distinct mass orderings between these particles, *viz.*,

$$\text{Case I} \quad : \quad m_{\tilde{\chi}_1^0} > m_{\tilde{\mu}_R} = m_{\tilde{e}_R}, \tag{4.2.10}$$

and

$$\text{Case II} \quad : \quad m_{\tilde{\mu}_R} = m_{\tilde{e}_R} > m_{\tilde{\chi}_1^0}, \tag{4.2.11}$$

These different hierarchies may leave their markedly unique footprints in collider signals. Hence, experimentally identifying the relevant mass ordering may unveil the physics behind the SUSY breaking. Thus, the main focus of this present work is to understand the effects of these hierarchies on the collider signals and to devise strategies to separate one from the other. However, before detailing the analyses dedicated solely for the discrimination in the two hierarchies at the high luminosity run of the LHC (HL-LHC), we ensure that our benchmark points satisfy all the following constraints.

- The mass of the lightest CP-even Higgs is required to lie in the range 123 GeV $<$ $m_{h^0} < 128$ GeV, which is consistent with the Higgs mass measurements from various channels at the LHC [179, 180].

- The signal strengths of the SM-like Higgs boson are required to lie within the experimentally measured values and their uncertainties [181, 182]. We use `LILITH` [183] in order to compute the likelihood function and require them to be ~ 1 for all our chosen benchmark points (BPs). Furthermore, we also perform a cross-check and find that the signal strengths in the individual Higgs decay channels lie within their experimental uncertainties upon employing the `HiggsBounds` package [184].

- We impose that the relic density of the LSP, $\Omega_{\tilde{\nu}} h^2$, satisfies the upper bound (at the 2σ level) obtained by PLANCK, namely $\Omega_{DM} h^2 = 0.1199 \pm 0.0027$ [10].

- In order to avoid destroying the successful predictions of the light element abundance from BBN, we require that the stau NLSP lifetime does not exceed 100 seconds [126, 185, 186].

- The current model-independent studies on heavy stable charged tracks from the LHC requires $\tilde{\tau}_1 > 360$ GeV, as obtained by CMS for a pair produced scenario [132].

- Furthermore, we demand the gluino and squark masses to be $m_{\tilde{g}} > 2.1$ TeV, $m_{\tilde{q}} > 1.4$ TeV and $m_{\tilde{t}} > 1.1$ TeV from recent available bounds from the LHC [187, 188]. These limits are based on searches in the jets $+ \not{E}_T$ channel, which are relevant for the MSSM with a neutralino LSP. However, in the absence of any dedicated SUSY search results based on stable charged track signals, we conservatively use the aforementioned limits.

4.3   Mass reconstruction strategy

In order to decipher the actual ordering of the masses in the SUSY electroweak sector, in particular of $\tilde{\chi}_1^0$ and $\tilde{\mu}_R/\tilde{e}_R$, we have to reconstruct the following three particles, *viz.*, $\tilde{\tau}_1$, $\tilde{\chi}_1^0$ and $\tilde{\mu}_R/\tilde{e}_R$, with the $\tilde{\mu}_R$ and $\tilde{e}_R$ being considered to be degenerate in mass. As discussed above, the mass of the $\tilde{\tau}_1$ can be reconstructed using the time-of-flight measurements following [126, 170] while the neutralino($\tilde{\chi}_1^0$) reconstruction can easily be performed using the procedure envisioned in Ref. [121]. For completeness, we briefly summarise these two strategies.

$\tilde{\tau}_1$ **reconstruction:** As $\tilde{\tau}_1$s are very heavy, typically $\mathcal{O}(100)$ GeV particles, they are slow. Their velocity distributions can be obtained using the time delay between the production of $\tilde{\tau}_1$s at the interaction point and their detection in the muon chamber. Combining this with the momentum measured in the muon chamber, one can reconstruct the $\tilde{\tau}_1$ mass by exploiting the relation,

$$m_{\tilde{\tau}_1} = \frac{p}{\beta\,\gamma}, \tag{4.3.1}$$

where p, β and γ are respectively the momentum, speed with respect to the speed of light and the Lorentz factor, of the $\tilde{\tau}_1$. In order to be fairly realistic with the experimental situation, we smear the actual velocity of $\tilde{\tau}_1$s with the Gaussian (Box-Muller) prescription by choosing a standard deviation of $\sigma_\beta = 0.024$, upon following ATLAS' calibration [67].

$\tilde{\chi}_1^0$ **reconstruction:** Following the prescription of ref. [121], in order to reconstruct the $\tilde{\chi}_1^0$ mass, one may look for $2\tilde{\tau}_1 + 2\tau$ states, dominantly produced by $\tilde{q}, \tilde{g}$ initiated cascades. The invariant mass distributions of these $\tilde{\tau}_1 + \tau$ pairs will peak around the $\tilde{\chi}_1^0$ mass. The most challenging part of this technique is the reconstruction of τs because of their semi-invisible decays. To tackle this difficulty of reconstructing the τ masses, we employ the collinear

approximation as described below.

Collinear Approximation: Following the method described in [189], one can fully reconstruct the τs with the knowledge of the fraction, $x_{\tau_{c_i}}$ $(i = 1, 2)$, of the parent τ momentum carried by the ensuing visible charged jet or lepton. Each event has two unknowns, *viz.*, the two components of the momenta of the neutrinos (one (two) neutrino(s) per hadronic (leptonic) τ decay). These two unknowns can be solved on an event-by-event basis upon knowing the two components of the missing transverse energy, $\vec{\not{E}}_T$. If $p_{\tau_i}^\mu$ and $p_{\tau_{c_i}}^\mu$ are the four momenta of the two parent τ-leptons and the corresponding visible charged objects, then one has

$$p_{\tau_{c_i}}^\mu = x_{\tau_{c_i}}\, p_{\tau_i}^\mu, \tag{4.3.2}$$

and one obtains

$$\vec{\not{E}}_T = \left(\frac{1}{x_{\tau_{c_1}}} - 1\right)\vec{p}_{\tau_{c_1}} + \left(\frac{1}{x_{\tau_{c_2}}} - 1\right)\vec{p}_{\tau_{c_2}}, \tag{4.3.3}$$

where the τ has been considered to be massless and the neutrinos from these τ decays are assumed to be collinear in the direction of their corresponding visible charged objects. Provided the decay products are not back-to-back, the above equation provides two conditions (from the x- and y-components of $\vec{\not{E}}_T$) for $x_{\tau_{c_i}}$ and one finally obtains the τ momenta as $p_{\tau_{c_i}}/x_{\tau_{c_i}}$.

Slepton reconstruction: Finally, in order to reconstruct the slepton masses $(m_{\tilde{\mu}_R}, m_{\tilde{e}_R})$, we consider the Drell-Yan production of $\tilde{\mu}_R \tilde{\mu}_R^* (\tilde{e}_R \tilde{e}_R^*)$ followed by the slepton's decay into a lepton (μ/e), a $\tilde{\tau}_1$ and a τ, mediated by an off-shell or an on-shell $\tilde{\chi}_1^0$ depending on their mass ordering. The topology of the process is shown in the left panel of Fig. 4.1. In the following, for both hierarchies mentioned in Eqs. 4.2.10 and 4.2.11 we investigate the two possible signatures,

- 2 $\tilde{\tau}_1$s + 2 opposite sign same flavour leptons (OSSF) + 1 τ-tagged jet + $\not{E}_T$

- 2 $\tilde{\tau}_1$s + 2 opposite sign same flavour leptons (OSSF) + 2 τ-tagged jet + $\not{E}_T$.

To reconstruct the slepton mass, we utilise the popular stransverse mass variable, M_{T2} [173, 174]. In general, M_{T2} is a useful variable for measuring the mass of a particle when it is pair-produced in a hadron collider and thereafter decays into a visible object along with invisible particles, thus giving rise to missing transverse momentum. Hence, the M_{T2} variable can be relevant for the reconstruction of slepton masses for the first signature involving a single τ-tagged jet. The variable M_{T2} is defined as

$$M_{T2} \equiv \min_{\vec{\not{p}}_{T,1} + \vec{\not{p}}_{T,2} = \vec{\not{E}}_T} \left(\max\left\{ m_T(\vec{p}_{T,1}, \vec{\not{p}}_{T,1}, m, m_{inv}), m_T(\vec{p}_{T,2}, \vec{\not{p}}_{T,2}, m, m_{inv}) \right\} \right), \tag{4.3.4}$$
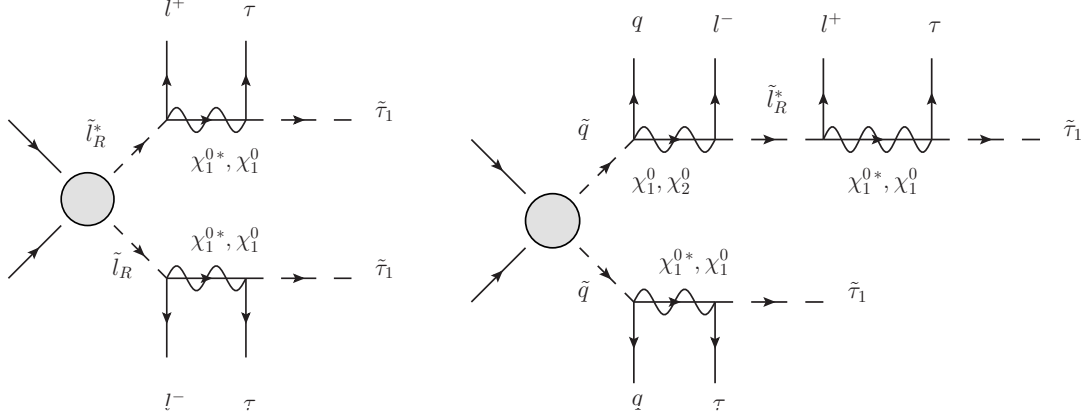
Figure 4.1: Representative diagrams for the Drell-Yan production of $\tilde{l}_R$ is shown in the left. The right panel illustrates a SUSY cascade process initiated by SUSY particles from the strong sector that mimics the final state of the left panel, modulo hard jets.

where $m, \vec{p}_{T,i}, \vec{\not{p}}_{T,i}$ and m_{inv} are respectively the mass of the visible objects, transverse momenta of the visible objects, the missing transverse momenta and the mass of the invisible particles in the ith leg and m_T refers to the standard transverse mass variable. The actual mass of the mother particle will always be bounded from below by M_{T2} and hence the end point of the M_{T2} distribution will give a fairly accurate estimate of its mass. The above definition is slightly modified to accept asymmetries, which leads us to the asymmetric M_{T2} variable [190] and is shown to be more useful than its symmetric counterpart while reconstructing the slepton masses. The asymmetric M_{T2} variable is defined as

$$M_{T2} \equiv \min_{\vec{\not{p}}_{T,1}+\vec{\not{p}}_{T,2}=\vec{\not{E}}_T} \left(\max\left\{ m_T(\vec{p}_{T,1}, \vec{\not{p}}_{T,1}, m_1, m_{inv,1}), m_T(\vec{p}_{T,2}, \vec{\not{p}}_{T,2}, m_2, m_{inv,2}) \right\} \right), \quad (4.3.5)$$

with different masses for the invisible particles in the two legs. For our first scenario involving a single τ-tagged jet, the other visible τ decay product escape the detector undetected. Hence the two visible particles (in each leg) required to construct the asymmetric M_{T2} are the $\tilde{\tau}_1$ along with its nearest (in the η-ϕ plane) lepton. The τ-tagged jet is considered to be part of that leg for which it is nearest (in its $\Delta R = \sqrt{\Delta\eta^2 + \Delta\phi^2}$ separation) to the $\tilde{\tau}_1$ and it is thus combined with the corresponding $\tilde{\tau}_1\ell$ pair. Hence, both the ν_τ and the undetected τ-jet/τ-lepton contribute to $\not{E}_T$ in this case. Owing to the smallness of the mass of the τ, one can safely use $m_{inv,1} = m_{inv,2} \simeq 0$ while constructing the M_{T2} variable. The asymmetric M_{T2} variable constructed in this way will be bounded above by $m_{\tilde{\mu}_R(\tilde{e}_R)}$.

For the signature involving double τ-tagging, we fully reconstruct both the sleptons upon

using the invariant masses of the three individually reconstructible objects, $viz.$, $\tilde{\tau}_1, \tau$ and $\ell^{\pm}$. The τs for this analysis are reconstructed according to the collinear approximation discussed above. In order to reconstruct both the sleptons properly, we construct all possible pairs of invariant masses $m_{\tilde{\tau}_1\,\tau\,l^{\pm}}$ and compute the difference between the invariant masses of each pair. The pair yielding the least difference in the invariant mass is regarded as the correct pair.

Lastly, pair production of strongly interacting superparticles also leads to similar final states but exhibit different topologies (as shown in Fig 4.1 (right)), namely the cascade decay has additional jets at the parton level. Hence, one cannot use the aforementioned procedures for slepton mass reconstruction for such processes. Our strategy is to choose cuts in order to suppress the contribution of processes initiated by strongly interacting particles. The cascade processes will always give rise to harder jets, to higher jet multiplicities and to a harder $\not{E}_T$ distribution as compared with DY production. Hence a hard cut on the p_T of the hardest jet as well as a cut on the jet multiplicity for jets above a certain threshold p_T ~ 100 GeV, and a hard upper cut on the $\not{E}_T$ can efficiently reduce the effects of the cascade processes, as we will see below. Moreover as $\not{E}_T$ plays an important role in the construction of the M_{T2} variable, which will, at the end be our most important observable for the mass reconstruction of the sleptons, removing the cascade processes with this cut will help in achieving faithful reconstructions of the sleptons.

4.3.1 Signal and background

In the remaining part of this section, we focus on the various details of our collider analyses. The presence of $\tilde{\tau}_1$s in the signal makes it easier to reduce the major SM backgrounds ensuing from the two real backgrounds, $viz.$, ZZZ and Zh and the following fakes, ZZ, $t\bar{t}Z$, and ZW^+W^-. All these SM backgrounds have been merged with up to two additional partons upon employing the MLM merging scheme [191] with appropriate choices for merging parameters. We ensure at least two muons, exactly two taus and two additional leptons (electrons or muons) for the real backgrounds. For the fake backgrounds, the additional merged jets will fake the tau jets or the leptons, as we will discuss below. As a means of discriminating the $\tilde{\tau}_1$s from the SM muons we have followed the footsteps of certain experimental analyses [66, 67] and impose hard cuts on the p_T of the two hardest muons (or $\tilde{\tau}_1$s for the signal) with an additional requirement of the $\tilde{\tau}_1/\mu$ speed to be $\beta(= \frac{p}{E}) < 0.95$.

For the collider analyses, we generate the signal and background samples along with their decays in the MadGraph5_aMC@NLO [142] framework. The parton showering and hadronisation

Parameter	$p_T(j_1)$	Number of jets with $p_T(j) > 100\text{GeV}$	$\not{E}_T$
Cut set A	< 200 GeV	< 2	< 150 GeV
Cut set B	< 200 GeV	< 2	< 200 GeV

Table 4.1: Selection cuts applied to suppress the squark-gluino processes. Here $p_T(j_1)$ refers to the transverse momentum of the hardest jet.

is done in `Pythia 8` [192]. The jets are constructed with the anti-kT [193] algorithm with a minimum p_T of 20 GeV and a jet parameter of $R = 0.4$, using the `FastJet` [194] package. Finally, we perform a fast detector analysis in the `Delphes 3` framework [144]. For all sample generations, we use the `NNPDF2.3` [195] parton distribution function set, at leading order (LO). The renormalisation and factorisation scales are set to the default dynamic values in `MadGraph5_aMC@NLO`. For the signal samples however, we use flat K-factors to approximately capture the next to leading order (NLO) effects. For this purpose, we determine our signal cross-sections at NLO with `Prospino2.0` [196] and scale the LO samples accordingly. Flat NLO K-factors for the backgrounds are computed within `MadGraph5_aMC@NLO` by taking the ratios of the unmerged cross-sections at NLO and LO. We scale the merged $ZZZ, Zh, ZZ, t\bar{t}Z$ and ZW^+W^- cross-sections by 1.53, 2.17 (which also includes a correction factor to the Higgs branching ratio), 1.48, 1.32 and 2.03 respectively. For the detector-level analyses, we employ the following cuts:

- For the two hardest muons ($\tilde{\tau}_1$s in the case of our signal), we require the transverse momenta of the these two objects to be $p_T^{\mu_{1,2}} > 70$ GeV, the speed, $\beta^{\mu_{1,2}} < 0.95$ and the rapidity to lie in the range, $|\eta(\mu_{1,2})| < 2.5$. Furthermore, we require these objects to be separated in the η-ϕ plane by $\Delta R(\mu_1, \mu_2) > 0.4$.

- For the remaining opposite-sign-same-flavour (OSSF) leptons (e, μ), we require, $p_T^\ell > 10$ GeV, $\beta(\ell) > 0.95$, $|\eta(\ell)| < 2.5$ and $\Delta R(\ell_1, \ell_2) > 0.2$.

- For all jets (quark/gluon initiated as well as τ-tagged ones), we demand the jets to have $p_T^j > 20$ GeV, $|\eta(j)| < 5$ and $\Delta R(j, j) > 0.4$.

- In addition, we require, $\Delta R(\mu_{1,2}, j) > 0.4$ and $\triangle R(\ell, j) > 0.4$.

Moreover, in order to suppress the squark-gluino contamination, we implement the additional cuts listed in Tab. 4.1. In Fig. 4.2, we sketch the β-distribution of the hardest muon/$\tilde{\tau}_1$
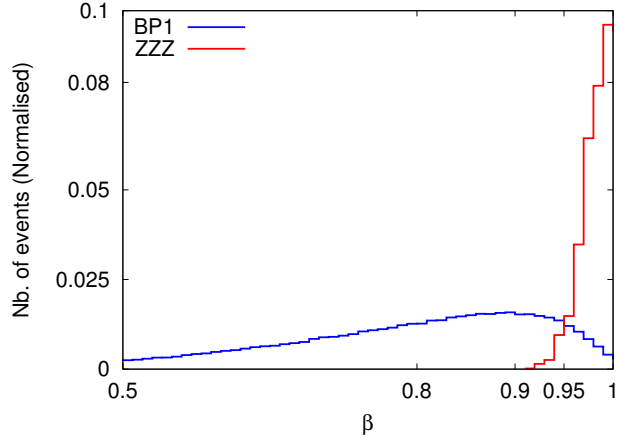
Figure 4.2: β-distribution for signals as well as background events are shown. The distribution clearly suggests that a negligible number of background events survives after the application of the β-cut as mentioned in the text.

for BP1 (as defined below) and for the ZZZ background, with the following values for the mean and rms, $\mu_{sig} = 0.768$, $\mu_{bkg} = 0.999$ and $\sigma_{sig} = 0.167$, $\sigma_{bkg} = 0.024$ [6]. One can clearly see that requiring $\beta \lesssim 0.95$ strongly suppresses the SM background events. Thus, geared with this setup, we proceed with the reconstruction of the slepton masses in the following section.

4.4   Results

In this section, we utilise the entire arsenal of techniques discussed above to finally show the viability of the slepton reconstructions and illustrate the possibility of probing the two mass hierarchies. For this purpose, we choose six benchmark points from the pMSSM spectrum, augmented with three additional families of sneutrino fields. We ensure that all these BPs abide by the constraints listed in section 4.2. Three of these BPs correspond to the case $m_{\tilde{\chi}_1^0} > m_{\tilde{\mu}_R, \tilde{e}_R}$ and are summarised in Tab. 4.2. The remaining three corresponding to $m_{\tilde{\chi}_1^0} < m_{\tilde{\mu}_R, \tilde{e}_R}$ are shown in Tab. 4.3.

Before commencing the collider study, we make a small digression to explain the factors contributing to the relic density. As is evident from Tables 4.2 and 4.3, for all our benchmark points, the $\tilde{\nu}$ relic density is in agreement with the value reported by the PLANCK

---

[6]The mean and the rms for the background are a result of the Gaussian smearing introduced by hand.

collaboration [10]. The dominant contribution comes from the *freeze-in* mechanism [7]. Even though the mass of the sneutrino LSP is not relevant for the collider analysis that follows, it directly affects the the relic density as is evident from equations (4.2.7) and (4.2.8). The neutrino trilinear coupling (A_ν) is also a deciding factor since it determines the decaywidths that control $\Omega_{\tilde{\nu}}^{FI}h^2$. On the one hand, large values of A_ν imply large $\Omega_{\tilde{\nu}}^{FI}h^2$, while in the other hand, a small A_ν increases the lifetime of $\tilde{\tau}_1$, thereby increasing the possibility of being strongly constrained by the BBN. As an example, in the case of BP3, as we increase A_ν from -2619 GeV to -400 GeV, the allowed value of $m_{\tilde{\nu}}$ increases from 39.2 GeV to 52.2 GeV [8], while the $\tilde{\tau}_1$ lifetime increases from ~ 2 seconds to ~ 94 seconds. Therefore, in our analysis we have fixed A_ν around the TeV-scale and thereby determine the allowed sneutrino mass ($m_{\tilde{\nu}}$) in order to saturate the abundance.

4.4.1 The primary channel: one τ-tagged jet

Our primary signature is comprised of events with two $\tilde{\tau}_1/\mu$ tracks, two OSSF leptons (electrons and muons), one τ-tagged jet along with $\not{E}_T$ and it obeys the topology in Fig. 4.1. As the efficiency of tagging a hadronically decaying τ-lepton is below 100%, a statistically significant number of events end up with a single τ-tagged jet. Thus, the final state having a single τ-tagged jet calls for the use of the asymmetric M_{T2} variable, which exhibits all the beneficial properties of the symmetric M_{T2} variable but with the additional advantage discussed in Sec. 4.3. For the present work, we consider a τ-tagging efficiency of 70% (60%) for the one- (three-) prong decay, as discussed in Ref. [197]. The efficiency of mis-tagging a QCD jet as a tau-tagged jet has been chosen to be $\sim 1\% - 2\%$.

The number of signal events surviving all the cuts, at an integrated luminosity $\mathcal{L} = 3000$ fb^{-1}, are tabulated in Tab. 4.4 for both the mass hierarchies. The numbers include contributions from the process of interest, *i.e.*, the Drell-Yan process as well as from the unwanted cascade topology. Both sets of cuts reduce the effect of the cascade contamination significantly. The M_{T2}-distributions for BP1 (case I) and BP4 (case II) are shown in Fig. 4.3 for the two sets of cuts which differ only in their upper limit for the missing transverse

---

[7]As an example, for BP3, with $A_\nu = -2619$ GeV and $m_{\tilde{\nu}} = 39.2$ GeV, we obtain $\Omega_{\tilde{\nu}}^{FI}h^2 \sim 0.114$ and $\Omega_{\tilde{\nu}}^{FO}h^2 \sim 0.006$. It might however be possible to have a larger freeze-out fraction by increasing the mass of the decaying supersymmetric particle as in such case the *freeze-in* contribution (Eq. (4.2.8)) is suppressed relative to the *freeze-out* contribution (Eq. (4.2.7)).

[8]For this case, the $\Omega_{\tilde{\nu}}^{FI}h^2$ and $\Omega_{\tilde{\nu}}^{FO}h^2$ change to ~ 0.112 and ~ 0.009 respectively, still keeping the *freeze-in* contribution almost an order of magnitude larger than its *freeze-out* counterpart.

Masses (in GeV)	BP1	BP2	BP3
$m_{\tilde{g}}$	2235	2200	2224
$m_{\tilde{u}_L}$, $m_{\tilde{c}_L}$	2004	2023	2124
$m_{\tilde{u}_R}$, $m_{\tilde{c}_R}$	1922	1919	2020
$m_{\tilde{d}_L}$, $m_{\tilde{s}_L}$	2005	2025	2125
$m_{\tilde{d}_R}$, $m_{\tilde{s}_R}$	1914	1920	2020
$m_{\tilde{t}_1}$	1218	1266	1373
$m_{\tilde{t}_2}$	1764	1741	1843
$m_{\tilde{b}_1}$	1705	1692	1797
$m_{\tilde{b}_2}$	1740	1732	1840
$m_{\chi_2^0}$	802	1009	942
$m_{\chi_1^\pm}$	802	1009	913
$m_{\tilde{\nu}_{e_L}}$, $m_{\tilde{\nu}_{\mu_L}}$	896	901	1011
$m_{\tilde{\nu}_{\tau_L}}$	855	857	911
$m_{\tilde{e}_L}$, $m_{\tilde{\mu}_L}$	900	905	1014
$m_{\tilde{\tau}_2}$	860	863	919
$m_{\tilde{\chi}_1^0}$	591	810	902
$m_{\tilde{\mu}_R}$, $m_{\tilde{e}_R}$	491	684	813
$m_{\tilde{\tau}_1}$	398	554	655
$m_{\tilde{\nu}}$	36.5	36.5	39.2
m_{h^0}	124	125	125
m_{A^0}	1696	1800	1800
$\tan\beta$	11.18	20.00	30.00
μ	1590	1200	930
$\Omega_{\tilde{\nu}}h^2$	0.1127	0.1128	0.1203
A_t	-2374	-2600	-2600
A_ν	-2619	-2619	-2619
$\|U_{L1}^{\tilde{\tau}_1}\|$	6.29×10^{-2}	1.11×10^{-1}	1.38×10^{-1}

Table 4.2: Benchmark points for studying the $m_{\tilde{\chi}_1^0} > m_{\tilde{\mu}_R,\tilde{e}_R}$ scenario.

Masses (in GeV)	BP4	BP5	BP6
$m_{\tilde{g}}$	2190	2253	2253
$m_{\tilde{u}_L}$, $m_{\tilde{c}_L}$	1967	2322	2322
$m_{\tilde{u}_R}$, $m_{\tilde{c}_R}$	1885	2120	2120
$m_{\tilde{d}_L}$, $m_{\tilde{s}_L}$	1968	2323	2323
$m_{\tilde{d}_R}$, $m_{\tilde{s}_R}$	1877	2121	2121
$m_{\tilde{t}_1}$	1182	1499	1500
$m_{\tilde{t}_2}$	1730	2037	2039
$m_{\tilde{b}_1}$	1666	1822	1827
$m_{\tilde{b}_2}$	1705	2013	2017
$m_{\chi_2^0}$	803	1017	1104
$m_{\chi_1^\pm}$	803	1017	1103
$m_{\tilde{\nu}_{e_L}}$, $m_{\tilde{\nu}_{\mu_L}}$	894	1203	1204
$m_{\tilde{\nu}_{\tau_L}}$	853	1103	1104
$m_{\tilde{e}_L}$, $m_{\tilde{\mu}_L}$	897	1206	1207
$m_{\tilde{\tau}_2}$	859	1108	1112
$m_{\tilde{\chi}_1^0}$	497	693	946
$m_{\tilde{\mu}_R}$, $m_{\tilde{e}_R}$	587	757	1006
$m_{\tilde{\tau}_1}$	421	599	831
$m_{\tilde{\nu}}$	36.5	44.5	44.5
m_{h^0}	124	125	125
m_{A^0}	1696	1800	1800
$\tan\beta$	11.18	20.00	30.00
μ	1590	1200	1200
$\Omega_{\tilde{\nu}}h^2$	0.1127	0.1127	0.1112
A_t	-2375	-2600	-2600
A_ν	-2619	-2619	-2619
$|U_{L1}^{\tilde{\tau}_1}|$	6.49×10^{-2}	5.58×10^{-1}	1.33×10^{-1}

Table 4.3: Benchmark points for studying the $m_{\tilde{\chi}_1^0} < m_{\tilde{\mu}_R, \tilde{e}_R}$ scenario.

Cut Set	N_s	
	Case I	Case II
Cut Set A	BP1: 73	BP4: 45
	BP2: 26	BP5: 11
	BP3: 10	BP6: 2
Cut Set B	BP1: 79	BP4: 48
	BP2: 31	BP5: 12
	BP3: 12	BP6: 2

Table 4.4: Number of signal events, surviving all the cuts, at an integrated luminosity of $\mathcal{L} = 3000$ fb^{-1} for Case I ($m_{\tilde{\chi}_1^0} > m_{\tilde{\mu}_R, \tilde{e}_R}$) and Case II ($m_{\tilde{\chi}_1^0} < m_{\tilde{\mu}_R, \tilde{e}_R}$) for the single τ-tagged jet signature.

momentum. One can clearly observe that cut set A lowers the number of events compared to cut set B, thereby improving the slepton mass reconstruction, by removing high $\not{E}_T$ events which are mainly a manifestation of detector effects and longer distribution tails owing to the off-shell slepton regime. Finally, if one defines the end point of the M_{T2} distribution to be the last bin that contains at least one signal event, then the slepton masses can be reconstructed with an accuracy of 5-10%, at an integrated luminosity of 3000 fb^{-1}. Using this definition, the reconstructed (actual) slepton mass for BP1 and BP4 are 505 (491) GeV and 570 (587) GeV respectively. The reconstructed (actual) masses are shown with the vertical dashed lines (arrows) in Fig. 4.3.

Until now, we have focused on the number of signal events surviving all cuts. However, with the cut applied on the speed, β, of the two hardest muons as implemented in Ref. [67], we end up with hardly any background events. Indeed the total SM background is reduced from ~ 21 events for $\mathcal{L} = 3000$ fb^{-1} in the absence of the β-cut, to $\lesssim 1$ upon demanding $\beta \leqslant 0.98$ for the two hardest muons in each event. Note that to be realistic in our background modelling, we also take into account the possibility of QCD jets faking leptons. A flat mistagging rate of 0.5% (0.1%) is considered for $j \to e$ (μ).
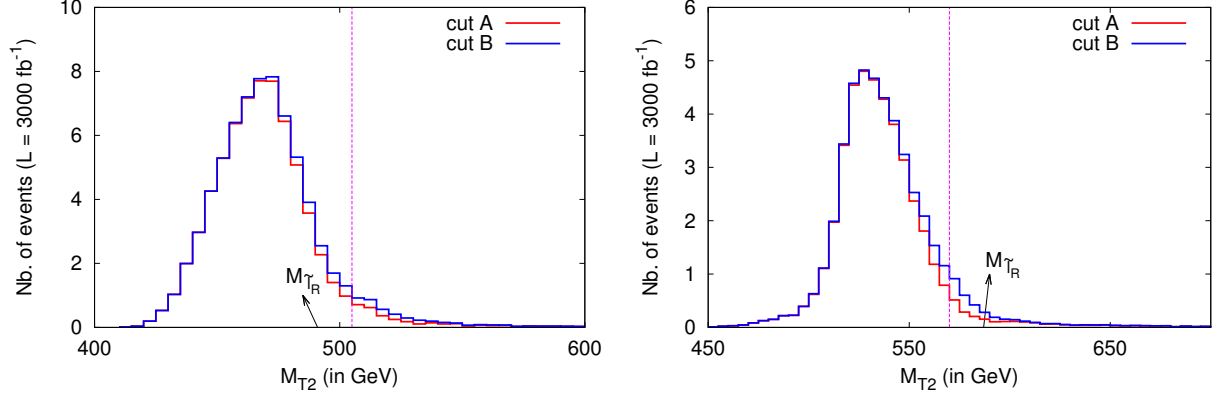
Figure 4.3: M_{T2}-distributions for BP1 (left) and BP4 (right) corresponding to $m_{\tilde{\chi}_1^0} > m_{\tilde{\mu}_R, \tilde{e}_R}$ and $m_{\tilde{\chi}_1^0} < m_{\tilde{\mu}_R, \tilde{e}_R}$ respectively. The vertical dashed lines show the reconstructed slepton masses following our prescription while the arrow symbolises the actual slepton mass. The distributions are constructed after all cuts.

4.4.2 Additional channel : two τ-tagged jets

In this last segment, we focus on the signature comprising of 2 $\tilde{\tau}_1/\mu$ tracks, 2 OSSF leptons, 2 τ-tagged jets along with $\not{E}_T$. This final state, however, suffers from a severe dearth of signals events owing to the double τ-tag. We summarise the number of surviving signal events for the two mass hierarchies, in Tab. 4.5. Here, we use the collinear approximation in order to reconstruct the τs. This method is shown to work quite accurately for $p_T^{\tau_j} > 40$ GeV. Fig. 4.4 shows the final reconstruction of the slepton masses for BP1 and BP4. The reconstruction peaks agree with the actual masses within the percent level.

The number of background events for the double τ-tagged scenario even before the implementation of the β cut is more than an order of magnitude smaller than its single τ-tagged counterpart. With $\mathcal{L} = 3000$ fb^{-1}, the number of background events is $\lesssim 1$. This is because, upon demanding two τ tags from the fake backgrounds ($t\bar{t}Z, ZZ$ and ZW^+W^-) with the small fake rates mentioned above, there are hardly any events which survive the event selection. Moreover, the real backgrounds, *viz.*, ZZZ, Zh have extremely small cross-sections Furthermore, the p_T requirement on the τ-tagged jets reduces the backgrounds further. For consistency, we nevertheless apply the same cut on β as in the previous case, moreover this cut hardly affects the signal. Even though the double-τ-tagged events are "background free", the number of signal events is also very low. For most of the benchmark points the number
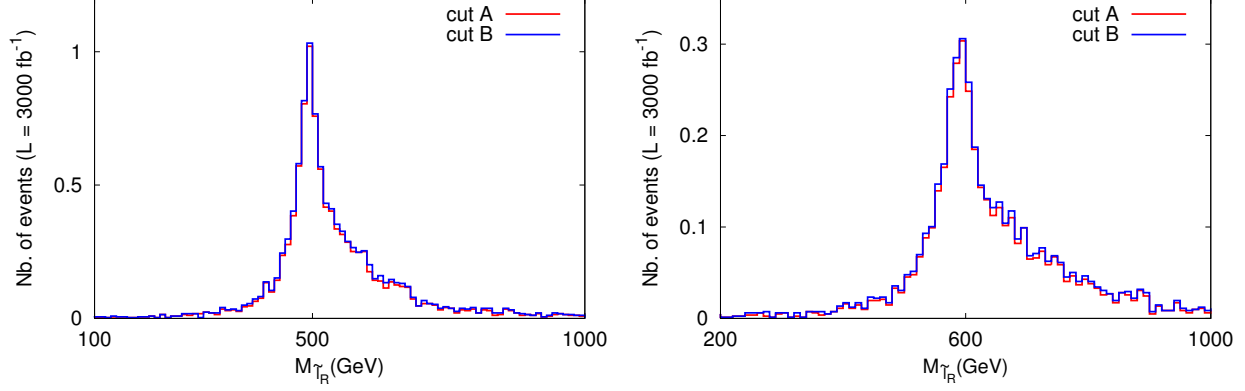
Figure 4.4: Figure shows $m_{\tilde{\mu}_R/\tilde{e}_R}$ distributions for BP1 ($m_{\tilde{\chi}_1^0} > m_{\tilde{\mu}_R,\tilde{e}_R}$) on the left panel and BP4 ($m_{\tilde{\chi}_1^0} < m_{\tilde{\mu}_R,\tilde{e}_R}$) on the right panel. The distributions are constructed after all cuts.

Cut Set	N_s	
	Case I	Case II
Cut Set A	BP1: 12	BP4: 11
	BP2: 7	BP5: 3
	BP3: 2	BP6: 1
Cut Set B	BP1: 13	BP4: 12
	BP2: 9	BP5: 3
	BP3: 3	BP6: 1

Table 4.5: Number of signal events, surviving all the cuts, at an integrated luminosity of $\mathcal{L} = 3000$ fb^{-1} for Case I ($m_{\tilde{\chi}_1^0} > m_{\tilde{\mu}_R,\tilde{e}_R}$) and Case II ($m_{\tilde{\chi}_1^0} < m_{\tilde{\mu}_R,\tilde{e}_R}$) for the 2 $\tilde{\tau}_1/\mu$ + 2 τ-tagged jet + 2 OSSF leptons + $\not{E}_T$ final state.

of signal events in the bin corresponding to actual slepton mass is less than one. Hence, although the two-τ-tagged channel can in principle lead to a more accurate reconstruction of the slepton masses than the single τ-tagged mode, this channel can only be useful for a future collider with much higher luminosities or higher energies than the HL-LHC.

To conclude this section, it is of utmost importance to reiterate that the lightest neu-

Benchmark points	N_s	
	1 $\tilde{\tau}_1$	2 $\tilde{\tau}_1$
BP1	26	6
BP2	7	2
BP3	3	1
BP4	15	4
BP5	4	1
BP6	1	1

Table 4.6: Number of events with 1 $\tilde{\tau}_1$ and 2 $\tilde{\tau}_1$, at an integrated luminosity of $\mathcal{L} = 3000$ fb^{-1} for Case I ($m_{\tilde{\chi}_1^0} > m_{\tilde{\mu}_R, \tilde{e}_R}$) and Case II ($m_{\tilde{\chi}_1^0} < m_{\tilde{\mu}_R, \tilde{e}_R}$) detectable at MoEDAL.

tralino, χ_1^0, can be reconstructed using the procedure outlined in Ref. [121] and the stau mass can be reconstructed using the method described in Ref. 4.3.1. Hence, with the information on the reconstructed $\tilde{\tau}_1$-mass and the χ_1^0-mass and the knowledge of reconstructing the right-handed slepton following the aforementioned procedures, one can straightforwardly disentangle the two mass-hierarchies, *viz.*, $m_{\chi_1^0} < m_{\tilde{\mu}_R, \tilde{e}_R}$ and $m_{\tilde{\mu}_R, \tilde{e}_R} < m_{\chi_1^0}$.

4.4.3 Detection prospects at MoEDAL

Long-lived particles can also be looked for at the new and largely passive detector MoEDAL [198, 199]. It is composed of nuclear track detectors and is located at the Point 8 on the LHC ring. MoEDAL is designed to detect monopoles and massive stable charged particles. Our model has a unique signature in terms of long-lived $\tilde{\tau}_1$s which can be detected there, if their $\beta \lesssim 0.5$. Although most of the $\tilde{\tau}_1$s in the channels considered do not satisfy this condition, see Fig. 4.2, at least one signal event is expected for all our benchmark points. We show in Tab. 4.6, the number of events with single and double $\tilde{\tau}_1$s expected at MoEDAL at an integrated luminosity of 3000 fb^{-1}. For illustration, we have reported only those events with $p_T^{\tilde{\tau}_1} > 10$ GeV and $\beta^{\tilde{\tau}_1} \lesssim 0.5$. However, we have not taken into account, the angular orientations of these long-lived particles and this may play a role in determining the final numbers. Although this signature will not provide additional information on the underlying SUSY spectrum, it will contribute to the validation of the long-lived stau scenario.

4.5 Conclusion

A pMSSM scenario augmented with three families of right-chiral neutrino superfields has been assumed in this chapter. With only Dirac masses for neutrinos, and corresponding SUSY breaking mass terms, we have considered several benchmark points, with a right sneutrino as the LSP and the dominantly right-chiral $\tilde{\tau}_1$ serving as the NLSP. Owing to the smallness of the neutrino Yukawa coupling (required by the neutrino oscillation data), the $\tilde{\tau}_1$s are fairly long-lived in the scale of colliders [9]. Large p_T and small β of these long-lived particles make it easy to discriminate them from the SM backgrounds. We assumed two different hierarchical structures for the masses of the weak-sector particles ($\tilde{\chi}_1^0$ and sleptons) here and have suggested a procedure for differentiating the two by reconstructing the slepton masses. We considered two possible signatures in each case, which differ only in the number of τ-tagged jets identified in the final states. In case of the single τ-tagged jet signal, the asymmetric M_{T2} variable is found out to be a good kinematic variable while in the other case, the collinear approximation has been used to reconstruct the τs and thereby the sleptons. The latter method, even though cleaner, suffers from a dearth in signal statistics and can only be used for future runs with higher luminosities and/or centre of mass energies.

---

[9]Such long-lived nature can also be realized in presence MeV-scale Majorana masses of the right-handed neutrinos, as shown in [200].

Chapter 5

Gamma-ray signals from multicomponent scalar dark matter decays

5.1 Introduction

In chapters 3 and 4 we have studied the possibility of pinning down a dark matter particle, very weakly coupled to the visible sector, via the production of heavier charged dark sector particles inside the periphery of collider detectors. Another possible strategy to detect dark matter particles is to look for the products of dark matter annihilation or decay, occurring in galaxies, galaxy clusters or extragalactic continuum, either in the form of photons, antimatter particles or neutrinos. Though the annihilation rates are extremely small for dark matter particles with such superweak interaction strengths, the dark sector might contain more than one candidates contributing to the relic density. The heavier of the two then decays to the lighter with a lifetime much longer than the age of the universe, giving rise to visible SM particles, a possibility already discussed in chapter 2.

However, the search for these SM particles is challenging, due to the existence of large (and not always sufficiently well understood) astrophysical backgrounds. On the other hand, in a given dark matter framework the intensity and energy spectrum of the products of annihilation or decay can be calculated, thus permitting in principle a dedicated search for this exotic component in the data. In many cases, the exotic flux component is expected to have a smooth energy spectrum, which is not easily distinguishable from the background.

However, some dark matter frameworks predict fluxes at Earth with energy spectra which are distinctively different from the ones predicted by state-of-the-art background models. For these frameworks, current instruments can be very sensitive to annihilation or decay signals. More importantly, the identification of such distinctive signal would hence constitute an evidence for the particle nature of the dark matter.

Generically, these distinctive features appear in dark matter annihilations or decays where the final state contains stable particles with energies at, or close to, the kinematic cut-off. While there exists a plenty of scenarios where DM pair annihilations give rise to a gamma-ray line [201,202] or a distinctive gamma-ray spectrum [203–206], frameworks with DM decay can also be envisioned [207,208]. Finally, the fairly good energy resolution for the cascade events at IceCube opens up the possibility of observing features in the neutrino energy spectrum from the two body decays $\nu\mathcal{N}$ (with $\mathcal{N} = \gamma, Z, h, \nu$ a neutral Standard Model particle) [209].

As mentioned earlier, there could be more than one particle contributing to the dark matter density, where additional dark matter signals may be obtained from the decay of a heavier dark matter component into a lighter, if allowed by the symmetries of the model [55]. Of special interest is the case where the mass difference is small, possibly due to the mild breaking of a dark sector symmetry, such that the phase space available in the decay is also small, thus leading to longer lifetimes (in analogy to the slow neutron decay into a proton, electron and antineutrino, which is a consequence of the mild breaking of the isospin symmetry). For sufficiently small mass differences, only decays into photon and neutrinos would be kinematically accessible, thus naturally leading to distinctive signals in the cosmic fluxes of these particle species.

For multicomponent fermionic dark matter the decay $\psi_2 \to \psi_1\gamma$ would produce a line in the photon spectrum at an energy $E_\gamma = M_2/2(1 - M_1^2/M_2^2)$, with M_1 and M_2 the masses of the dark matter components ψ_1 and ψ_2, respectively. The signals in this case, are analogous to those from a single-component fermionic dark matter scenario with decay $\psi \to \gamma\nu$, generates a photon with energy $E_\gamma = m_\psi/2$, and has been thoroughly studied in the literature [210]. This class of models generically predicts also the three-body decays $\psi_2 \to \psi_1\nu\bar{\nu}$ and, if kinematically allowed, $\psi_2 \to \psi_1 e^+e^-$ or into other charged fermions, which contribute respectively to the neutrino flux or to the electron/positron flux [211].

The case of the multicomponent scalar dark matter has received less attention (see, however, [212]). The two body decay $\phi_2 \to \phi_1\gamma$ is forbidden by the conservation of total angular momentum. On the other hand, the process $\phi_2 \to \phi_1\gamma\gamma$ is allowed. In this chapter we will study this process in detail, focusing on the case where the mass difference between

the two dark matter components is small. In this regime, the photon spectrum produced in the decay has a distinctive shape that allows a sensitive search for this signal in the gamma-ray data. Furthermore, the branching ratio of this process can be sizable (or even dominant). Hence, the search for the photon signals would constitute the most powerful probe of this scenario.

This chapter is organized as follows: In section 5.2 we consider an effective theory approach to describe the decays $\phi_2 \to \phi_1 \gamma\gamma$, $\phi_2 \to \phi_1 f\bar{f}$, and we provide a simple model where the effective interactions are generated at the one loop level due to a Yukawa coupling of the dark matter components with two exotic electrically charged heavy fermions. In section 5.3 we consider a variant of this model, where the two dark matter components interact with one light Standard Model fermion and one heavy exotic fermion, in which case the effective theory description of the decay $\phi_2 \to \phi_1 \gamma\gamma$ may not be valid. In section 5.4 we consider a concrete realization of the latter scenario in the context of the $\tilde{\nu}$MSSM. Finally, in section 5.5 we summarize and conclude.

5.2 Effective theory approach to multicomponent scalar dark matter decay

We consider a scenario where the Standard Model is extended with two scalar gauge singlets, ϕ_1 and ϕ_2, with masses M_1 and M_2 respectively. We also introduce a Z_2 symmetry, under which ϕ_1 and ϕ_2 are both odd, while all Standard Model particles are even. Therefore, interaction terms of the form $\phi_i |H|^2$ are forbidden. We assume that ϕ_1 is the lightest particle of the Z_2-odd sector. Then, ϕ_1 is cosmologically stable and constitutes a dark matter candidate. The heavier scalar singlet ϕ_2 decays into ϕ_1, but it is assumed to be long-lived in cosmological time-scales. In this scenario, therefore, the dark matter contains two components with abundances $\Omega_{\phi_1} h^2$ and $\Omega_{\phi_2} h^2$. The relic density of both dark matter components can be determined *e.g.* by thermal freeze-out [213, 214] or by thermal freeze-in [215] depending on the model parameters. In what follows, we will not address dark matter production, but simply assume that the total dark matter abundance is $(\Omega_{\phi_1} + \Omega_{\phi_2}) h^2 \simeq 0.12$, as determined by the Planck satellite [10].

The signals of the mono-component singlet scalar dark matter scenario have been thoroughly discussed in the literature, and the extension to the multi-component variant of the model is straightforward. In this chapter, therefore, we will focus on the aspects of the

model that are specific to the multicomponent character of our framework. Concretely, we will focus on the signals arising from the decay of the heavier Z_2-odd dark matter component into the lighter. The decay can be induced by the Higgs portal term

$$-\mathcal{L}_{\text{dim}-4} = f_3 \phi_2 \phi_1 |H|^2 , \tag{5.2.1}$$

or by dimension six operators of the form

$$-\mathcal{L}_{\text{dim}-6} = \frac{g_4}{\Lambda_4^2} \phi_2 \phi_1 \mathcal{S}_{\text{dim}-4} + \frac{g_3}{\Lambda_3^2} \phi_2 \partial_\mu \phi_1 \mathcal{V}^\mu_{\text{dim}-3} + \frac{g_3'}{\Lambda_3^2} \phi_1 \partial_\mu \phi_2 \mathcal{V}^\mu_{\text{dim}-3} + \frac{g_2}{\Lambda_2^2} \partial_\mu \phi_1 \partial_\nu \phi_2 \mathcal{T}^{\mu\nu}_{\text{dim}-2} , \tag{5.2.2}$$

where $\mathcal{S}_{\text{dim}-4}$, $\mathcal{V}^\mu_{\text{dim}-3}$ and $\mathcal{T}^{\mu\nu}_{\text{dim}-2}$ are, respectively, any gauge invariant dimension-four scalar, dimension-three vector or dimension-two tensor operator involving Standard Model particles only. Besides, Λ_i denotes the typical mass scale of the particles generating the corresponding effective interaction, and g_i are dimensionless parameters; the validity of our effective theory requires $\Lambda_i \gg M_1, M_2$.

These effective interactions could be generated, for instance, by extending the model with heavy vector-like fermionic fields $\psi_1(Z_2\text{-even})$ and $\psi_2(Z_2\text{-odd})$ with masses m_1 and m_2, respectively, singlets under $SU(3)_c \times SU(2)_L$ and with hypercharge -1, which couple to the scalar field ϕ_i via a Yukawa interaction $Y_i \phi_i \overline{\psi}_1 \psi_2$. Integrating out the heavy fermions, one obtains the following dimension-six operators involving the electromagnetic field strength tensor, through the diagrams shown in Fig. 5.1:

$$-\mathcal{L}_{\text{int}} \supset \frac{f_1}{\Lambda^2} \left(\partial_\mu \phi_2 \partial_\nu \phi_1 - \partial_\nu \phi_2 \partial_\mu \phi_1 \right) F^{\mu\nu} + \frac{f_2}{\Lambda^2} \phi_2 \phi_1 F^{\mu\nu} F_{\mu\nu} , \tag{5.2.3}$$

with

$$\frac{f_1}{\Lambda^2} \simeq \frac{\alpha_{\text{EM}}^{1/2}}{12\pi^{3/2} m_1 m_2} g\left(\frac{m_1}{m_2}\right) \text{Im}(Y_1 Y_2^*),$$

$$\frac{f_2}{\Lambda^2} \simeq \frac{\alpha_{\text{EM}}}{12\pi \, m_1 \, m_2} \text{Re}(Y_1 Y_2^*). \tag{5.2.4}$$

Here,

$$g(x) = \frac{3x \left(1 - 4x + x^2\right)}{\left(1 - x^2\right) \left(1 - x\right)^2} + \frac{4x \left(1 - 3x + x^2 - 3x^3 + x^4\right) \log x}{\left(1 - x^2\right)^2 \left(1 - x\right)^2} \tag{5.2.5}$$

is a function that satisfies $g(x) = -g(x^{-1})$ and which vanishes at $x = 1$ (*i.e.*, when $m_1 = m_2$) and when $x \gg 1$ or $x \ll 1$ (*i.e.*, when there is a large hierarchy between m_1 and m_2); the vanishing of the Wilson coefficient $f_1 = 0$ when $m_1 = m_2$ is due to Furry's theorem, as in
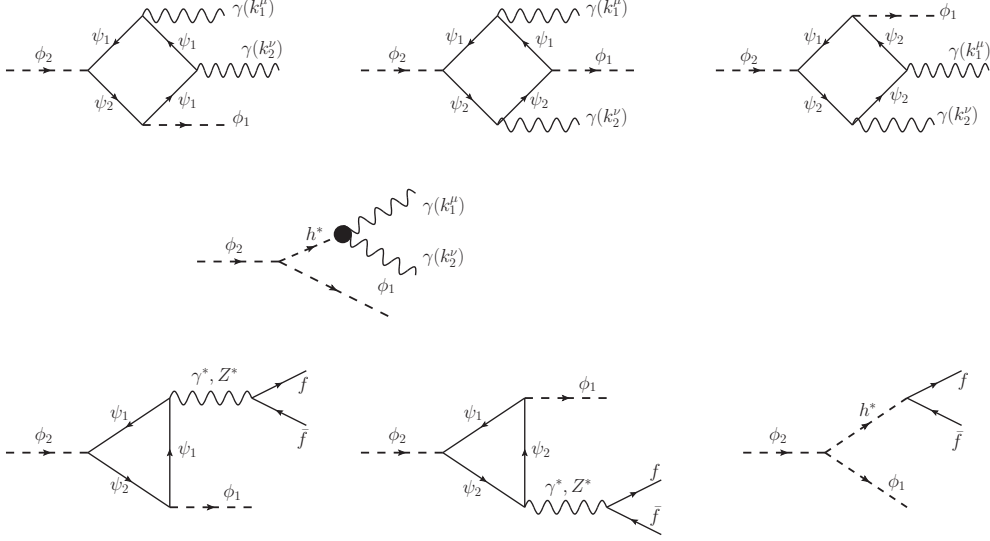
Figure 5.1: One-loop Feynman diagrams contributing to the processes $\phi_2 \rightarrow \phi_1 \gamma \gamma$ and $\phi_2 \rightarrow \phi_1 f \bar{f}$. Diagrams where the photon lines are interchanged (not shown in the Figure) also contribute to the amplitudes.

this limit the vertex factors remain invariant under the reversal of the fermion directions in the loop. Note also that f_1 is non-zero only when the relative phase between Y_1 and Y_2 is different from 0 or π. Analogous interactions involving the Z-boson arise upon replacing $A^\mu \rightarrow - \tan \theta_W Z^\mu$, with θ_W being the Weinberg's angle.

The possible two body decay final states include a Standard Model neutral boson, either a photon, a Z boson or a Higgs boson. It can be checked that the decay rate for $\phi_2 \rightarrow \phi_1 \gamma$ via the operator proportional to f_1 is zero for an on-shell photon, in concordance with the conservation of angular momentum. On the other hand, decays involving one Z-boson or one Higgs boson are allowed. The signatures of these decays are identical to those produced by the well studied decays $\phi \rightarrow ZZ, hh$, with the appropriate shift in the energy of the Z or the Higgs boson.

In this chapter we concentrate in a scenario where the two-body decays $\phi_2 \rightarrow \phi_1 X$, with X a massive boson, are kinematically forbidden. One can define the parameter $\Delta \equiv 1 - M_1^2/M_2^2$, which measures the mass degeneracy between the two dark matter components: $\Delta \simeq 1$ corresponds to a very hierarchical spectrum and $\Delta \simeq 0$ to a very degenerate spectrum. The condition $M_2 < M_1 + M_X$ that forbids the decay $\phi_2 \rightarrow \phi_1 X$, with M_X the mass of the boson X, then translates into $M_2 \leq M_X/(1 - \sqrt{1 - \Delta})$. This condition is satisfied, in particular for the hierarchical spectrum when ϕ_2 is lighter than X, and in the degenerate limit when

$M_2 \lesssim 2M_X/\Delta$ [1]. The possible three body decays are then $\phi_2 \to \phi_1 f\bar{f}$, with f being a Standard Model fermion, and $\phi_2 \to \phi_1 \gamma\gamma$. While three body decays with two fermions in the final state have been discussed in the literature in other scenarios, the three body decay with two photons in the final state has received less attention (see, however, [212]).

The decay $\phi_2 \to \phi_1 f\bar{f}$, if kinematically allowed, is induced by the mediation of an off-shell photon (via the dimension-six operator proportional to f_1 in Eq. (5.2.3)), an off-shell Z-boson (via the dimension-six operator proportional to f_1 in Eq. (5.2.3), replacing $A^\mu \to -\tan\theta_{\mathrm{W}} Z^\mu$), and an off-shell Higgs boson (via the dimension-four operator proportional to f_3 in Eq. (5.2.1)). The differential decay rate reads

$$
\begin{aligned}
\frac{d\Gamma_{\phi_1 f\bar{f}}}{dx_f} =\ & \frac{f_1^2 N_c \alpha_{\mathrm{EM}}}{192\pi^3 \Lambda^4} M_2^5 \Delta^5 \frac{x_f^2 (1-x_f)^2}{(1-x_f \Delta)} \left[12 q_f^2 + 8 q_f c_v^{(f)} \frac{M_2^2 \Delta^2}{\cos^2\theta_{\mathrm{W}} m_Z^2} \frac{x_f(1-x_f)}{(1-x_f \Delta)} \right. \\
& \left. + (c_v^{(f)2} + c_a^{(f)2}) \frac{M_2^4 \Delta^4}{\cos^4\theta_{\mathrm{W}} m_Z^4} \frac{x_f^2 (1-x_f)^2}{(1-x_f \Delta)^2} \right] + \frac{f_3^2 N_c m_f^2}{128\pi^3 m_h^4} M_2^3 \Delta^5 \frac{x_f^2 (1-x_f)^2}{(1-\Delta x_f)^2}, \quad (5.2.6)
\end{aligned}
$$

where we have defined $x_f \equiv \dfrac{2E_f}{M_2 \Delta}$, which is kinematically restricted to be in the range $0 \le x_f \le 1$. Here, m_f and q_f are the fermion mass and electric charge, N_c is the number of colors, and $c_v^{(f)}$ and $c_a^{(f)}$ are the vector and axial-vector couplings to the Z boson. In these expressions it has been assumed that $M_2 - M_1 \gg 2m_f$, such that the final state fermions are relativistic. We note that the amplitudes of the processes mediated by gauge bosons interfere with each other, but not with the amplitude of the process mediated by the Higgs, as the fermions in the final state have the same chirality in the former case, while opposite chirality in the latter. We also note that the conservation of angular momentum requires the two (relativistic) final state fermions to be emitted in the same direction when the fermions have the same chirality, and in opposite directions when they have opposite chirality. The conservation of linear momentum requires the scalar ϕ_1 to be emitted collinearly with one of the fermions when they have opposite chirality (and, when the two fermions have the same chirality, in the opposite direction to these).

The total decay rate for the decay $\phi_2 \to \phi_1 f\bar{f}$ is

$$
\begin{aligned}
\Gamma_{\phi_1 f\bar{f}} =\ & \frac{f_1^2 N_c \alpha_{\mathrm{EM}}}{120960\pi^3 \Lambda^4} M_2^5 \Delta^5 \left[252 q_f^2\, {}_2F_1(1,3,6;\Delta) + 36 q_f c_v^{(f)} \frac{M_2^2 \Delta^2}{\cos^2\theta_{\mathrm{W}} m_Z^2}\, {}_2F_1(2,4,8;\Delta) \right. \\
& \left. + (c_v^{(f)2} + c_a^{(f)2}) \frac{M_2^4 \Delta^4}{\cos^4\theta_{\mathrm{W}} m_Z^4}\, {}_2F_1(3,5,10;\Delta) \right] + \frac{f_3^2 N_c m_f^2}{3840\pi^3 m_h^4} M_2^3 \Delta^5\, {}_2F_1(2,3,6;\Delta),
\end{aligned}
$$

$$(5.2.7)$$

---

[1] For small mass splittings, the effective operators of Eq. (5.2.2) in general should contain not quarks and gluons as degrees of freedom but pions, as dictated by chiral perturbation theory. In this regime, the two body decay $\phi_2 \to \phi_1 \pi^0$ or similar decays involving mesons may occur.

where we have used that

$$\int_0^1 dx \, x^{b-1}(1-x)^{c-b-1}(1-\Delta x)^{-a} = {}_2F_1(a,b,c;\Delta)\mathrm{B}(b,c-b) \qquad (5.2.8)$$

for $c > b > 0$. Here, $\mathrm{B}(a,b)$ is the Euler's beta function and ${}_2F_1(a,b,c;\Delta)$ is the Gauss's hypergeometric function, which is monotonically increasing with Δ and takes limiting values

$$
\begin{aligned}
{}_2F_1(a,b,c,0) &= 1 \ , \\
{}_2F_1(a,b,c,1) &= \frac{\Gamma(c)\Gamma(c-a-b)}{\Gamma(c-a)\Gamma(c-b)} \ ,
\end{aligned}
\qquad (5.2.9)
$$

for $c > a + b$.

One can check that

$$\frac{M_2^2 \Delta^2}{m_Z^2} \le \left(1 + \frac{M_1}{M_2}\right)^2 < 4 \ , \qquad (5.2.10)$$

where the maximum value occurs for $M_2 = M_1 + m_Z$, namely when the Z-boson can be produced on-shell, and when $M_2/m_Z \to \infty$. Therefore, in most of the parameter space the contribution to the rate from the Z-boson mediated decay can be neglected against the contribution from the photon mediated decay. On the other hand, the contribution from the Higgs boson should not be neglected, despite the suppression by m_f/m_h, as it depends on a different coupling. A special case is the decay $\phi_2 \to \phi_1 \nu \bar{\nu}$, since both the Higgs and photon exchange contributions to the rate are very suppressed compared to the Z-boson exchange contribution.

The process $\phi_2 \to \phi_1 \gamma\gamma$, on the other hand, receives contributions from the dimension-six operator proportional to f_2 in Eq. (5.2.3), and from the mediation of an off-shell Higgs boson, via the dimension-four operator proportional to f_3 in Eq. (5.2.1) combined with the effective Higgs interaction $c_{\gamma\gamma}\frac{h}{v}F^{\mu\nu}F_{\mu\nu}$. The differential rate reads:

$$\frac{d\Gamma_{\phi_1\gamma\gamma}}{dx_\gamma} = \frac{1}{192\pi^3}\left(\frac{f_2}{\Lambda^2} + \frac{f_3 c_{\gamma\gamma}}{m_h^2}\right)^2 M_2^5 \, \Delta^7 \, \frac{x_\gamma^3 (1-x_\gamma)^3}{(1-x_\gamma\Delta)^3} \ , \qquad (5.2.11)$$

where $x_\gamma \equiv \dfrac{2E_\gamma}{M_2\Delta}$ and $c_{\gamma\gamma} \simeq -2.03 \times 10^{-3}$ in the Standard Model. Due to the conservation of angular momentum, the two photons must be emitted back to back if they have the same polarization, and collinearly if they have opposite polarization; the conservation of linear momentum requires ϕ_1 to be emitted along with one of the photons in the former case,

and in the direction opposite to the photons in the latter [2]. The partial rate of this decay channels is:

$$\Gamma_{\phi_1\gamma\gamma} = \frac{1}{26880\pi^3}\left(\frac{f_2}{\Lambda^2} + \frac{f_3 c_{\gamma\gamma}}{m_h^2}\right)^2 M_2^5\,\Delta^7\,{}_2F_1(3,4,8;\Delta)\,, \tag{5.2.12}$$

where we have used Eq. (5.2.8). Here, ${}_2F_1(3,4,8;\Delta)$ varies between 1 and 35 for Δ between 0 and 1.

Approximate expressions for the partial decay rates are:

$$\begin{aligned}
\Gamma_{\phi_1 e^+ e^-} &\simeq \left(10^{26}\,\text{s}\right)^{-1}\left[\left(\frac{f_1/\Lambda^2}{1.1\times10^{-22}\,\text{GeV}^2}\right)^2\left(\frac{M_2}{1\,\text{GeV}}\right)^5\Delta^5\,{}_2F_1(1,3,6;\Delta)\right.\\
&\quad\left.+\left(\frac{f_3}{8.8\times10^{-16}}\right)^2\left(\frac{M_2}{1\,\text{GeV}}\right)^3\Delta^5\,{}_2F_1(2,3,6;\Delta)\right]\,,\\
\Gamma_{\phi_1\nu_i\bar\nu_i} &\simeq \left(10^{26}\,\text{s}\right)^{-1}\left(\frac{f_1/\Lambda^2}{1.7\times10^{-17}\,\text{GeV}^{-2}}\right)^2\left(\frac{M_2}{1\,\text{GeV}}\right)^9\Delta^9\,{}_2F_1(3,5,10;\Delta)\,,\\
\Gamma_{\phi_1\gamma\gamma} &\simeq \left(10^{26}\,\text{s}\right)^{-1}\left[\frac{f_2/\Lambda^2}{7.4\times10^{-23}\,\text{GeV}^{-2}} - \frac{f_3}{5.7\times10^{-16}}\right]^2\left(\frac{M_2}{1\,\text{GeV}}\right)^5\Delta^7\,{}_2F_1(3,4,8;\Delta).
\end{aligned} \tag{5.2.13}$$

Clearly, ϕ_2 can be cosmologically long-lived for sufficiently weak interaction strengths f_1, f_2, f_3, and/or for a small mass for the mother dark matter particle and/or for a small mass difference with the daughter dark matter particle. Fig. 5.2 shows contour lines of the inverse decaywidth in the final states $\phi_1\gamma\gamma$ (top panel), $\phi_1\nu\bar\nu$ (bottom panel left) and $\phi_1 e^- e^+$ (bottom panel right), for the representative cases $\Delta = 1$ and $\Delta = 0.001$, which respectively correspond to a very hierarchical spectrum and to a very degenerate spectrum of dark matter components.

The rates for the different processes depend on different combinations of the couplings f_1, f_2 and f_3. However, if the decays are dominated by the Higgs exchange one finds

$$\frac{\Gamma_{\phi_1\gamma\gamma}}{\Gamma_{\phi_1 e^- e^+}} \simeq \frac{c_{\gamma\gamma}^2}{7}\frac{M_2^2\Delta^2}{m_f^2}\frac{{}_2F_1(3,4,8;\Delta)}{{}_2F_1(2,3,6;\Delta)}\,,$$

---

[2] It is interesting to remark that, even if the photons are emitted in the same direction and with the same speed, the propagation history of the two photons on their way to the Earth might be different. Therefore they will not arrive to the detector in coincidence. We will make this assumption when we analyze the observable signals of this framework. On the other hand, the emission of two photons in exactly the same direction and with the same speed is a very peculiar feature of the decay $\phi_2 \to \phi_1\gamma\gamma$, not exclusively of the framework where ϕ_1 and ϕ_2 are cosmologically long-lived, and could have implications in other contexts.
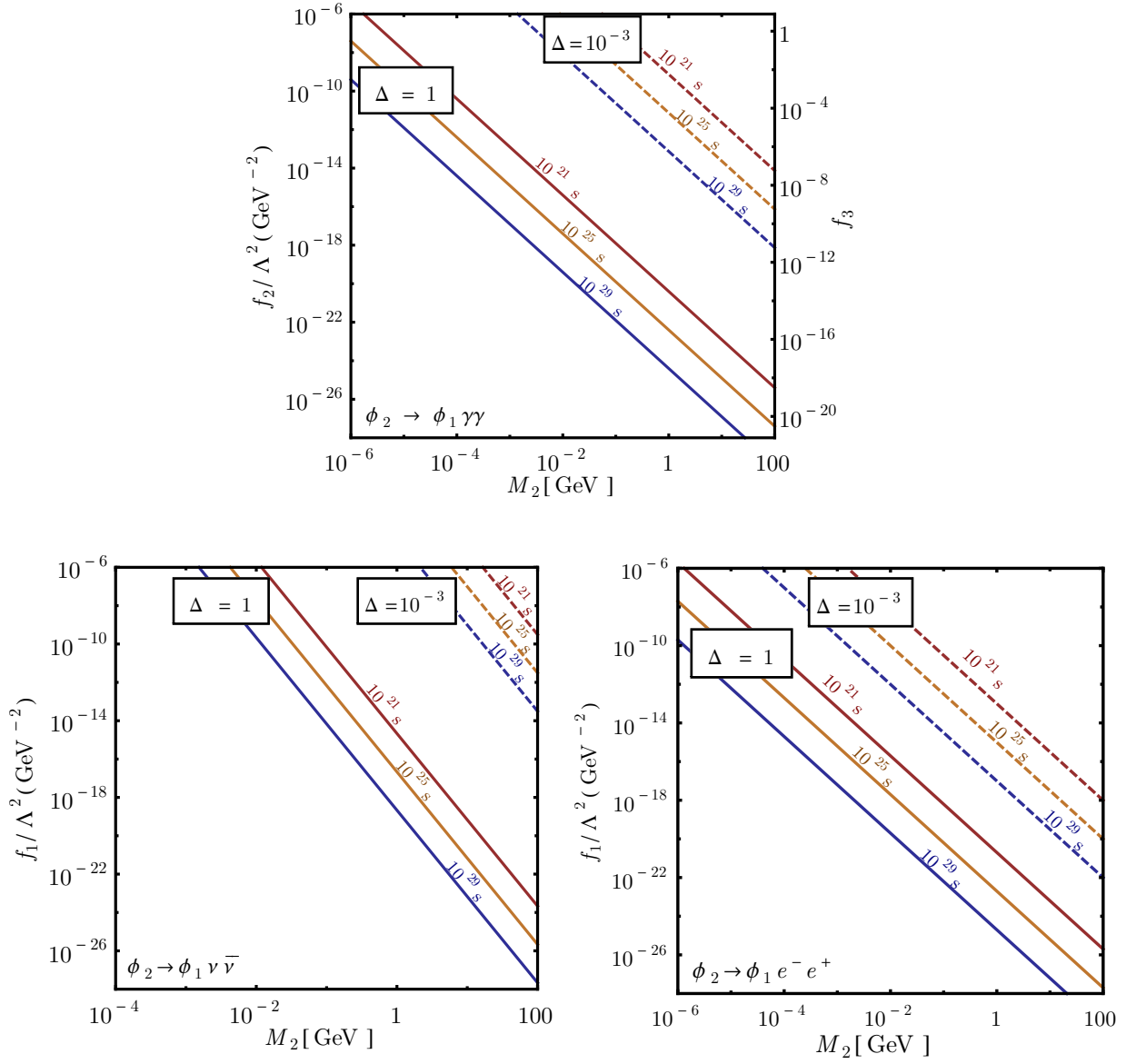
Figure 5.2: Inverse width contours for the decay processes $\phi_2 \to \phi_1 \gamma\gamma$ (top panel), $\phi_2 \to \phi_1 \nu\bar{\nu}$ (bottom left panel) and $\phi_2 \to \phi_1 e^- e^+$ (bottom right panel) as a function of the mass of the decaying dark matter component M_2, for exemplary hierarchical ($\Delta = 1$) and degenerate ($\Delta = 10^{-3}$) spectra, for the effective theory described in Section 5.2 characterized by the couplings f_1/Λ^2, f_2/Λ^2 and f_3.

$$\Gamma_{\phi_1 \nu_i \bar{\nu}_i} \simeq 0 \ . \tag{5.2.14}$$

Besides, for the toy model where the effective interactions f_1 and f_2 are generated via
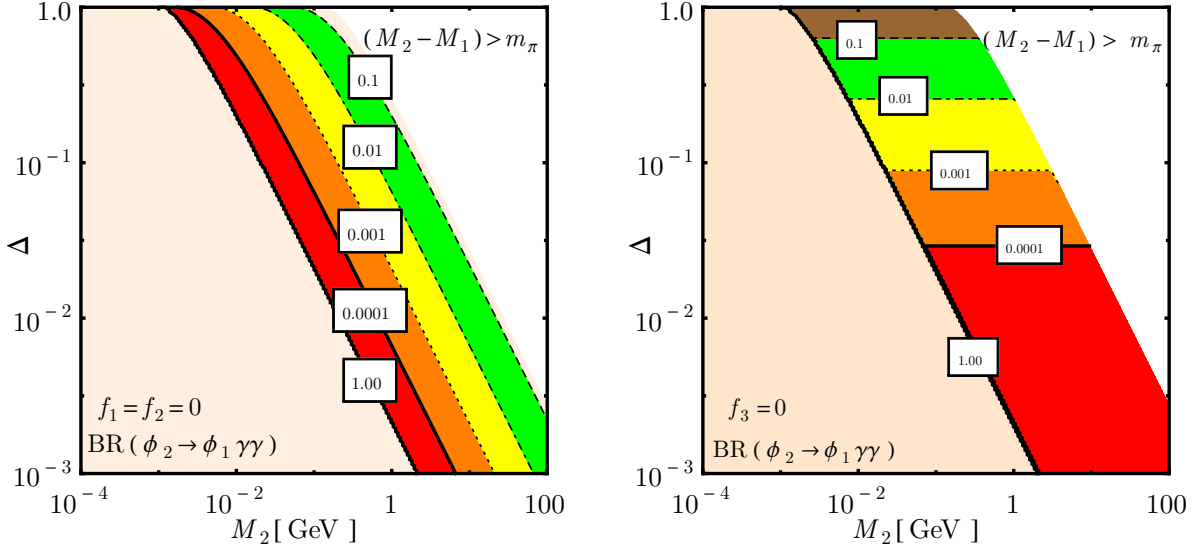
Figure 5.3: Branching ratios of the process $\phi_2 \to \phi_1\gamma\gamma$ as a function of the decaying dark matter mass M_2 and the degeneracy parameter Δ for an effective theory with $f_1 = f_2 = 0$ (left panel) and with $f_3 = 0$ (right panel). The white region, where the decay $\phi_2 \to \phi_1\pi^0$ is kinematically accessible, is disregarded in our analysis. See main text for details.

integrating out a vector-like pair of heavy fermions,

$$
\frac{\Gamma_{\phi_1\gamma\gamma}}{\Gamma_{\phi_1 e^+ e^-}} \simeq \frac{\pi}{56} \frac{\Delta^2 \, g^{-2} \, (m_1/m_2)}{\tan^2 \arg(Y_1 Y_2^*)} \frac{{}_2F_1(3,4,8;\Delta)}{{}_2F_1(1,3,6;\Delta)} \,,
$$
$$
\frac{\Gamma_{\phi_1\gamma\gamma}}{\sum_i \Gamma_{\phi_1 \nu_i \bar{\nu}_i}} \simeq \frac{3\pi}{2 \left(c_v^{(f)\,2} + c_a^{(f)\,2} \right)} \frac{g^{-2} \, (m_1/m_2)}{\tan^2 \arg(Y_1 Y_2^*)} \frac{m_z^4 \cos^4 \theta_W}{M_2^4 \Delta^2} \frac{{}_2F_1(3,4,8;\Delta)}{{}_2F_1(3,5,10;\Delta)} \,.
\tag{5.2.15}
$$

The branching ratios for the decay $\phi_2 \to \phi_1\gamma\gamma$ both for the Higgs mediated scenario (left) and for the fermion loop scenario (right) are shown in Fig. 5.3 for different values of Δ with $M_2 - M_1 \leq m_\pi$, taking for concreteness $m_2 \simeq 5\,m_1$ and $\arg(Y_1 Y_2^*) = \pi/4$. One concludes from the plot that the decay $\phi_2 \to \phi_1\gamma\gamma$ has a sizable or dominant branching ratio in a substantial part of the parameter space. Therefore, the model could be testable with gamma-ray observations.

The (normalized) differential energy spectrum in this scenario can be cast as:

$$
\frac{1}{\Gamma_{\phi_1\gamma\gamma}} \frac{d\Gamma_{\phi_1\gamma\gamma}}{dx_\gamma} = \frac{140}{{}_2F_1(3,4,8;\Delta)} \frac{x_\gamma^3 (1 - x_\gamma)^3}{(1 - x_\gamma \Delta)^3} \,,
\tag{5.2.16}
$$
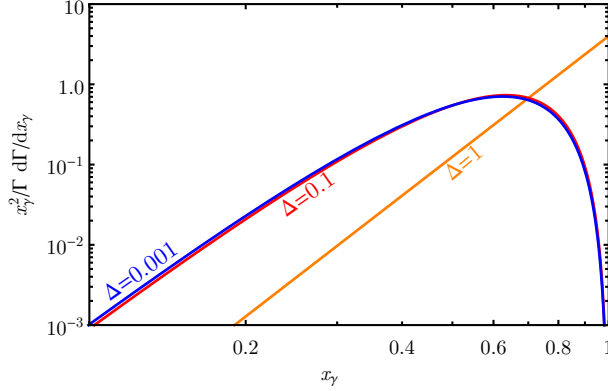
Figure 5.4: Differential energy spectrum of photons produced in the decay $\phi_2 \to \phi_1 \gamma\gamma$ for different values of the degeneracy parameter Δ when the decay process can be described by the effective theory presented in Section 5.2.

which only depends on the mass splitting parameter Δ and on the variable x. The energy spectrum is shown in Fig. 5.4, for three representative values of Δ. The spectrum presents a maximum at $x = (1 - \sqrt{1 - \Delta})/\Delta$, which takes values between $1/2$ and 1 for $\Delta \to 0$ and $\Delta \to 1$. In terms of the photon energy, this is equivalent to a peak at $E_\gamma = \dfrac{M_2}{2}(1 - \sqrt{1 - \Delta})$, which takes values between $E_\gamma = \frac{1}{4}M_2\Delta$ and $E_\gamma = \frac{1}{2}M_2\Delta$ for $\Delta \to 0$ and $\Delta \to 1$, respectively. Notably, and regardless of the value of the parameter Δ, the energy spectrum presents a sharp peak close to the kinematical endpoint, which could stand out over the featureless spectrum of the isotropic diffuse gamma-ray emissions.

The flux of photons received on Earth from the decay $\phi_2 \to \phi_1 \gamma\gamma$ receives two main contributions. The extragalactic contribution is generated by the decay of dark matter particles distributed homogeneously and isotropically in the Universe, and has a differential spectrum given by (see eqn. 2.4.2 in chapter 2)

$$\frac{d\Phi_{\rm eg}}{dE_\gamma} = \frac{1}{4\pi} \frac{\Omega_{\phi_2}\rho_{\rm c}}{M_2} \int_0^\infty \frac{dz}{H(z)} \frac{d\Gamma}{dE_\gamma}\left[(z+1)E_\gamma\right] \, e^{-\tau(E_\gamma, z)} \,, \tag{5.2.17}$$

which includes contributions from all redshifts z. Here, $\rho_{\rm c} = 4.9 \times 10^{-6}\,{\rm GeV\,cm^{-3}}$ is the critical density of the Universe, $H(z) = H_0\sqrt{\Omega_\Lambda + \Omega_{\rm m}(z+1)^3}$ is the (redshift-dependent) Hubble parameter, and $\tau(E_\gamma, z)$ is the optical depth, which determines the attenuation of the gamma-ray flux in their propagation from the decay point to the Earth. In our analysis we have adopted $\Omega_\Lambda = 0.69$, $\Omega_{\rm m} = 0.31$ [10], and the parametrization of the optical depth presented in [117]. The second contribution stems from the decay of dark matter particles
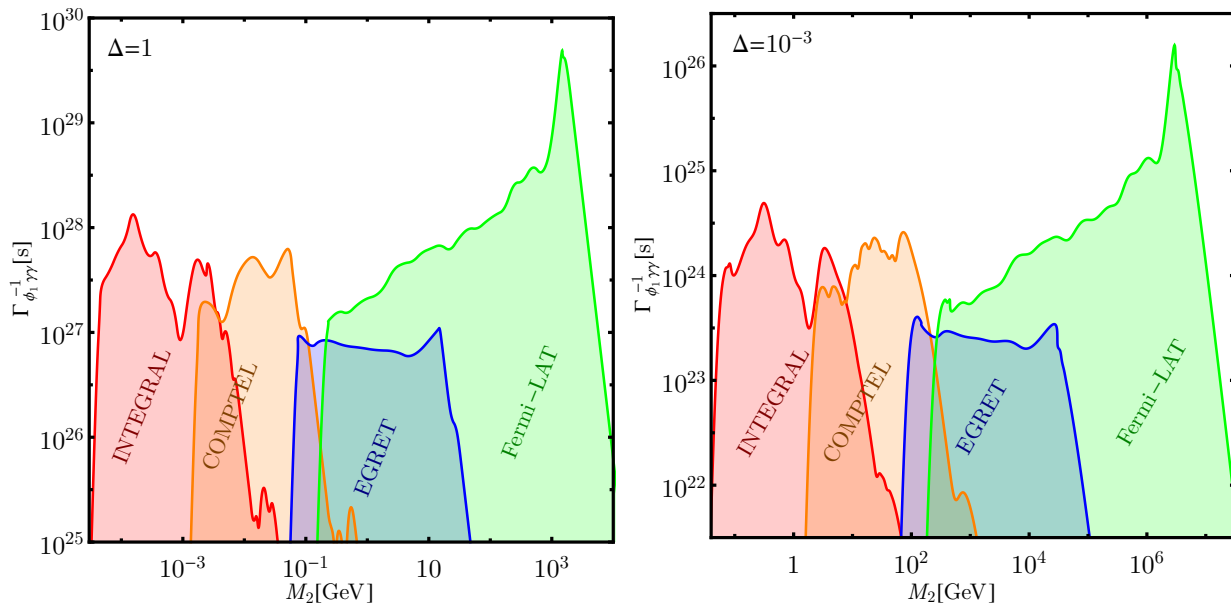
Figure 5.5: Lower limit on the inverse width of the decay process $\phi_2 \to \phi_1 \gamma\gamma$ as a function of the mass of the decaying dark matter component M_2, for a very hierarchical ($\Delta = 1$, left panel) and a very degenerate ($\Delta = 10^{-3}$, right panel) dark matter mass spectrum.

in the Milky Way halo, and is given by (see eqn. 2.4.1 in chapter 2):

$$\frac{d\Phi_{\text{halo}}}{dE_\gamma}(\psi) = \frac{1}{4\pi M_2} \frac{\Omega_{\phi_2}}{\Omega_{\text{DM}}} \frac{d\Gamma}{dE_\gamma} \int_0^\infty ds\, \rho_{\text{DM}}[r(s, \psi)] \,, \tag{5.2.18}$$

where we have assumed that the fraction of the dark matter mass density in the form of the unstable component ϕ_2 is the same in the Milky Way and in the Universe at large scale: $\rho_{\phi_2}/\rho_{\text{DM}} = \Omega_{\phi_2}/\Omega_{\text{DM}}$. In determining the galactic contribution to the gamma-ray flux, $\frac{d\Phi_{\text{halo}}}{dE_\gamma}(\psi)$ we have assumed the Navarro-Frenk-White (NFW) dark matter halo profile [216] with scale radius $r_s = 21\,\text{kpc}$, local dark matter density $\rho_\odot = 0.3\,\text{GeV/cm}^3$ and distance of the Sun to the Milky Way center $r_\odot = 8.5\,\text{kpc}$.

The non-observation of a statistically significant sharp feature in the isotropic diffuse photon flux determined by INTEGRAL [217], COMPTEL [218], EGRET [219] and the Fermi-LAT [220] leads to limits on the width of the dark matter decay channel $\phi_2 \to \phi_1 \gamma\gamma$, which are shown in Fig. 5.5 as a function of the dark matter mass, and for two different values of the mass splitting parameter $\Delta = 1$(left panel) and 10^{-3}(right panel). The limits have been derived assuming that $\Omega_{\phi_2}h^2 = \Omega_{DM}h^2$ and imposing that the predicted photon flux does not exceed the 2σ limit reported by the experiment in every energy bin. We have

assumed a flat energy resolution $\sigma(E)/E = 0.1$ throughout our analysis. The contribution to the photon flux from inverse Compton scattering has been neglected; therefore our limits can be regarded as conservative. In principle, a given experiment is sensitive to arbitrarily large dark matter masses, due to the low energy tail in the photon energy spectrum. On the other hand, the photon multiplicity decreases rapidly, as x_γ^{-3}, when $x_\gamma \ll 1$, while the measured photon flux scales roughly as E_γ^{-2}. As a result, the range of masses to which the experiment is sensitive is effectively bounded from above as well.

We obtain that current observations require $\Gamma^{-1}_{\phi_1\gamma\gamma} \gtrsim 5 \times 10^{26}$ s for $\Delta = 1$ and for a mother particle with mass M_2 in the range 40 keV $-$ 1 TeV. As the spectrum becomes more and more degenerate, the limits on the inverse width become weaker, approximately by a factor $\Delta/2$ (this is due to the fact that the energy of the peak is proportional to $1 - \sqrt{1-\Delta} \simeq \Delta/2$, combined with the fact that the observational limits are roughly flat with the energy of the photon). For $\Delta = 10^{-3}$ the inverse width is therefore restricted to be $\Gamma^{-1}_{\phi_1\gamma\gamma} \gtrsim 2.5 \times 10^{23}$ s when the mother dark matter particle mass is in the range $M_2 = 80\,\mathrm{MeV} - 2\,\mathrm{PeV}$.

5.3   Scalar dark sector coupled to SM fermions

In the previous section we have considered a possible UV completion to the effective interaction Eq.(5.2.3) consisting in one heavy Z_2-even fermion and one heavy Z_2-odd fermion, with the same gauge quantum numbers. The Standard Model contains already various Z_2-even fermions, therefore, an obvious variant of the aforementioned scenario consists in identifying ψ_1 with any Standard Model fermion, which we denote by f, and ψ_2 with a heavy Z_2-odd exotic fermion. If the Standard model fermion is also heavy, $m_1 \gg M_2, M_1$, the results of the previous section apply. However, if the dark matter particles interact with a light Standard Model fermion, a separate analysis is necessary. In this section we focus in the scenario where $M_2 - M_1 \gg m_1$, so that the decay $\phi_2 \to \phi_1 f\bar{f}$ proceeds at tree level (since ψ_1 is identified with f). The decay $\phi_2 \to \phi_1 \gamma\gamma$, on the other hand, still proceeds at the one loop level. However, due to the lightness of the Standard Model fermion in the loop, the process cannot be described by the effective interactions constructed in the previous Section.

For simplicity, we will assume in this section that the Higgs portal interaction is negligible, so that the decays proceed dominantly by the interactions with the Standard Model fermion and the Z_2-odd exotic fermion. The amplitude for the process $\phi_2 \to \phi_1 f\bar{f}$ can be obtained from the effective interaction

$$-\mathcal{L}_{int} \supset \frac{\mathrm{Re}(Y_1 Y_2^*)}{2m_2^2} \bar{f}\gamma^\mu \left(a\, P_L + b\, P_R\right) f \left(\phi_1 \overset{\leftrightarrow}{\partial_\mu} \phi_2\right), \tag{5.3.1}$$

where $P_{L,R}$ are the chiral projection operators. On the other hand, and as said above, the decay $\phi_2 \to \phi_1\gamma\gamma$ cannot be described by an effective interaction and the amplitude must be calculated instead from the full Lagrangian. We obtain

$$\mathcal{A}(\phi_2 \to \phi_1\gamma\gamma) = \frac{\alpha_{\rm EM}}{\pi}\frac{m_1}{m_2}{\rm Re}(Y_1Y_2^*)\,\mathcal{I}\left(\frac{m_1^2}{k_1k_2}\right)\left[\eta^{\mu\nu} - \frac{k_1^\mu k_2^\nu}{k_1k_2}\right]\epsilon_{1\nu}\epsilon_{2\mu}\,, \tag{5.3.2}$$

where $k_{1,2}$ and $\epsilon_{1,2}$ are the four-momenta and the polarizations of the emitted photons, and the loop function $\mathcal{I}(x)$ is given by

$$\mathcal{I}(x) = 1 + \frac{1}{2}(1-2x)\left[{\rm Li}_2\left(\frac{1+\sqrt{1-2x}}{x}\right) + {\rm Li}_2\left(\frac{1-\sqrt{1-2x}}{x}\right)\right]. \tag{5.3.3}$$

For $x \geq 1/2$ the function $\mathcal{I}(x)$ is real and monotonically decreasing, while for $x \leq 1/2$, $\mathcal{I}(x)$ contains an imaginary part due to the on-shellness of the loop fermion ψ_1. Approximate expressions for $\mathcal{I}(x)$ are

$$\mathcal{I}(x) \approx \begin{cases} \left(1+\frac{\pi^2}{4}\right) - \frac{1}{4}(1-2x)\log^2\frac{x}{2} - \frac{x}{2}(\pi^2 + \log\frac{x}{2}) + i\frac{\pi}{2}(1-2x)\log\frac{x}{2} & \text{for } x \ll 1 \\ \frac{1}{3x} + \frac{7}{180x^2} & \text{for } x \gg 1 \end{cases}. \tag{5.3.4}$$

The differential rate for the process $\phi_2 \to \phi_1 f\bar{f}$ reads, under the assumption $M_2 - M_1 \gg 2m_f$,

$$\frac{d\Gamma_{\phi_1 f\bar{f}}}{dx_f} = \frac{1}{64\pi^3}{\rm Re}(Y_1Y_2^*)^2\left(\frac{M_2^5\Delta^5}{m_2^4}\right)\frac{x_f^2(1-x_f)^2}{(1-x_f\Delta)}\,, \tag{5.3.5}$$

resulting in a partial decaywidth

$$\Gamma_{\phi_1 f\bar{f}} = \frac{1}{1920\pi^3}{\rm Re}(Y_1Y_2^*)^2\left(\frac{M_2^5\Delta^5}{m_2^4}\right){}_2F_1(1,3,6;\Delta). \tag{5.3.6}$$

On the other hand, the differential decaywidth for $\phi_2 \to \phi_1\gamma\gamma$ reads,

$$\frac{d\Gamma_{\phi_1\gamma\gamma}}{dx_\gamma} = \frac{\alpha_{\rm EM}^2}{128\pi^5}{\rm Re}(Y_1Y_2^*)^2\left(\frac{m_1^4\Delta}{M_2m_2^2}\right)F_{\gamma\gamma}(x_\gamma)\,, \tag{5.3.7}$$

where

$$F_{\gamma\gamma} = \int_{z_{\rm min}}^\infty dz\frac{|\mathcal{I}(z)|^2}{z^2} \approx \begin{cases} \frac{1}{27z_{\rm min}^3} & \text{for } z_{\rm min} \gg 1 \\ \frac{1}{z_{\rm min}}\left(12.8 + 0.062\log^4 z_{\rm min}\right) & \text{for } z_{\rm min} \ll 1 \end{cases}. \tag{5.3.8}$$

with $z_{\rm min} = \frac{2m_1^2}{M_2^2}\frac{(1-x_\gamma\Delta)}{(1-x_\gamma)x_\gamma\Delta^2}$. We note that the regime $M_2 - M_1 < 2m_1\,(> 2m_1)$ corresponds to $z_{\rm min} > 1/2\,(< 1/2)$.
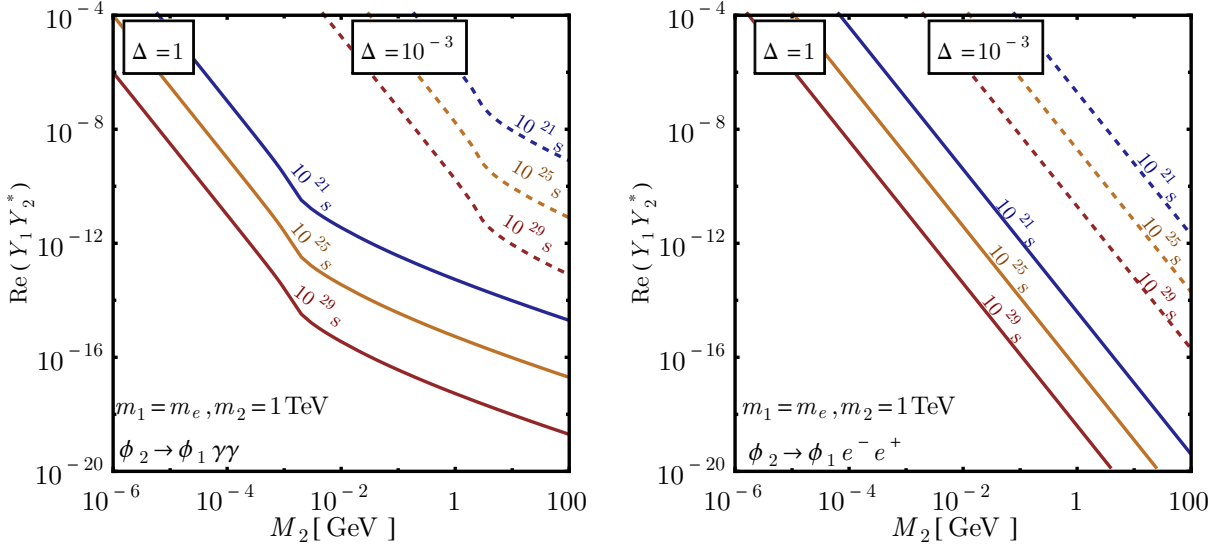
Figure 5.6: Same as Fig. 5.2, but for the scenario described in Section 5.3 where the two dark matter components have Yukawa couplings $Y_{1,2}$ to a light Z_2-even fermion and a heavy Z_2-odd exotic fermion. For the plot we have assumed that the Z_2-even fermion is an electron and that the Z_2-odd fermion has mass $m_2 = 1$ TeV.

Thus, from Eq. (5.3.7) and (5.3.8) one obtains:

$$\frac{d\Gamma_{\phi_1\gamma\gamma}}{dx_\gamma} \approx \frac{\alpha_{\rm EM}^2}{128\pi^5} {\rm Re}(Y_1 Y_2^*)^2 \left(\frac{m_1^4 \Delta}{M_2 m_2^2}\right) \begin{cases} \dfrac{M_2^6 \Delta^6}{216\, m_1^6} \dfrac{x_\gamma^3 (1-x_\gamma)^3}{(1-x_\gamma\Delta)^3} & \text{for } M_2 - M_1 \ll 2\,m_1 \\[2ex] \dfrac{M_2^2 \Delta^2}{2\, m_1^2} \dfrac{x_\gamma (1-x_\gamma)}{(1-x_\gamma\Delta)} \left[12.8 + 0.062 \log^4\left(\dfrac{2m_1^2}{M_2^2} \dfrac{(1-x_\gamma\Delta)}{(1-x_\gamma)\, x_\gamma\Delta^2}\right)\right] \\ & \text{for } M_2 - M_1 \gg 2\,m_1 \end{cases} .$$

$$(5.3.9)$$

Approximate expressions for the partial decay rates are:

$$\Gamma_{\phi_1 f\bar{f}} \simeq \left(10^{26}{\rm s}\right)^{-1} \left(\frac{{\rm Re}(Y_1 Y_2^*)}{2.1 \times 10^{-17}}\right)^2 \left(\frac{m_2}{1\,{\rm TeV}}\right)^{-4} \left(\frac{M_2}{1\,{\rm GeV}}\right)^5 \Delta^5\, {}_2F_1\left(1, 3, 6; \Delta\right),$$

$$\Gamma_{\phi_1\gamma\gamma} \simeq \left(10^{26}{\rm s}\right)^{-1} \left(\frac{m_2}{1\,{\rm TeV}}\right)^{-2}$$

91
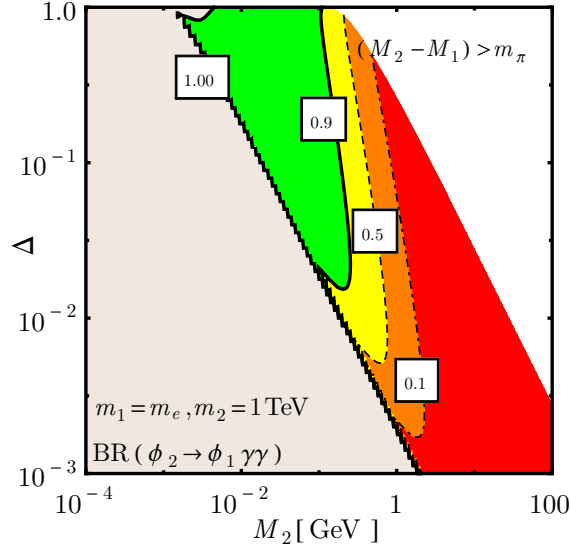
Figure 5.7: Same as Fig. 5.3, but for the scenario described in Section 5.3. For the plot we have assumed that the Z_2-even fermion is an electron and that the Z_2-odd fermion has mass $m_2 = 1$ TeV.

$$
\times
\begin{cases}
\left(\dfrac{\mathrm{Re}(Y_1 Y_2^*)}{6.3\times 10^{-20}}\right)^2 \left(\dfrac{m_e}{m_1}\right)^2 \left(\dfrac{M_2}{1\,\mathrm{GeV}}\right)^5 \Delta^7 {}_2F_1\left(3,4,8;\Delta\right) & \text{for } M_2 - M_1 \ll 2m_1 \\[2.5ex]
\left(\dfrac{\mathrm{Re}(Y_1 Y_2^*)}{6\times 10^{-15}}\right)^2 \left(\dfrac{m_1}{m_e}\right)^2 \left(\dfrac{M_2}{1\,\mathrm{GeV}}\right) \Delta^3 \times \\[2.5ex]
\quad \left[\left(1 + \dfrac{1}{200}\log^4\left(\dfrac{M_2^2\Delta^2}{2m_1^2}\right)\right) {}_2F_1\left(1,2,4;\Delta\right) + 0.03\,\mathcal{J}\left(M_2,m_1,\Delta\right)\right] \\[2.5ex]
& \text{for } M_2 - M_1 \gg 2m_1
\end{cases}
,
$$

$$(5.3.10)$$

where,

$$
\mathcal{J}\left(M_2,m_1,\Delta\right) \equiv \int_0^1 dx_\gamma \frac{x_\gamma(1-x_\gamma)}{(1-\Delta\,x_\gamma)}
$$
$$
\left[4\log^3\left(\frac{M_2^2\Delta^2}{2m_1^2}\right)\log\left[\frac{x_\gamma(1-x_\gamma)}{(1-\Delta\,x_\gamma)}\right] + 6\log^2\left(\frac{M_2^2\Delta^2}{2m_1^2}\right)\log^2\left[\frac{x_\gamma(1-x_\gamma)}{(1-\Delta\,x_\gamma)}\right]\right].
$$

$$(5.3.11)$$

Fig. 5.6 shows contour lines of the inverse widths into $\phi_1\gamma\gamma$ (left panel) and into $\phi_1 e^+ e^-$ (right panel), in the parameter space spanned by $\mathrm{Re}(Y_1 Y_2^*)$ and M_2, for $\Delta = 1$ and $\Delta = 10^{-3}$,
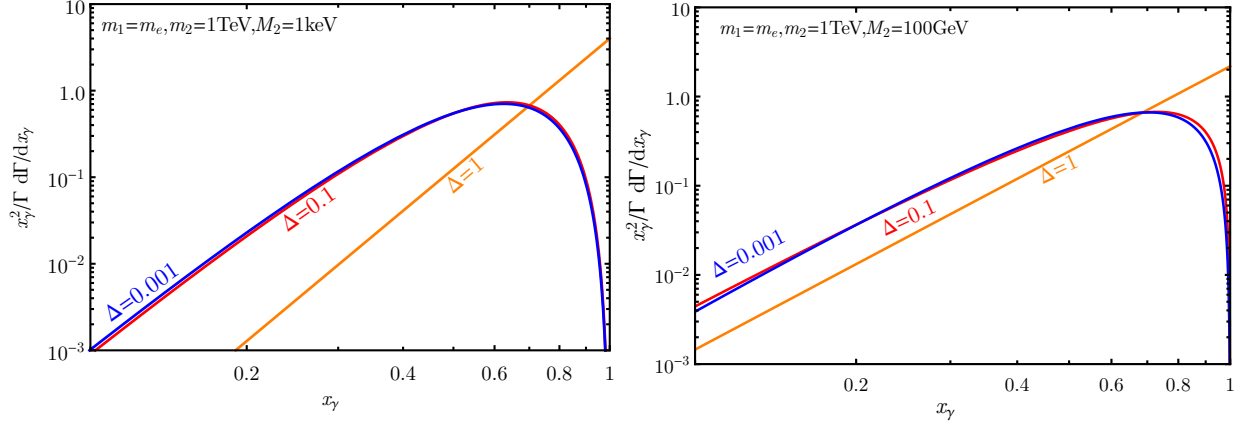
Figure 5.8: Same as Fig. 5.4, but for the scenario described in Section 5.3. For the plot we have assumed that the Z_2-even fermion is an electron, that the Z_2-odd fermion has mass $m_2 = 1$ TeV, and that the decaying dark matter component mass is $M_2 = 1$ keV (left panel) and $M_2 = 100$ GeV (right panel).

taking for concreteness a model where the dark matter particles couple to an electron and to a Z_2-odd exotic fermion with mass $m_2 = 1$ TeV.

The ratio of rates can be calculated from Eq. (5.3.10). One finds that

$$
\frac{\Gamma_{\phi_1\gamma\gamma}}{\Gamma_{\phi_1 f\bar{f}}} \simeq
\begin{cases}
\dfrac{\alpha_{\text{EM}}^2 \Delta^2}{2016\pi^2} \left(\dfrac{m_2}{m_1}\right)^2 \dfrac{{}_2F_1(3,4,8;\Delta)}{{}_2F_1(1,3,6;\Delta)} & \text{for } M_2 - M_1 \ll 2m_1 \\[3mm]
\dfrac{639\,\alpha_{\text{EM}}^2}{20\pi^2\,\Delta^2} \left(\dfrac{m_1^2 m_2^2}{M_2^4}\right) \times & \\[2mm]
\dfrac{\left[\left(1 + \frac{1}{200}\log^4\left(\frac{M_2^2\Delta^2}{2m_1^2}\right)\right) {}_2F_1\left(1,2,4;\Delta\right) + 0.03\,\mathcal{J}\left(M_2,m_1,\Delta\right)\right]}{{}_2F_1\left(1,3,6;\Delta\right)} & \\[3mm]
& \text{for } M_2 - M_1 \gg 2m_1
\end{cases}
\tag{5.3.12}
$$

It follows from these expressions that $\phi_2 \to \phi_1\gamma\gamma$ can have a sizable branching ratio, especially when $m_2 \gg m_1, M_2$. This is illustrated in Fig. 5.7, which shows contour lines of the branching ratio for $\phi_2 \to \phi_1\gamma\gamma$ for different values of Δ and M_2, for the specific case where the Standard Model fermion is an electron and the Z_2-odd exotic fermion has mass $m_2 = 1$ TeV.

The (normalized) differential photon spectrum is in this case

$$\frac{1}{\Gamma_{\phi_1\gamma\gamma}}\frac{d\Gamma_{\phi_1\gamma\gamma}}{dx_\gamma} \simeq \begin{cases} \dfrac{140}{{}_2F_1(3,4,8;\Delta)}\dfrac{x_\gamma^3(1-x_\gamma)^3}{(1-x_\gamma\,\Delta)^3} & \text{for } M_2 - M_1 \ll 2m_1, \\[2ex] \dfrac{x_\gamma(1-x_\gamma)}{(1-\Delta\,x_\gamma)}\dfrac{6 + 0.03\,\log^4\left[\left(\frac{2m_1^2}{M_2^2\Delta^2}\right)\frac{(1-\Delta\,x_\gamma)}{x_\gamma(1-x_\gamma)}\right]}{\left[\left(1+\frac{1}{200}\log^4\left(\frac{M_2^2\Delta^2}{2m_1^2}\right)\right){}_2F_1\left(1,2,4;\Delta\right) + 0.03\mathcal{J}\left(M_2,m_1,\Delta\right)\right]} \\[2ex] & \text{for } M_2 - M_1 \gg 2m_1 \end{cases} ,$$

$$(5.3.13)$$

which is mostly dependent on the parameter Δ, but also has a mild dependence on M_2. The differential photon spectrum is shown in Fig. 5.8, taking for illustration $M_2 = 1$ keV (left panel) and M_2=100 GeV (right panel). The differential spectrum is qualitatively similar to the one obtained in the effective theory approach analyzed in Section 5.2, although shows some quantitative differences. The corresponding limits on the inverse width from gamma-ray telescopes are shown in Fig. 5.9, for the representative cases $\Delta = 1$ (left panel) and $\Delta = 10^{-3}$ (right panel), for the case when the Standard Model fermion in the loop is an electron.

5.4 A supersymmetric scenario

As pointed out in chapter 4, MSSM augmented with three generations of right-handed neutrino superfields with only Dirac masses for the neutrinos allows the possibility of realizing a feebly interacting scalar dark sector comprising right-chiral sneutrinos [76, 126, 157, 158, 200, 221–224]. In case the sneutrino masses have a common origin at high-scale, they are likely to be nearly degenerate at the electroweak scale, since their renormalization group equation is driven by the neutrino trilinear coupling [126, 164] which is usually proposed to be proportional to neutrino Yukawa coupling y_ν, the proportionality constant being a SUSY breaking mass-scale A_ν.

When the mass difference is smaller than twice the electron mass, the heavier sneutrino ($\tilde{\nu}_i$) decays into the lighter sneutrino and a neutrino-antineutrino pair via the exchange of virtual neutralinos, or into the lighter sneutrino and two photons. For unitary sneutrino mixing, it can be checked that the coupling $\tilde{\nu}_i\tilde{\nu}_k\,h\,(Z)$ is forbidden for $i \neq k$ and hence the decays cannot occur via the mediation of a virtual Higgs (Z) boson. The decay can however proceed at the one loop level via diagrams such as the ones in Fig. 5.10. Assuming that all supersymmetric particles, excepting the right-handed sneutrinos, are at the mass scale
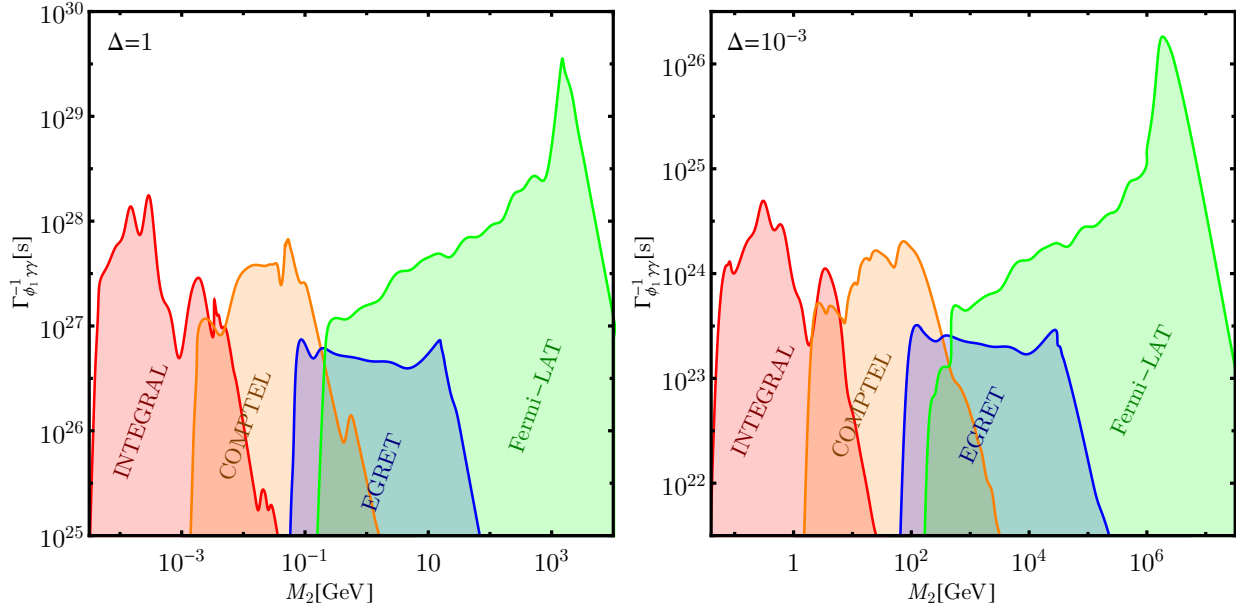
Figure 5.9: Lower limit on the inverse width of the decay process $\phi_2 \to \phi_1 \gamma\gamma$ as a function of the mass of the decaying dark matter component M_2, for a very hierarchical ($\Delta = 1$, left panel) and a very degenerate ($\Delta = 10^{-3}$, right panel) dark matter mass spectrum with $\psi_1 =$ electron for illustration.
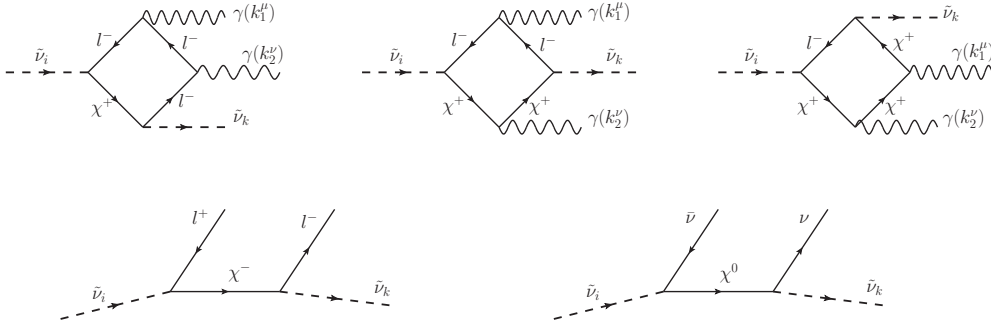
Figure 5.10: Feynman diagrams giving the dominant contribution to the decay processes $\tilde{\nu}_i \to \tilde{\nu}_k \gamma\gamma, \tilde{\nu}_i \to \tilde{\nu}_k e^- e^+$ and $\tilde{\nu}_i \to \tilde{\nu}_k \nu\bar{\nu}$. Diagrams where the photon lines are interchanged (not shown in the Figure) also contribute to the amplitudes.

$m_{\rm SUSY}$, and $m_{\tilde{\nu}_{Ri}} \ll m_{\rm SUSY}$, we checked that the dominant contribution to the amplitude comes from lepton(l^-)-chargino(χ^-) loops, which is enhanced by a factor $\sim m_{\rm SUSY}/m_l$ compared to other contributions. This scenario, therefore, falls into the class of models analyzed in Section 5.3. Assuming a scheme of *minimal flavour violation* [225–228] in the leptonic sector, the Yukawa coupling of the sneutrino $i = 1, 2$ to the lepton $l = e, \mu, \tau$ is given by

$$Y_{il} = g_W \sin \Theta_{\tilde{\nu}_{ii}} U_{il} , \tag{5.4.1}$$

where g_W is weak gauge coupling, U_{il} are elements of the Pontecorvo-Maki-Nakagawa-Sakata (PMNS) matrix and $\Theta_{\tilde{\nu}_{ii}}$ is the mixing angle between the left-sneutrino of flavor i with the right-sneutrino of the same flavor and is provided in Eq.(4.2.5) with $2.8 \times 10^{-13} \lesssim (y_\nu \sin \beta) \lesssim 4.4 \times 10^{-13}$, as considered in chapter 4.

Particularizing Eq.(5.3.10) to this model, and taking for simplicity $A_\nu, m_{\tilde{\nu}_L} \sim m_{\rm SUSY} \gg m_{\tilde{\nu}_R}$, with $m_{\rm SUSY}$ being the overall SUSY mass scale, the partial rates in the different channels can be approximated as,

$$\Gamma_{\tilde{\nu}_i \to \tilde{\nu}_k \nu\bar{\nu}} \simeq \left(10^{26}{\rm s}\right)^{-1} \left(\frac{\sum\limits_{l,r=e,\mu,\tau} {\rm Re}(Y_{il}Y_{kr}^*)}{2.1 \times 10^{-17}}\right)^2 \left(\frac{m_{\rm SUSY}}{1\,{\rm TeV}}\right)^{-4} \left(\frac{m_{\tilde{\nu}_i}}{1\,{\rm GeV}}\right)^5 \Delta^5,$$

$$\Gamma_{\tilde{\nu}_i \to \tilde{\nu}_k e^- e^+} \simeq \left(10^{26}{\rm s}\right)^{-1} \left(\frac{{\rm Re}(Y_{ie}Y_{ke}^*)}{2.1 \times 10^{-17}}\right)^2 \left(\frac{m_{\rm SUSY}}{1\,{\rm TeV}}\right)^{-4} \left(\frac{m_{\tilde{\nu}_i}}{1\,{\rm GeV}}\right)^5 \Delta^5,$$

$$\Gamma_{\tilde{\nu}_i \to \tilde{\nu}_k \gamma\gamma} \simeq \left(10^{26}{\rm s}\right)^{-1} \left(\frac{m_{\rm SUSY}}{1{\rm TeV}}\right)^{-2}$$

$$\times \begin{cases} \left(\dfrac{{\rm Re}(Y_{ie}Y_{ke}^*)}{6.3 \times 10^{-20}}\right)^2 \left(\dfrac{m_{\tilde{\nu}_i}}{1\,{\rm GeV}}\right)^5 \Delta^7 & \text{for } m_{\tilde{\nu}_i} - m_{\tilde{\nu}_k} \ll 2m_e, \\[2ex] \left(\dfrac{{\rm Re}(Y_{ie}Y_{ke}^*)}{6 \times 10^{-15}}\right)^2 \left(\dfrac{m_{\tilde{\nu}_i}}{1\,{\rm GeV}}\right) \Delta^3 \left[1 + \dfrac{7}{5}\log^2\left(\dfrac{m_{\tilde{\nu}_i}^2 \Delta^2}{2\,m_e^2}\right)\right] & \text{for } m_{\tilde{\nu}_i} - m_{\tilde{\nu}_k} \gg 2m_e \end{cases}$$

$$\tag{5.4.2}$$

where we have assumed $\Delta \ll 1$.

When the mass difference between the sneutrinos is smaller than twice the electron mass, the only decays accessible are $\tilde{\nu}_i \to \tilde{\nu}_k \gamma\gamma$ and $\tilde{\nu}_i \to \tilde{\nu}_k \nu\bar{\nu}$, with ratio of the rates approximately given by

$$\frac{\Gamma_{\tilde{\nu}_i \to \tilde{\nu}_k \gamma\gamma}}{\Gamma_{\tilde{\nu}_i \to \tilde{\nu}_k \nu\bar{\nu}}} \simeq \frac{\alpha_{\rm EM}^2 \Delta^2}{2016\pi^2} \left(\frac{U_{ek}^\dagger U_{ie}}{\sum\limits_{l,r=e,\mu,\tau} U_{rk}^\dagger U_{il}}\right) \left(\frac{m_{\rm SUSY}^2}{m_e^2}\right) . \tag{5.4.3}$$

In this regime one has $\Delta \le 4m_e/m_{\tilde{\nu}_i}$, therefore the diphoton decay channel can dominate over the "invisible" decay channel if the mass difference is not too small and if $m_{\tilde{\nu}_i} \lesssim 1.1 \times$

$10^{-4}\, m_{\mathrm{SUSY}}$; if the mass difference between the sneutrinos is generated through quantum effects by the tiny neutrino Yukawa coupling, such that $\Delta \ll 4m_e/m_{\tilde{\nu}_i}$, then the decay will be dominated by the "invisible" channel.

When the right-sneutrino mass splitting is larger than twice the electron mass, $\Delta \geq 2m_e/m_{\tilde{\nu}_i}$ the loop and α_{EM} suppression factors in Eq. (5.4.3) can be compensated by the (possibly large) factor $m_{\mathrm{SUSY}}^2/m_{\tilde{\nu}_i}^2$. In this regime, furthermore, the decay channel $\tilde{\nu}_i \to \tilde{\nu}_k e^- e^+$ opens up. The ratio of the rates of $\tilde{\nu}_i \to \tilde{\nu}_k \gamma\gamma$ and $\tilde{\nu}_i \to \tilde{\nu}_k e^+ e^-$ is given by

$$\frac{\Gamma_{\tilde{\nu}_i \to \tilde{\nu}_k \gamma\gamma}}{\Gamma_{\tilde{\nu}_i \to \tilde{\nu}_k e^- e^+}} \quad \simeq \quad \frac{639\, \alpha_{\mathrm{EM}}^2}{40\pi^2} \left(\frac{m_{\mathrm{SUSY}}^2}{m_{\tilde{\nu}_i}^2} \right) \mathcal{F}\left(\frac{m_{\tilde{\nu}_i}^2 \Delta^2}{2m_e^2} \right) , \tag{5.4.4}$$

with $\mathcal{F}(x) = x^{-1}(1+7/5\log^2 x)$. This ratio is larger than 1 when the sneutrino is sufficiently light. On the other hand, in this regime $x \geq 2$, which implies $\mathcal{F}(x) \lesssim 0.93$. Therefore, the ratio Eq. (5.4.4) is necessarily smaller than 1 if $m_{\tilde{\nu}_i} \gtrsim 9 \times 10^{-3}\, m_{\mathrm{SUSY}}$.

For even larger masses, decays into a muon-antimuon pair, or mesons open up, usually taking a significant fraction of the total decaywidth.

The Yukawa couplings inducing the sneutrino decay are, in simple scenarios, related to the sneutrino dark matter density. Concretely, for sneutrino dark matter generated by freeze-in of the slepton decays $\tilde{l}_L \to \tilde{\nu}_R W$ and $\tilde{\nu}_L \to \tilde{\nu}_R Z$, the relic abundance can be approximated as (see appendix A.2 and [157]),

$$\Omega_{\tilde{\nu}_i} h^2 \simeq 0.12 \left(\frac{g_*}{106.75} \right)^{-3/2} \left(\frac{\sin\Theta_{\tilde{\nu}_{ii}}}{6.08 \times 10^{-12}} \right)^2 \left(\frac{\sin\beta}{1} \right)^{-2} \left(\frac{m_{\mathrm{SUSY}}}{1\,\mathrm{TeV}} \right) \left(\frac{m_{\tilde{\nu}_i}}{1\,\mathrm{GeV}} \right) , \tag{5.4.5}$$

where $\Theta_{\tilde{\nu}_{ii}}$ was defined in Eq. (4.2.5), which in turn determines the Yukawa couplings of the model through Eq. (5.4.1). We can then estimate the order of magnitude of the inverse width for the decay process $\tilde{\nu}_i \to \tilde{\nu}_k \gamma\gamma$ as

$$\Gamma_{\tilde{\nu}_i \to \tilde{\nu}_k \gamma\gamma} \simeq \sin^4\beta \left(\frac{m_{\mathrm{SUSY}}}{1\mathrm{TeV}} \right)^{-4}$$
$$\times \begin{cases} (5 \times 10^{33}\mathrm{s})^{-1} \left(\frac{m_{\tilde{\nu}_i}}{1\,\mathrm{GeV}} \right)^3 \Delta^7 & \text{for } m_{\tilde{\nu}_i} - m_{\tilde{\nu}_k} \ll 2m_e, \\ (2 \times 10^{36}\mathrm{s})^{-1} \left(\frac{m_{\tilde{\nu}_i}}{1\,\mathrm{GeV}} \right) \Delta^5 \mathcal{F}\left(\frac{m_{\tilde{\nu}_i}^2 \Delta^2}{2\,m_e^2} \right) & \text{for } m_{\tilde{\nu}_i} - m_{\tilde{\nu}_k} \gg 2m_e \end{cases} , \tag{5.4.6}$$

where we have assumed that $\tilde{\nu}_i$ accounts for most of the dark matter of the Universe, $|U_{ij}| \sim 1/\sqrt{3}$, $g_* = 106.75$ and $\Delta \ll 1$. It is clear from eqn. (5.4.6) that the choices of parameters favoured by freeze-in production result in a diphoton flux which is well below the sensitivity of current or future gamma-ray telescopes. In variants of this scenario, however, the prospects of detection might be more promising.

5.5 Conclusion

We have considered a dark matter scenario where the lightest and next-to-lightest particles of the dark sector are singlet scalars, odd under a discrete Z_2 symmetry, while the Standard Model particles are all even. The lightest scalar, ϕ_1, is assumed to be absolutely stable. However, the next-to-lightest scalar, ϕ_2, could decay into the lightest one together with Standard Model particles.

We have investigated the gamma-ray signatures produced in the decay. Angular momentum conservation forbids the decay $\phi_2 \to \phi_1 \gamma$, hence we have focused on the three-body decay $\phi_2 \to \phi_1 \gamma\gamma$, which presents a characteristic energy spectrum with a peak close to the kinematic end-point and which could be easily distinguished from the (featureless) astrophysical diffuse gamma-ray background.

We have constructed the most general CP-conserving effective Lagrangian inducing this decay either via a Higgs portal interaction or via dimension six operators, and we have proposed a UV complete model that generates those dimension six operators involving one Z_2-even and one Z_2-odd heavy fermion running in the loops. We have calculated the decay rates for the processes $\phi_2 \to \phi_1 \gamma\gamma$, $\phi_2 \to \phi_1 e^- e^+$ and $\phi_2 \to \phi_1 \nu\bar\nu$ and identified the regions of the parameter space where the branching ratio of $\phi_2 \to \phi_1 \gamma\gamma$ is sizable. We have also derived stringent limits on the inverse width for this process from the non-observation of such gamma-ray feature in the diffuse gamma-ray background inferred from the INTEGRAL, COMPTEL, EGRET and Fermi-LAT observations, both for large and for small mass differences between the two dark matter components. These limits in turn translate into stringent limits on the parameters of the model.

We have also analyzed a variant of our UV complete model where the Z_2-even fermion is identified with a Standard Model fermion. For this scenario, the effective theory approach to the decay $\phi_2 \to \phi_1 \gamma\gamma$ is not valid and therefore requires a separate analysis. In particular, we show that the photon energy spectrum (and accordingly the limits on the inverse width from gamma-ray data) differs from the one calculated in the effective theory approach. As a particular case of this scenario, we have considered the MSSM augmented by three right-handed neutrino superfields, and we have studied the gamma-ray signals generated in the decay of the next-to-lightest supersymmetric particle into the lightest in the case where the total lepton number is conserved. For freeze-in production the predicted gamma-ray flux is unfortunately many orders of magnitude below the sensitivity of current or future gamma-ray telescopes, due to the smallness of the neutrino Yukawa coupling. In other scenarios, however, the gamma-ray signal from $\phi_2 \to \phi_1 \gamma\gamma$ may be within the reach of experiments [56].

Chapter 6

Search for decaying heavy dark matter in an effective interaction framework: a comparison of γ-ray and radio observations

6.1 Introduction

Following our discussions in previous chapters indirect searches of dark matter annihilation as well as decay products can be considered as an alternative possibility to terrestrial searches of dark matter, consisting in direct detection via DM-neucleon scattering or missing energy in colliders. Though for dark matter mass in the electroweak scale, i.e., $\mathcal{O}(100\,\text{GeV})$, such detection strategies are very fruitful, for dark matter mass in the trans-TeV range both the procedures suffer from a dearth in signal. Such scarcity of signal events in direct search experiments is caused by the lowering of local number density of DM particles. The result is the weak limit on the elastic scattering cross-sections for a WIMP for masses exceeding a TeV. At the same time, low signal rates suppress collider signals with $\slashed{E}_T$. Therefore, the best bet as of now for trans-TeV DM particles is indirect signals in the form of high-energy SM particles from extra-terrestrial sources.

While indirect signals of a stable DM particle come mostly from its annihilation into SM particles [32, 229–232], it is not inconceivable that such a particle is not fully stable, as

pointed out in chapter 2, though its lifetime must exceed the age of the universe by at least ten orders of magnitude [40, 233]. Specifically, decaying dark matter with superweak interaction strength to the visible sector particles are envisioned quite often [57, 58]. Moreover, decay of heavier particles in the dark sector which has a lifetime much larger than the age of the universe can also give rise to similar indirect signals, as discussed in chapter 5. While observations from experiments like Fermi-LAT [220], AMS-02 [234, 235], HESS [236, 237], IceCube [238] etc. contribute to the existing limits, it is equally important to study the possibility of detecting such DM induced signals in future generation experiments.

Our aim in this chapter is to study decay of a heavy DM particle, realized in several scenarios containing non-thermal DM particles [239–246], by parameterizing the decay Lagrangian in terms of effective operators, using as illustration scalar DM particle(s) in single-component as well as multicomponent scenarios. The effective operators listed by us are assumed to be responsible for DM decays in galaxies. However, we take a model-independent view of the relic density [10], by not ruling out other production/annihilation channels. The assumption inbuilt in the present study is that only the effective operators under consideration here are responsible for indirect DM decay signals.

The limits on DM decay from γ-ray data to date come largely from the isotropic background caused by the intra-galactic DM distribution as well as the extra-galactic continuum, as has been calculated for a scalar dark sector decay in chapter 5. The limits coming from localised sources do not offer much of an improvement on this in general [247], since the emitted flux from DM decay goes as ρ_{DM}/m_{DM}, as against ρ_{DM}^2/m_{DM}^2 in the case of annihilation [111]. Thus the upper limits on DM lifetime mostly come from the Fermi-LAT data on isotropic gamma-ray, whenever they are available. The projected CTA sensitivity in such cases mostly require decaywidths that are already ruled out [248]. An exception is the situation where the DM mass exceeds about 1 TeV, and the DM decays directly into one or two photons. The available Fermi-LAT data in such a case offer no limits [211]. This is where the projected CTA measurements have been considered.

However, indirect signals of dark matter decay not only consists of gamma-ray spectra but also can be observed using radio synchrotron fluxes from dwarf spheroidal galaxies (dSph). While the existing radio data provide some constraints on the DM parameter space [231], the picture is likely to improve considerably when the Square Kilometer Array (SKA) telescope starts its operation [249]. Though the prospects of exploring trans-TeV stable DM via its pair-annihilation have already been discussed in recent studies [250, 251], the present chapter is aimed at extending this to decaying heavy DM, and also comparing the predicted results

to existing and future gamma-ray observations. The DM decay cascades here, just as in the case of annihilation, lead to energetic electron-positron pairs that execute cycloidal motion under the influence of galactic magnetic fields, leading to radio synchrotron emission whose flux is determined by solving the appropriate transport equation.

Keeping the above observations in mind, we focus here on gamma-ray predictions of CTA and constraints from Fermi-LAT using extra-galactic continuum as a source of decaying DM, vis-a-vis those for SKA, using Draco as an example of the target dSph. As has been mentioned above, scalar DM particles have been used to illustrate our point, although the conclusions are easily extendable to a fermionic dark sector. We consider various $SU(2)_L \times U(1)_Y$ invariant effective operators, as listed in the next section, driving DM decays in various channels. We have included two-body decays of the DM, as also three-body decays of one quasi-stable particle in the dark sector decaying into the lightest particle along with a pair of SM particles. Decays of the latter generate electron-positron pairs that are the ultimate sources of radio synchrotron emission. Comparing the upper limits on the decaywidth from gamma-ray data with those expected from the SKA observation we find that the latter can probe deeper into the DM parameter space in all the decay modes considered.

The chapter is organized as follows: In section 6.2 we have parametrized the DM decay into gauge boson as well as fermion pairs in terms of higher dimensional operators. Section 6.3 contains a brief discussion of the astrophysical signals of decaying DM, namely the γ-ray flux as well as the radio synchrotron flux. We have presented our findings in section 6.4. Finally we conclude and summarize in section 6.5. The necessary formulae used for our analysis can be found in the appendix A.3.

6.2   Effective operators

As mentioned in chapter 2 there can be scenarios where DM particle is not absolutely stable but decays, albeit very slowly [57,58] with a lifetime much larger than the age of the universe. More often than not, such decays are due to the breaking of some symmetries via some heavy exotic particles running in the loops and hence can be parametrized as higher-dimensional operators, as we have done in chapter 5. Parametrization of the decay of such a DM candidate by dimension-5 effective operators is strongly constrained [252], since in that case

$$\tau_{DM} \simeq 6.58 \times 10^4 \, \text{s} \left(\frac{m_{DM}}{1\,\text{TeV}}\right)^{-3} \left(\frac{\Lambda}{10^{19}\text{GeV}}\right)^2, \tag{6.2.1}$$

leaving out factors dependent on the spin of the DM particle. This exceeds the requisite lower limit only when $m_{DM} \leq \mathcal{O}(\text{MeV})$, even with $\Lambda \simeq 10^{19}\text{GeV}$ [210]. For most of the DM parameter space, one thus finds it more consistent to parametrize all the decay interactions of the DM by dimension-6 operators, the suppressant scale Λ being the mass scale of the new physics responsible for generating such interactions.

As has been mentioned in section 6.1, we simplify our analysis by confining ourselves to a scalar dark sector, though the features related to its detection pointed out by us apply to particles with spin as well. We consider two possible scenarios within this category:

1. A single-component dark matter which is quasi-stable over the age of the universe and has two-body decays into SM particles.

2. A multicomponent (two-component) scenario where the heavier of the two dark sector members is quasi-stable and decays into the lighter, stable one, along with visible SM particles.

We outline these two scenarios below [1].

6.2.1 Single-component scalar dark matter

Following the above observation, we postulate dimension-6 terms as being responsible for DM decays. Modulo some hitherto unspecified symmetry, broken by the vacuum expectation value (vev) of scalar DM field ϕ, the dimension-6 operators reduced to dimension-5 ones, dictating two-body DM decays [2]. The corresponding dimension-5 operators can be parameterised as [98, 253]:

$$-\mathcal{L}_{dim-5} \quad \supset \quad -\mathcal{L}_{dim-5}^{\text{gauge}} - \mathcal{L}_{dim-5}^{\text{fermion,1}} - \mathcal{L}_{dim-5}^{\text{fermion,2}} \tag{6.2.2}$$

where

$$-\mathcal{L}_{dim-5}^{\text{gauge}} \quad = \quad \frac{f_{WW}}{\Lambda}\phi\, W^{a\,\mu\nu}W^a_{\mu\nu} + \frac{f_{BB}}{\Lambda}\phi\, B^{\mu\nu}B_{\mu\nu},$$

---

[1]In principle, both of these features may be found in a multicomponent dark sector where the lightest particle, too, is long-lived but unstable. The analysis of such a scenario requires multiple effective interactions to be operative at the same time. We simplify our analysis by taking one type of effective operator at a time, where the nature of effective interactions gets related more transparently to aspects of DM decay observations in the γ-ray and radio ranges.

[2]Smallness of the effective dimension-5 operators can be justified by an appropriate vev for ϕ. Similarly decays like ϕ to a pair of SM higgs is assumed here to be negligible, by postulating a near-vanishing interaction between the dark sector scalars and the SM higgs.

$$-\mathcal{L}_{dim-5}^{\text{fermion,1}} = \phi\left(\frac{f_{QQ}}{\Lambda}\bar{Q}_L\gamma^\mu D_\mu Q_L + \frac{f_{uu}}{\Lambda}\bar{u}_R\gamma^\mu D_\mu u_R + \frac{f_{dd}}{\Lambda}\bar{d}_R\gamma^\mu D_\mu d_R\right)$$

$$+\phi\left(\frac{f_{l_L l_L}}{\Lambda}\bar{l}_L\gamma^\mu D_\mu l_L + \frac{f_{l_R l_R}}{\Lambda}\bar{l}_R\gamma^\mu D_\mu l_R\right),$$

$$= \phi\,\frac{f_{qq}}{\Lambda}\left(\bar{Q}_L\gamma^\mu D_\mu Q_L + \bar{u}_R\gamma^\mu D_\mu u_R + \bar{d}_R\gamma^\mu D_\mu d_R\right)$$

$$+\phi\,\frac{f_{ll}}{\Lambda}\left(\bar{l}_L\gamma^\mu D_\mu l_L + \bar{l}_R\gamma^\mu D_\mu l_R\right),$$

$$-\mathcal{L}_{dim-5}^{\text{fermion,2}} = \phi\left[\frac{f_{uuH}}{\Lambda}\bar{Q}_L u_R \tilde{H} + \frac{f_{ddH}}{\Lambda}\bar{Q}_L d_R H + \frac{f_{lH}}{\Lambda}\bar{l}_L l_R H + h.c\right], \qquad (6.2.3)$$

with Λ being the suppression scale. Here ϕ is $SU(2)_L \times U(1)_Y$-singlet thus making each operator invariant under the electroweak group. While presenting our results, we will however consider only one operator to be dominant at a time, for the sake of simplicity. In each such case the two-body decays in the respective final states is taken to dominate DM decay, the three-body decays driven by the corresponding operators being understandably suppressed. For simplicity we have also assumed that $f_{QQ} = f_{uu} = f_{dd} \equiv f_{qq}$ and $f_{l_L l_L} = f_{l_R l_R} \equiv f_{ll}$ while presenting our results. Expressions for the two-body partial decaywidths are given in appendix A.3.1.

6.2.2 Multicomponent scalar dark sector

As an alternative scenario, we consider a multicomponent dark sector containing two SM singlet Z_2-odd real scalars ϕ_2 and ϕ_1. We assume ϕ_2 (identifying $M_2 \equiv m_{DM}$, as the mass of the decaying dark matter) is heavier than ϕ_1 (with mass M_1) and ϕ_2 decays to ϕ_1 with a lifetime much larger than the age of the universe [254], a scenario similar to the one we have studied in chapter 5. We parametrize these decay modes in terms of several dimension-6 operators [253] [3],

$$-\mathcal{L}_{dim-6} \supset -\mathcal{L}_{dim-6}^{\text{gauge}} - \mathcal{L}_{dim-6}^{\text{fermion,1}} - \mathcal{L}_{dim-6}^{\text{fermion,2}} \qquad (6.2.4)$$

where

$$-\mathcal{L}_{dim-6}^{\text{gauge}} = \frac{f_{WW}}{\Lambda^2}\phi_2\phi_1 W^{a\,\mu\nu}W^a_{\mu\nu} + \frac{f_{BB}}{\Lambda^2}\phi_2\phi_1 B^{\mu\nu}B_{\mu\nu} + \frac{f_B}{\Lambda^2}\left(\partial_\mu\phi_2\partial_\nu\phi_1 - \partial_\nu\phi_2\partial_\mu\phi_1\right)B^{\mu\nu},$$

$$-\mathcal{L}_{dim-6}^{\text{fermion,1}} = \phi_2\overset{\leftrightarrow}{\partial}_\mu\phi_1\left(\frac{f_{QQ}}{\Lambda^2}\bar{Q}_L\gamma^\mu Q_L + \frac{f_{uu}}{\Lambda^2}\bar{u}_R\gamma^\mu u_R + \frac{f_{dd}}{\Lambda^2}\bar{d}_R\gamma^\mu d_R\right.$$

---

[3]We have neglected the dimension-4 interaction term $\lambda_{12}\phi_2\phi_1 H^\dagger H$ compared to the dimension-6 effective operators presented in Eqn. 6.2.5.

$$+\frac{f_{l_L l_L}}{\Lambda^2}\bar{l}_L\gamma^\mu l_L + \frac{f_{l_R l_R}}{\Lambda^2}\bar{l}_R\gamma^\mu l_R\Bigg),$$

$$= \phi_2\overset{\leftrightarrow}{\partial}_\mu\phi_1\frac{f_{qq}}{\Lambda^2}\Bigg(\bar{Q}_L\gamma^\mu Q_L + \bar{u}_R\gamma^\mu u_R + \bar{d}_R\gamma^\mu d_R\Bigg)$$

$$+\phi_2\overset{\leftrightarrow}{\partial}_\mu\phi_1\frac{f_{ll}}{\Lambda^2}\Bigg(\bar{l}_L\gamma^\mu l_L + \bar{l}_R\gamma^\mu l_R\Bigg),$$

$$-\mathcal{L}^{\text{fermion},2}_{dim-6} = \phi_2\phi_1\left[\frac{f_{uuH}}{\Lambda^2}\bar{Q}_L u_R\tilde{H} + \frac{f_{ddH}}{\Lambda^2}\bar{Q}_L d_R H + \frac{f_{llH}}{\Lambda^2}\bar{l}_L l_R H + h.c\right]. \qquad (6.2.5)$$

The interactions shown in $\mathcal{L}^{\text{gauge}}_{dim-6}$ generate the terms of eqn. 5.2.3 after spontaneous breaking of electroweak symmetry, with the identification $f_2 \equiv \left(\sin^2\theta_W f_{WW} + \cos^2\theta_W f_{BB}\right)/\sqrt{2}$ and $f_1 \equiv f_B\sin\theta_W$.

Unlike the case of sec. 6.2.1, the energy distribution of the primary decay products in this case depends on the lorentz structure of the matrix element itself (see appendix A.3.2). We have considered three-body decays [4] into bosonic final states $\phi_2 \to \phi_1 W^+W^-, \phi_1 ZZ, \phi_1 Z\gamma, \phi_1\gamma\gamma$ as well as fermionic final states $\phi_2 \to \phi_1 b\bar{b}, \phi_1 t\bar{t}, \phi_1\tau^+\tau^-$ and the two-body decay $\phi_1 Z$ [5]. As in the case of single-component dark matter, here also we have also assumed that $f_{QQ} = f_{uu} = f_{dd} \equiv f_{qq}$ and $f_{l_L l_L} = f_{l_R l_R} \equiv f_{ll}$, for simplicity. In addition to the DM mass M_2 and the Wilson coefficient driving the decay under consideration, $\Delta M = M_2 - M_1$ is also a parameter that affects the γ-ray and radio signals. While determining the signals of ϕ_2 decay from various astrophysical objects we have assumed ϕ_2 density to be same as the DM density of that object *i.e.* $\rho_{\phi_2} = \rho_{\text{DM}}$. For $\rho_{\phi_2} < \rho_{\text{DM}}$ the results presented in sec. 6.4 get relaxed by a factor of $\rho_{\phi_2}/\rho_{\text{DM}}$.

6.3 Astrophysical signals of decaying DM

The heavier SM particles produced in DM decay leads to further cascades with either $e^\pm$ or π^0 as the end products. The $e^\pm$ undergo cycloidal motion in the galactic magnetic fields to produce observable radio signals while the π^0 mostly decay into photons in the gamma-ray energy range. Moreover, direct coupling of dark sector scalars to electroweak field strength tensors (i.e., $W^{\mu\nu}, B^{\mu\nu}$) directly produce gamma-ray photons.

---

[4]The four-body decays e.g. $\phi_2 \to \phi_1 h f\bar{f}, \phi_1 W^+W^-Z$ are sub-dominant compared to the three-body decays driven by the same operators due to phase space suppression and hence have been neglected in our analysis.

[5]Note that $\phi_2 \to \phi_1\gamma$ is suppressed from angular momentum conservation.

6.3.1 DM induced γ-ray flux

The differential γ-ray flux originating from the SM final states (e.g. $W^+W^-, ZZ, Z\gamma, \gamma\gamma, \bar{b}b,$ $\bar{t}t, \tau^+\tau^-$) of DM decay inside our galaxy, $\dfrac{d\Phi_{\mathrm{Gal}}}{dE_\gamma}(E_\gamma, \Omega)$, is given by eqn. 2.4.1. This differential distribution is calculated using [255]. We have considered $\rho_{\mathrm{DM}}(r)$ to be a standard Navarro-Frenk-White (NFW) profile [112] profile:

$$\rho_{\mathrm{DM}}(r) = \frac{\rho_0}{(r/r_s)\left(1 + r/r_s\right)^2} \tag{6.3.1}$$

where $r_s = 20\,\mathrm{kpc}$ and ρ_0 is such that the local DM density $\rho_{\mathrm{DM}}(r = 8.25\mathrm{kpc}) = 0.4$ GeV/cm^3 [256, 257].

On the other hand, DM decay inside of our galaxy also gives rise to $e^\pm$ which can transfer their energy to photons of CMB, dust scattered light and starlight via Inverse Compton Scatterings (ICS). The energy distribution of ICS gamma-rays are given by [117]:

$$\frac{d\Phi_{\mathrm{ICS}}}{dE_\gamma}(E_\gamma, \Omega) = \frac{1}{4\pi E_\gamma}\int_0^\infty ds \times 2 \int_{m_e}^{m_{\mathrm{DM}}/2} dE_e \mathcal{P}_{\mathrm{ICS}}(E_\gamma, E_e, \vec{r})\frac{dn_e}{dE_e}(E_e, \vec{r}) \tag{6.3.2}$$

where $\mathcal{P}_{\mathrm{ICS}}$ is the ICS power spectrum in Klein-Nishina regime which includes the distribution of photons in the inter-steller radiation field of CMB, dust scattered light and starlight [258]. On the other hand, $\dfrac{dn_e}{dE_e}(E_e, \vec{r})$ is the steady-state $e^\pm$ distribution obtained from the diffusion-loss equation:

$$\nabla\left[D(E_e, \vec{r})\nabla\left(\frac{dn_e}{dE_e}(E_e, \vec{r})\right)\right] + \frac{\partial}{\partial E}\left(b(E_e, \vec{r})\frac{dn_e}{dE_e}(E_e, \vec{r})\right) + Q(E_e, \vec{r}) = 0 \tag{6.3.3}$$

where $D(E_e, \vec{r})$ is the diffusion parameter which have been taken to be position independent for simplicity and we have used $D(E_e) = 3.33 \times 10^{27}\,\mathrm{cm}^2\,\mathrm{s}^{-1}\,(E_e/\mathrm{GeV})^{0.7}$ [259, 260]. The eqn 6.3.3 have been solved in a cylindrical diffusion zone of height of 8 kpc and radius 20 kpc [117]. For the energy-loss term $b(E_e, \vec{r})$ we have used the parametrization provided in [117]. The third term of eqn 6.3.3 is the source term:

$$Q(E_e, \vec{r}) = \frac{\rho_{\mathrm{DM}}(\vec{r}) \times \Gamma}{m_{\mathrm{DM}}}\sum_f \frac{dN_e^f}{dE_e}(E_e)B_f \tag{6.3.4}$$

where $\rho_{\mathrm{DM}}(\vec{r})$ is given in eqn 6.3.1 and $\dfrac{dN_e^f}{dE_e}(E_e)$ is the differential distribution of $e^\pm$ produced per DM decay in the final state f.

As for the galactic contribution to γ-rays from DM decay, the direction of observation (Ω) in eqns. 5.2.18 and 6.3.2 has been defined for the Fermi-LAT observation region $|b| \geq$
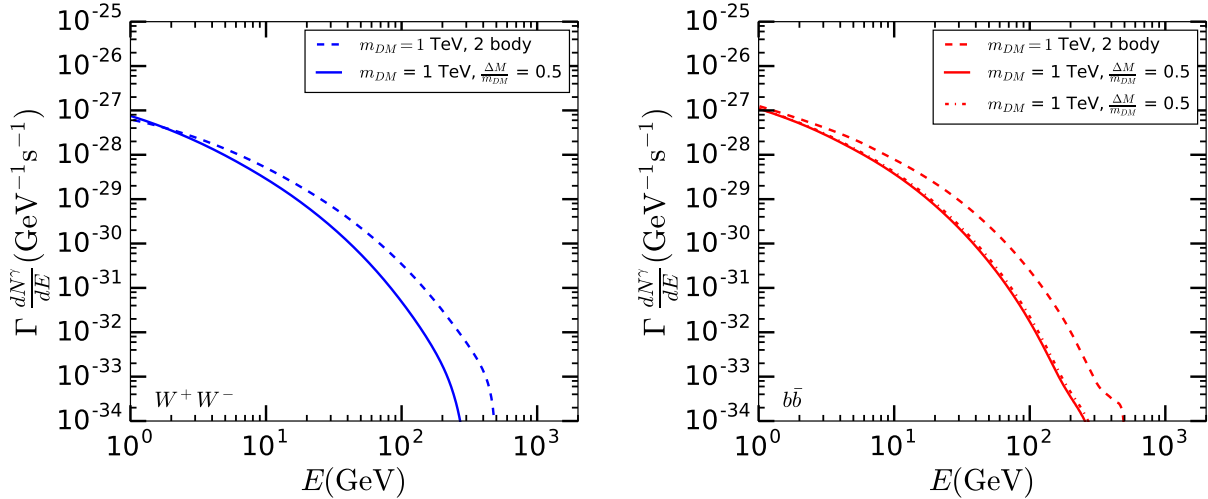
Figure 6.1: *Left panel:* γ-ray spectrum ($\Gamma\frac{dN^\gamma}{dE}$) for the decay processes $\phi \to W^+W^-$ (dashed curve) and $\phi_2 \to \phi_1 W^+W^-$ (solid curve). In the latter case, the (normalised) energy distribution of W^+/W^- is governed by Eqn. A.3.8. *Right panel:* γ-ray spectrum for the decay processes $\phi \to b\bar{b}$ (dashed curve) and $\phi_2 \to \phi_1 b\bar{b}$ (solid and dashed-dotted curves). For three-body decays the (normalised) energy distributions of $b/\bar{b}$ is governed by Eqns. A.3.13 (solid line) and A.3.14 (dashed-dotted line). Here $m_{DM} = 1$ TeV ($\frac{\Delta M}{m_{DM}} = 0.5$ for multicomponent scenario) and $\Gamma = 10^{-28}s^{-1}$.

20^0, $|l| \leq 180^0$ [220, 233], for which the astrophysical sources of isotropic gamma-rays are well resolved.

The gamma-rays originating from the DM decay outside of our galaxy also contributes to Fermi's measurement of IGRB. The extra-galactic contribution to the gamma-ray flux, $\frac{d\Phi_{\text{EG}}}{dE_\gamma}(E_\gamma)$, is as given in eqn. 2.4.2.

Thus the total γ-ray flux from DM decays,

$$\frac{d\Phi}{dE_\gamma} = \frac{d\Phi_{\text{Gal}}}{dE_\gamma} + \frac{d\Phi_{\text{ICS}}}{dE_\gamma} + \frac{d\Phi_{\text{EG}}}{dE_\gamma} \qquad (6.3.5)$$

which have been compared with the Fermi's result of IGRB [220] while deriving the limits presented in sec. 6.4. Having thus taken all contributions into account, it is found that for DM masses up to 300 GeV, $\Phi_{\text{Gal}} + \Phi_{\text{EG}}$ largely determines the limit, while Φ_{ICS} and Φ_{EG} play decisive roles for even higher masses. A caveat to be added here, however, is that ICS may become dominant if the DM directly decays into $e^\pm/\mu^\pm$ pairs, in contrast to the channels we have considered here. We refer the reader to [233] for details.

The galactic contribution to the total γ-ray flux in eqn 6.3.5 has been calculated following

[233] by taking the entire high-latitude sky for $|b| > 20^0$ into account. Note that this galactic contribution is not truly isotropic and can vary by a factor of 5 within the range of angles considered. Hence, if one takes the contribution towards anti-galactic center (i.e. $l = 180^0$) only (see [261, 262]), the total γ-ray flux can decrease at most by a factor of 5 and thus the limits on the dark matter decaywidth (presented in sec. 6.4) will also be weakened at most by the same factor. Since the decaywidth is proportional to the square of the Wilson coefficients, the corresponding limits on these coefficients will be relaxed maximally by a factor of ~ 2.2. This will widen the available DM parameter space that can be probed by future radio telescopes like SKA.

We have shown for illustration the γ-ray distributions ($\Gamma \frac{dN^\gamma}{dE_\gamma}$) originating from the decays $\phi \to W^+ W^-$ ($\phi \to b\bar{b}$) and $\phi_2 \to \phi_1 W^+ W^-$ ($\phi_2 \to \phi_1 b\bar{b}$) in the left (right) panel of Fig 6.1 for a benchmark value of m_{DM}, Γ and $\Delta M/m_{DM}$. Clearly for the three-body decays a substantial energy is taken away by ϕ_1, thereby softening the corresponding γ-ray spectrum.

6.3.2 DM induced radio flux

The SM products of DM decay inside a dSph generate $e^\pm$ pairs through cascade decays, whose abundance is decided by the source function $Q_e(E, r)$ [231] given in eqn. 6.3.4. The differential distribution is again obtained using [255]. As already mentioned, we have taken the dSph Draco as the target assuming a NFW profile as given in eqn. 6.3.1 with $\rho_0 = 1.4$ GeV. cm^{-3} and $r_s = 1.0$ kpc [263] [6]. We have used Draco for predicting the radio signal as various relevant parameters like the J-factor are somewhat better constrained for this dSph [265]. However, these parameters are also well-measured for other dSph's such as Seg1, Carina, Fornax, Sculptor etc [265–267]. Draco is used for illustration in our analysis.

The produced electron (positron) diffuses through the galactic medium and loses energy via several processes like Inverse-Compton scatterings (IC), Synchrotron radiation (Synch), Coulomb effect, bremsstrahlung etc. The final $e^\pm$ distribution $\frac{dn_e}{dE}(E, r)$ is obtained by solving the differential equation 6.3.3 [263, 268, 269], under the assumption that both the diffusion coefficient and energy-loss term are spatially invariant. Thus the diffusion parameter is parametrized as $D(E) = D_0 \left(\frac{E}{\text{GeV}} \right)^{0.3}$ and the radius of the diffusion zone is assumed to be 2.5 kpc [263]. The energy loss coefficient $b(E)$ is parametrized following [268–270].

The final radio flux (S_ν) as a function of frequency (ν) is obtained by folding this $\frac{dn_e}{dE}$

---

[6]We have checked that, the choice of other profiles such as Burkert [115,263] or Diemand et al. (2005) [264] (hereafter D05) [263] keep the observed radio flux almost similar.
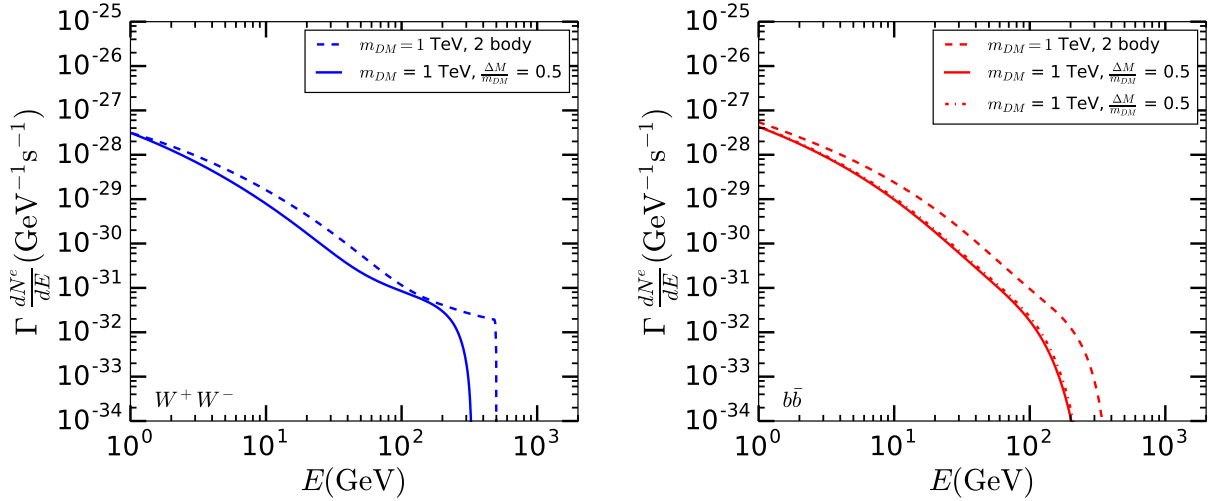
Figure 6.2: *Left panel:* $e^\pm$ spectrum ($\Gamma \frac{dN^e}{dE}$) for the decay processes $\phi \to W^+W^-$ (dashed curve) and $\phi_2 \to \phi_1 W^+W^-$ (solid curve). In the later case, the (normalised) energy distribution of W^+/W^- is governed by Eqn. A.3.8. *Right panel:* $e^\pm$ spectrum for the decay processes $\phi \to b\bar{b}$ (dashed curve) and $\phi_2 \to \phi_1 b\bar{b}$ (solid and dashed-dotted curves). For three-body decays the (normalised) energy distributions of $b/\bar{b}$ is governed by Eqns. A.3.13 (solid line) and A.3.14 (dashed-dotted line). Here $m_{DM} = 1$ TeV ($\frac{\Delta M}{m_{DM}} = 0.5$ for multicomponent scenario) and $\Gamma = 10^{-28} s^{-1}$.

with synchrotron power spectrum ($P_{Synch}(\nu, E, B)$) [250, 263, 268, 269] and integrating over the size of the emission region of the dSph ($\Delta\Omega$):

$$S_\nu(\nu) = \frac{1}{4\pi} \int_{\Delta\Omega} d\Omega \int_0^\infty ds \left(2 \int_{m_e}^{m_{DM}/2} dE \frac{dn_e}{dE}(r(s,\Omega), E) P_{Synch}(\nu, E, B) \right). \qquad (6.3.6)$$

As an example we have shown the $e^\pm$ distribution ($\Gamma \frac{dN^e}{dE}$) produced in the decays $\phi \to W^+W^-$ ($\phi \to b\bar{b}$) and $\phi_2 \to \phi_1 W^+W^-$ ($\phi_2 \to \phi_1 b\bar{b}$) in the left (right) panel of Fig. 6.2 for a benchmark value of $m_{DM}, \Gamma, \Delta M/m_{DM}$. The energy distributions are softer for three-body decays, as in the case of γ-rays. Fig. 6.3 encapsulates the resulting synchrotron fluxes ($S_\nu(\nu)$) where the values of the diffusion coefficient(D_0) and magnetic field(B) have been chosen to be $D_0 = 3 \times 10^{28} \text{cm}^2 \text{s}^{-1}$ and $B = 1$ μG, for illustration [263, 271].
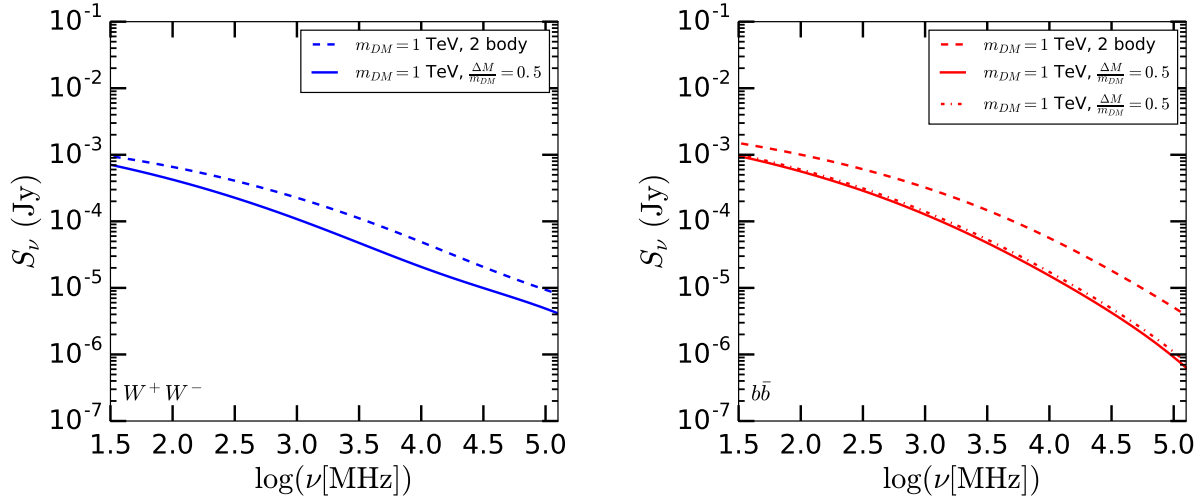
Figure 6.3: *Left panel:* Radio synchrotron flux, $S_\nu(\nu)$ (in Jy) for the decay processes $\phi \to W^+W^-$ (dashed curve) and $\phi_2 \to \phi_1 W^+W^-$ (solid curve). In the later case, the (normalised) energy distribution of W^+/W^- is governed by Eqn. A.3.8. *Right panel:* Synchrotron flux for the decay processes $\phi \to b\bar{b}$ (dashed curve) and $\phi_2 \to \phi_1 b\bar{b}$ (solid and dashed-dotted curves). For three-body decays the (normalised) energy distributions of $b/\bar{b}$ is governed by Eqns. A.3.13 (solid line) and A.3.14 (dashed-dotted line). Here $m_{DM} = 1$ TeV ($\frac{\Delta M}{m_{DM}} = 0.5$ for multicomponent scenario) and $\Gamma = 10^{-28}s^{-1}$. Choice of astrophysical parameters are $D_0 = 3 \times 10^{28}\text{cm}^2\text{s}^{-1}$ and $B = 1 \ \mu G$.

6.4 Results

Using Fermi-LAT observation of isotropic gamma-ray background (IGRB) [220] we start by showing illustrative upper limits on the DM decaywidth Γ, considering only a single decay channel at a time (i) for a given dark matter mass (m_{DM}) in case of two-body decays of DM itself and (ii) for a chosen dark matter mass (m_{DM}) and two fixed values of $\Delta M/m_{DM}$, namely 0.9 (*'hierarchical scenario'*) and 0.1 (*'degenerate scenario'*) in case of three-body decays occurring within a multicomponent scalar dark sector. We have subsequently presented the upper limits on the Wilson coefficients in Eqns. 6.2.3 and 6.2.5 considering only one effective operator at a time. This is a reasonable assumption since each operator presented here is independently gauge invariant. We have thus taken into account in the ultimate analysis all the decay channels opened up by a particular operator. The upper limits have been determined following the procedure of [233].

In each of the above cases we have also presented the sensitivity reach of the upcoming

109

Square Kilometer Array (SKA) assuming some benchmark values of the diffusion coefficient and the magnetic field, namely, $D_0 = 3 \times 10^{28} \mathrm{cm}^2 \mathrm{s}^{-1}$ and $B = 1\ \mu G$. However, these astrophysical parameters are not very well constrained yet for a dSph [232, 272]. Though the proximity to our galaxy suggests that $B \approx 1\ \mu G$ is a reasonable possibility [272], similar guidelines regarding D_0 hardly exists.

6.4.1 Decay to Gauge bosons

Fig. 6.4 shows the upper limits on the DM decaywidths (Γ) from Fermi-LAT observations as well as the sensitivity reach of the SKA in the channels W^+W^- (upper panel, left), ZZ (upper panel, right), $Z\gamma$ (lower panel, left) and $\gamma\gamma$ (lower panel, right). We have assumed 100% branching ratio to each of these decay modes. It is important to point out that the decays of DM (or dark sector particles) to $Z\gamma$ and $\gamma\gamma$ are associated with primary (direct) photons. Since Fermi-LAT is mostly sensitive to photons in the energy range *a few* MeV-1 TeV and the direct photons produced in the $Z\gamma$ and $\gamma\gamma$ final states for $m_{DM} > 1\,\mathrm{TeV}$ fall outside the energy range of Fermi-LAT, the corresponding limits weakens [220]. The future generation gamma-ray experiment like CTA [273, 274] can improve over Fermi-LAT in this range of parameters. We have adopted the strategy outlined in [211] to calculate sensitivity reach of CTA in the channels $Z\gamma$ and $\gamma\gamma$, which will show up as *sharp spectral features* on top of otherwise isotropic background flux of electrons+gamma-rays. The sensitivity reach of SKA in each of the cases have been shown which is nearly 4 to 2 orders of magnitude stronger depending on the DM mass m_{DM} barring the $\gamma\gamma$ final state. In case of the $\gamma\gamma$ final state the primary (off-shell) photons can split into e^+e^- pairs or other SM particle pairs which subsequently generate SKA-detectable radio signal [7]. Since this splitting is suppressed by α_{EM}, the SKA sensitivity can be stronger by 2 to 1 order of magnitude only (see fig. 6.4 bottom panel, right). Better sensitivity of SKA is mostly attributed to its large cross-sectional area and low threshold [249]. Of course, it also depends on the choice of astrophysical parameters (B, D_0). In our case we have assumed that $D_0 = 3 \times 10^{28} \mathrm{cm}^2 \mathrm{s}^{-1}$ and $B = 1\ \mu G$ which are reasonable choices for dSph such as Draco. A more conservative choice, i.e, a larger D_0 or a lower B will raise the sensitivity level.

The limits and sensitivities for the two-body decays $\phi \to VV'$ is the strongest one since the final state VV' has the energy m_{DM} available to them in these cases. For the three-body decays $\phi_2 \to \phi_1 VV'$, on the other hand, even if one neglects the energy carried away by ϕ_1

---

[7]The $e^\pm$ spectrum that originates from the splitting of a virtual primary photon (in $\gamma\gamma$ and γZ final states) has been calculated using the tools provided in [117].

the energy available to VV' is $\approx \Delta M < m_{DM}$. Thus the energy distribution of the final state photons or $e^{\pm}$ softens for the three-body decays (see Fig.6.1 and 6.2). This explains why the limits weakens for three-body decays as compared to two-body decays and also by at least an order of magnitude in case of $\Delta M/m_{DM} = 0.1$ compared to $\Delta M/m_{DM} = 0.9$. The (normalised) energy distribution of V/V', produced in the decay $\phi_2 \rightarrow \phi_1 VV'$, is governed by the Eqn. A.3.8.

In Fig. 6.5 we have shown the constraints obtained from Fermi-LAT and the sensitivity reach expected from SKA for gauge invariant wilson coefficients f_{WW}, f_{BB} considering $\Lambda = 10^{16}$ GeV for illustration. The operator proportional to f_{WW} opens up all the channels $W^+ W^-, ZZ, Z\gamma, \gamma\gamma$ while f_{BB} opens up $ZZ, Z\gamma, \gamma\gamma$ (see Eqns. A.3.3 and A.3.9). Thus in order to calculate limits on those parameters one needs to consider contribution from all the channels with appropriate branching fractions. As mentioned earlier, for channels such as $Z\gamma$ and $\gamma\gamma$ (which have direct photon(s) in their final states), both Fermi-LAT limit (mainly for lower DM mass) and CTA limit (mainly for higher DM mass) have been used. One should note that $\gamma\gamma$ channel has a branching ratio proportional to $\cos^4 \theta_W$ when f_{BB} is open compared to the $\sin^4 \theta_W$ dependence, when f_{WW} is open and thus the limit on f_{BB} is affected more by the inclusion of the sensitivity reach of CTA. This understanding is reflected in the kink around the energy, beyond which CTA offers a better probe for direct photons than Fermi-LAT. We have also shown the limits on the wilson coefficient f_B. The operator proportional to f_B gives only a two-body decay $\phi_2 \rightarrow \phi_1 Z$ (see the discussions regarding Eqn. A.3.10).

6.4.2 Decay to Fermions

In Fig. 6.6 we have shown the upper limits (for Fermi-LAT) and sensitivity (for SKA) on the decaywidth (Γ) as a function of m_{DM} assuming the decay occurs dominantly through $b\bar{b}$ (upper panel, left), $t\bar{t}$ (upper panel, right) and $\tau^+ \tau^-$ (lower panel). The (normalised) energy distribution of a fermion(f)/anti-fermion($\bar{f}$) produced in the three-body decay $\phi_2 \rightarrow \phi_1 f\bar{f}$ is considered to be the one governed by Eqn. A.3.13. One can check that the other energy distribution provided in Eqn. A.3.14 produces almost similar limits (and sensitivity) for any of the aforementioned fermionic channels, as expected from Figs. 6.1 and 6.2.

In Fig. 6.7 we have shown the constrains obtained from Fermi-LAT and the sensitivity reach expected from SKA on the wilson coefficient f_{qq} in case of the two-body decay of DM itself (upper left panel) and in case of decays in the dark sector (lower left panel). Here f_{qq} is the coupling to the quarks arising from $\mathcal{L}_{dim-5}^{\text{fermion},1}$ in Eqn. 6.2.3 and $\mathcal{L}_{dim-6}^{\text{fermion},1}$ in Eqn. 6.2.5,

respectively. For simplicity we have assumed that both the left and right handed quarks have the same values of this coupling. Also, we have considered that $f_{qq} \neq 0$ only for third generation of quarks which via gauge invariance dictates the relative contribution of the channels $b\bar{b}$ and $t\bar{t}$. It is quite evident that the limits from SKA on f_{qq} will be stronger than Fermi-LAT by more than one order of magnitude up to $m_{DM} \simeq 100 \, \mathrm{TeV}$ [8].

The upper right and lower right panel of the same figure shows the constraints on the wilson coefficient f_{ll} in case of the two-body decay of DM itself and in case of decays in the dark sector, respectively. Here also, we have assumed that both the left and right handed leptons have the same values of this coupling which appears only for the third generation of leptons. The only visible decay products as a result of switching on f_{ll} being $\tau^+\tau^-$ the limits on f_{ll} is straightforward to obtain from the decaywidths themselves. Although the sensitivity of SKA to $\tau^+\tau^-$ final states decreases rapidly as the m_{DM} increases (see the lower panel of Fig. 6.6) [9], SKA can still probe larger parameter space compared to Fermi-LAT even up to $m_{DM} \simeq 100$ TeV.

Fig. 6.8 shows the constrains obtained from Fermi-LAT and the sensitivity reach expected from SKA on the wilson coefficients f_{bbH}, f_{ttH} and f_{llH} in case of the two-body decay of DM itself (left column) and in case of decays in the dark sector (right column), respectively. Here f_{bbH}, f_{ttH} and f_{llH} are the couplings to the b and t quarks and τ lepton following from $\mathcal{L}_{dim-5}^{\mathrm{fermion,2}}$ in Eqn. 6.2.3 and $\mathcal{L}_{dim-6}^{\mathrm{fermion,2}}$ in Eqn. 6.2.5. For simplicity, we have considered the couplings to be non-zero only for the third generation of fermions. It is clear that the limits expected from 500 hours of observation at SKA on f_{bbH} and f_{ttH} will be stronger than Fermi-LAT by more than one order of magnitude up to $m_{DM} \simeq 100 \, \mathrm{TeV}$. Although the sensitivity of SKA to the $\tau^+\tau^-$ channel decreases rapidly as m_{DM} increases (see the lower panel of Fig. 6.6), SKA can still probe larger parameter space compared to Fermi-LAT even up to $m_{DM} \simeq 100$ TeV.

---

[8]It may be noted that DM decay takes place via higher dimensional operators with a large suppression scale. Thus one does not expect any unitarity bounds on the mass of decaying DM. On the other hand, such bounds may restrict m_{DM} to be less than few tens of TeV from the viewpoint of annihilations [275], on which we have not entered into a discussion here.

[9]In case of $\tau^+\tau^-$ channel one mostly has high energy $e^{\pm}$ which give rise to a synchrotron flux peaking towards higher frequencies. Thus for heavier DM masses only the lower frequency part of the radio flux (which is suppressed) contributes to SKA observation and consequently sensitivity decreases with increasing m_{DM} (See [250] for more details).

6.5 Conclusion

We have carried out a study of long-lived DM with its decay showing up in γ-ray as well as radio telescope observations. In order to comply with constraints on DM lifetime, the decay interactions have been parameterised by higher-dimensional operators. Both two-body decays of a scalar DM particle and three-body decays of quasi-stable particles within a dark sector have been considered, the SM particles among decay products being pairs of gauge bosons as well as fermions of the third family.

Constraints on the coefficients of the various operators have been obtained from existing γ-ray observations. The Fermi-LAT results are found to be most constraining in this respect. In comparison, the proposed CTA observations are found to yield weaker constraints, except in cases where at least one γ-ray photon is directly produced in the decay of a trans-TeV DM, as opposed to photons coming via cascades.

However, radio synchrotron signals from dSphs are found to provide better probes for DM decays, by enabling exploration of regions which cannot be ruled out by either the Fermi-LAT data or the CTA. This is true even for DM masses well-above a TeV. Using as benchmark 500 hours of observation at the upcoming SKA radio telescope, we find such a conclusion to hold for DM masses ranging up to tens of TeV.
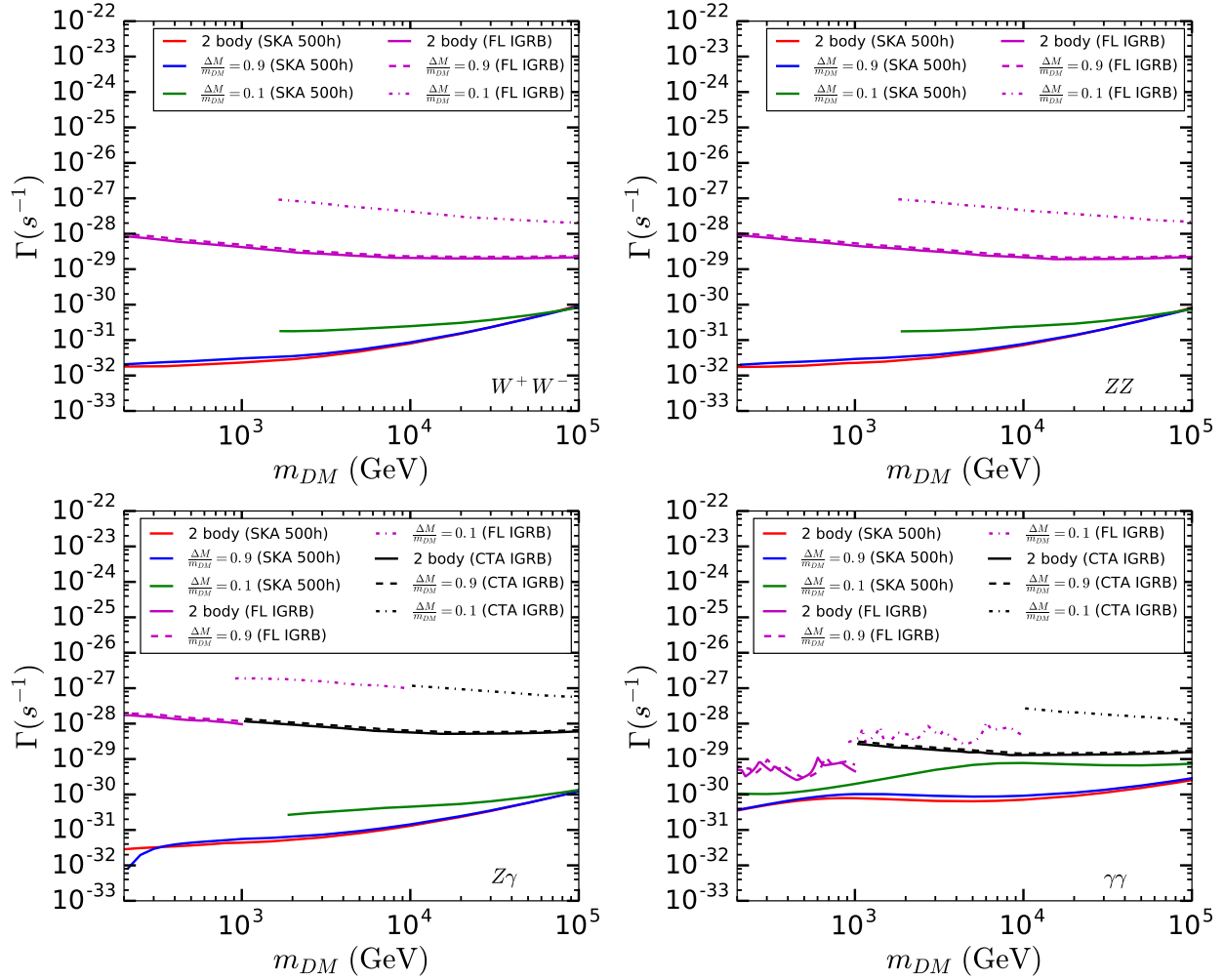
Figure 6.4: SKA sensitivity and the upper limit from γ-ray observation in the $\Gamma - m_{DM}$ plane for the decay of a DM (or a dark sector) particle of mass m_{DM} to various vector boson final states (VV'), i.e. either W^+W^- (upper-left panel) or ZZ (upper-right panel) or $Z\gamma$ (lower-left panel) or $\gamma\gamma$ (lower-right panel). The red, blue and green curves denote the required values of Γ to detect the radio fluxes at SKA (assuming a 500 hours of observation) from Draco dSph for the processes $\phi \to VV'$ and $\phi_2 \to \phi_1 VV'$ (with $\frac{\Delta M}{m_{DM}} = 0.9$ and 0.1), respectively. The (normalised) energy distribution of V/V' in three-body decay is governed by Eqn. A.3.8. The astrophysical parameters used are $D_0 = 3 \times 10^{28} \text{cm}^2 \text{s}^{-1}$ and $B = 1 \ \mu G$. The solid, dashed and dashed-dotted magenta lines are the corresponding upper limits on Γ from the observation of isotropic γ-ray background (IGRB) by Fermi-LAT (FL). In case of $Z\gamma$ and $\gamma\gamma$, along with Fermi-LAT, the projected sensitivity from the IGRB observation by CTA (black curves; assuming 500 hours of observation) also has been shown (see the text for details).
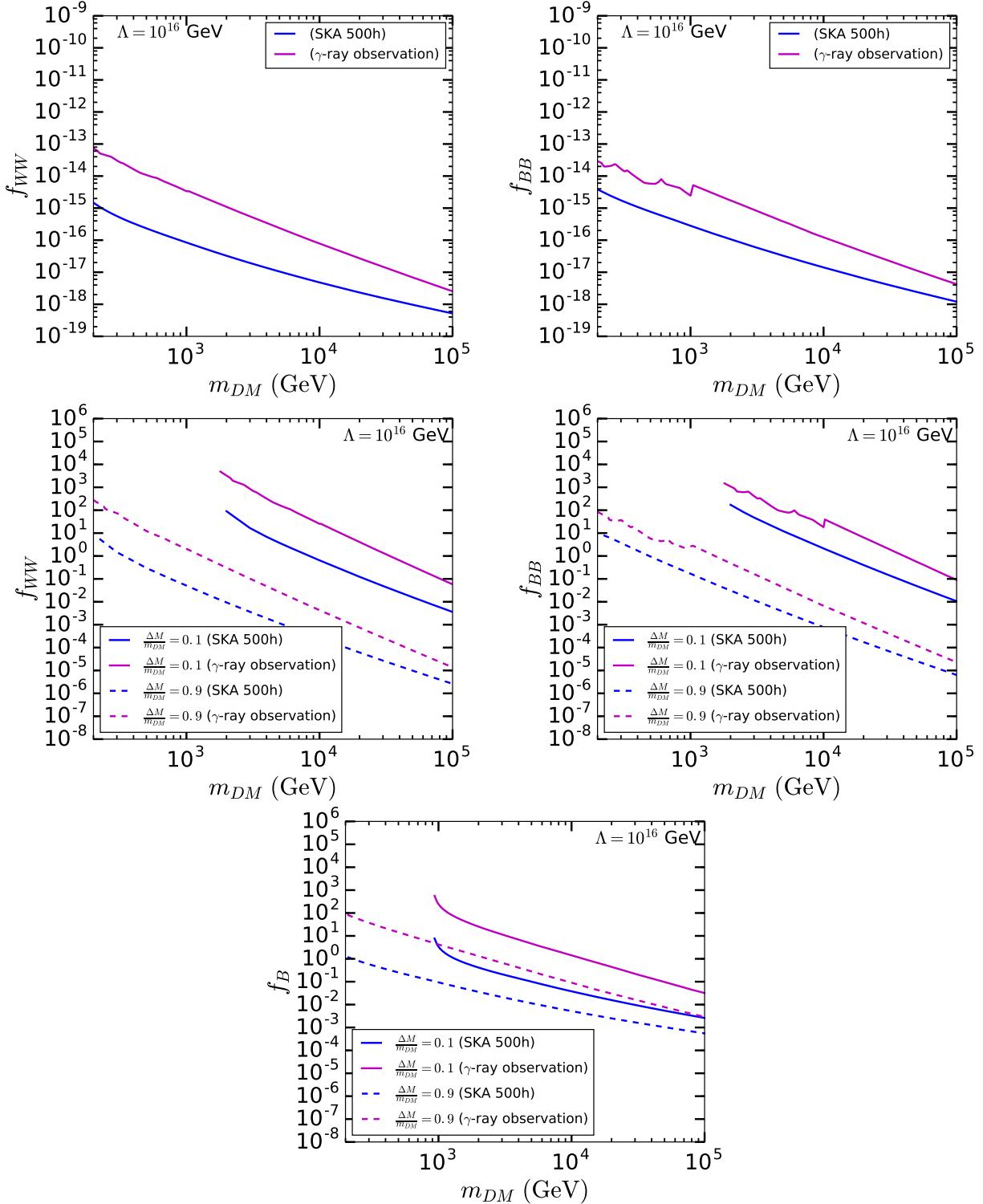
Figure 6.5: Sensitivity of SKA (blue) and corresponding limits from the IGRB observation (magenta) on the effective couplings f_{WW}, f_{BB} and f_B, for for two-body decays (*Upper panel*) and three-body decays (*Middle and Lower panels*) assuming $D_0 = 3 \times 10^{28} \text{cm}^2\text{s}^{-1}$ and $B = 1$ μG. For three-body decays we have taken $\Delta M/m_{DM} = 0.1$ (solid) and 0.9 (dashed).
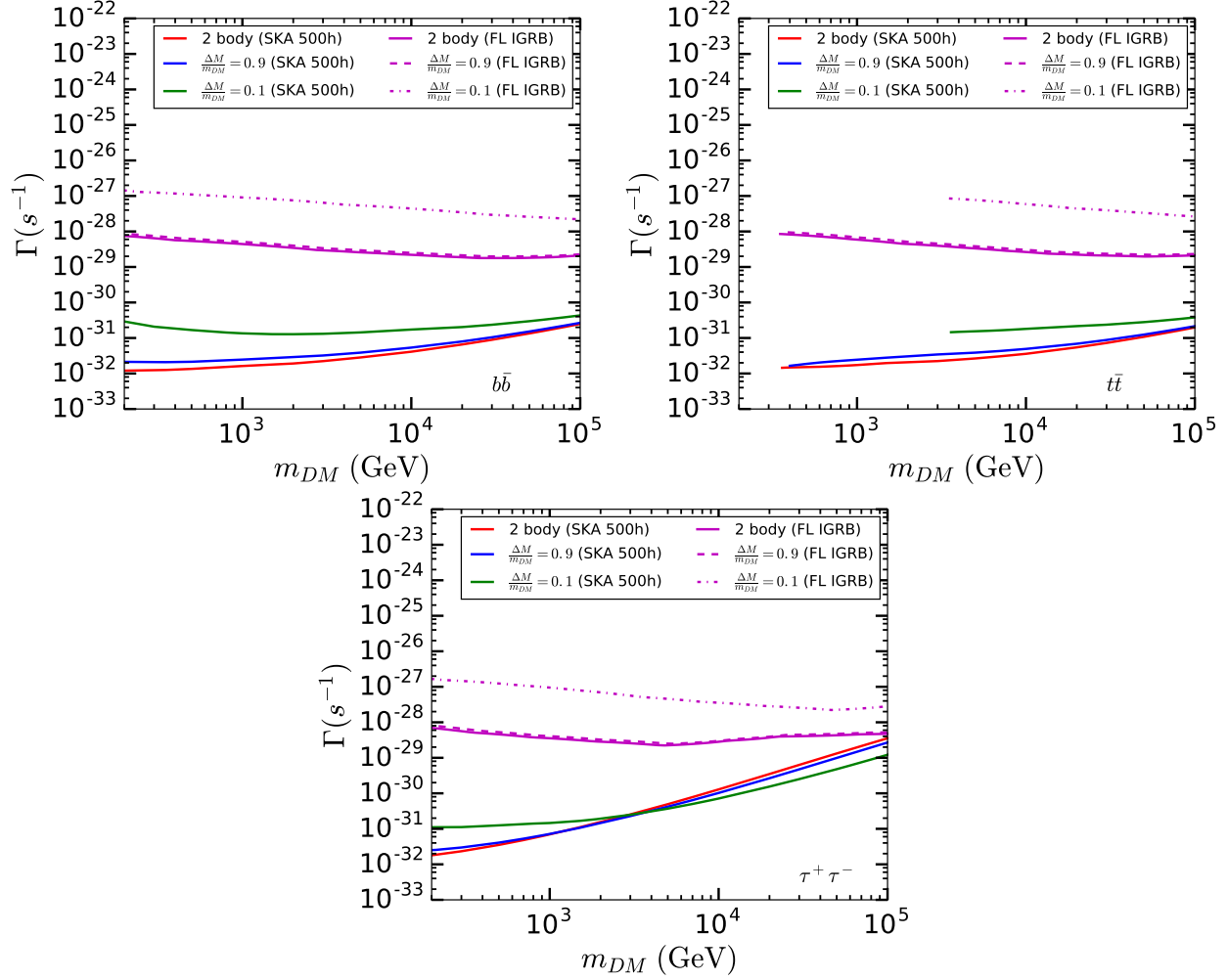
Figure 6.6: SKA sensitivity and the upper limit from γ-ray observation in the $\Gamma - m_{DM}$ plane for the decay of a DM (or a dark sector) particle of mass m_{DM} to various fermionic final states $(f\bar{f})$, i.e. either $b\bar{b}$ (upper-left panel) or $t\bar{t}$ (upper-right panel) or $\tau^+\tau^-$ (lower panel). The red, blue and green curves denote the required values of Γ to detect the radio fluxes from Draco dSph for the processes $\phi \to f\bar{f}$ and $\phi_2 \to \phi_1 f\bar{f}$ (with $\frac{\Delta M}{m_{DM}} = 0.9$ and 0.1), respectively. The (normalised) energy distribution of $f/\bar{f}$ in three-body decay is governed by Eqn. A.3.13. The astrophysical parameters used are $D_0 = 3 \times 10^{28} \mathrm{cm^2 s^{-1}}$ and $B = 1$ μG. The solid, dashed and dashed-dotted magenta lines are the corresponding upper limits on Γ from the observation of isotropic γ-ray background (IGRB) by Fermi-LAT (FL).

Figure 6.7: *Upper panel:* Sensitivity of SKA (blue lines; assuming a 500 hours observation for Draco dSph) to the effective couplings of $\mathcal{L}_{dim-5}^{\text{fermion},1}$, shown in Eqn. 6.2.3, which give the two-body decays of a DM particle of mass m_{DM} to the pairs of fermions. f_{qq} is the coupling to both b and t quarks and f_{ll} is the coupling to τ lepton. The astrophysical parameters used are $D_0 = 3 \times 10^{28} \text{cm}^2 \text{s}^{-1}$ and $B = 1~\mu G$. The magenta lines are the corresponding limits obtained from the isotropic γ-ray background (IGRB) observation. *Lower panel:* Similar constraints on the effective couplings of $\mathcal{L}_{dim-6}^{\text{fermion},1}$, shown in Eqn. 6.2.5, which give the three-body decays of a DM particle of mass m_{DM}. Two different values of $\Delta M/m_{DM}$ have been considered, $\Delta M/m_{DM} = 0.1$ (solid lines) and 0.9 (dashed lines).
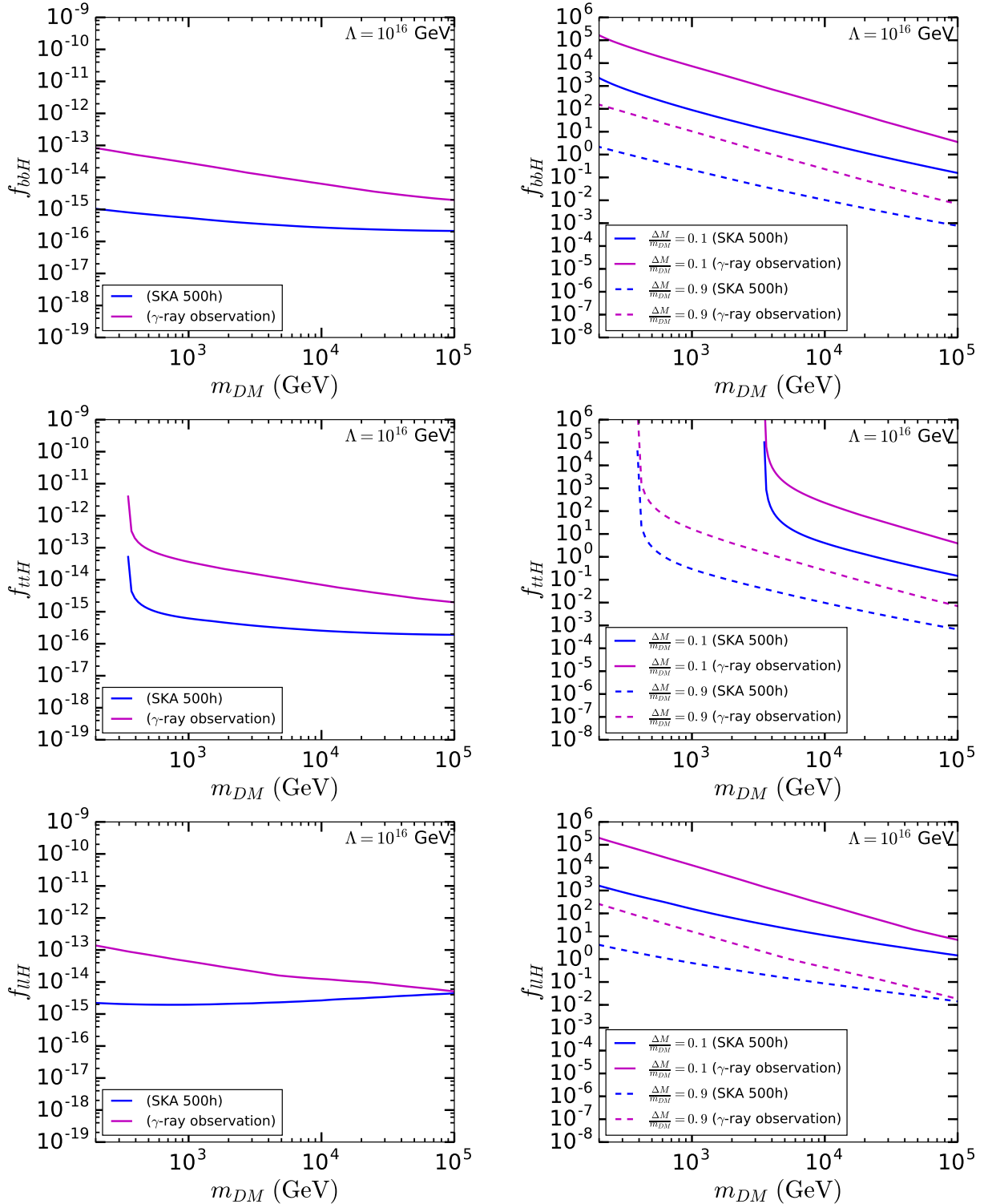
Figure 6.8: Sensitivity of SKA (blue) and corresponding limits from IGRB observations (magenta) on the effective couplings f_{bbH}, f_{ttH} and f_{llH}, for two-body decays (*Left column*) and three-body decays (*Right column*) assuming $D_0 = 3 \times 10^{28} \text{cm}^2\text{s}^{-1}$ and $B = 1 \ \mu G$. For three-body decays we have taken $\Delta M/m_{DM} = 0.1$ (solid) and 0.9 (dashed).

Chapter 7

Conclusions

In this thesis, we have dealt with a few theoretical frameworks containing DM where DM-visible sector interactions are rather suppressed. Such tiny interactions are achieved by parameterizing the DM-visible particle vertices either in terms of effective operators generated at a high-scale or '*technically natural*' minuscule renormalizable couplings. Although, these DM particles are unlikely to produce the trademark signatures of WIMPs in direct, indirect or collider search experiments, presence of heavier states in the dark sector may open up possibilities for new signals. Specifically, next-to-lightest dark sector particles appearing as HSCPs inside LHC as well as astrophysical signals originating from decays within a dark sector have been considered. In addition, implications for decaying DM, in the context of gamma-ray and radio observations have also been explored. Our findings are briefly summarized as follows :

- In chapter 3 we have studied two BSM scenarios of fermionic FIMPs, stabilized by an imposed Z_2 symmetry where the roles of the next-to-lightest Z_2-odd particles (NLOP) are played by the charged component of a $SU(2)_L$-triplet fermion and the charged scalar belonging to a $SU(2)_L$-doublet, respectively. In both the scenarios, the parameter regions consistent with freeze-in relic density of the DM as well as light-element abundances suggested by BBN require the NLOPs to behave as HSCPs, decaying outside the collider detectors. Each of these models predict two distinct kinds of signals involving the HSCPs, the discovery potential of which are investigated in the 14 TeV run of LHC and was found that for an integrated luminosity of 3000 fb^{-1} the fermionic (scalar) HSCP can be probed up to $\sim 1.2\,\mathrm{TeV}$ ($\sim 800\,\mathrm{GeV}$).

- Right-handed sneutrino LSP in the context of the MSSM extended with three gener-

ations of righ-handed neutrino superfields, with only Dirac masses for the neutrinos have been assumed in chapter 4. In such scenarios, decay of a dominantly right-chiral stau NLSP to the sneutrino LSP is very slow pertaining to the smallness of the neutrino Yukawa coupling, leading to long-lived charged tracks within LHC. We have used Drell-Yan production of $\tilde{l}_R$ followed by its decay $\tilde{l}_R \to \tilde{\tau}_1 \tau l$, to determine right-slepton masses and hence discriminate between two different mass orderings between $\tilde{\chi}_1^0$ and $\tilde{l}_R$. We found that for the final state with a single identified τ-jet asymmetric M_{T2} variable can be used to determine $\tilde{l}_R$ masses while collinear approximation works good for final states involving 2τ-jets.

- In chapter 5 we have considered a two-component Z_2-odd SM singlet scalar dark matter scenario where the heavier (ϕ_2) decays to the lighter (ϕ_1) in association with a pair of SM particles (i.e., e^-e^+, $\nu\bar{\nu}$, $\gamma\gamma$) at cosmological time scales. All dimension-4 as well as dimension-6 interaction terms governing such decays are taken into account and the corresponding effective couplings are expressed in terms of the parameters of a UV complete model where such dimension-6 interactions are generated at one-loop via the mediation of two heavy charged fermions. We have not only identified the parameter region where $\phi_2 \to \phi_1 \gamma\gamma$ is the dominant decay mode but also derived conservative constraints on the DM lifetime by using the observations of diffuse gamma-ray flux. Additionally, the case where one of the loop particles is a light SM fermion is also studied, a specific example of which is the right-handed sneutrino LSP in $\tilde{\nu}$MSSM.

- We have investigated in chapter 6 the astrophysical signals originating from the decay of a scalar DM and also that from a two-component scalar dark sector, by parameterizing all possible decays in terms of the effective operators which are consistent with SM gauge invariance as well as any existing symmetry of the dark sector. Each term of the effective lagrangian being gauge invariant on its own, we have assumed only one of them to be operative at a time and constrained the parameter space spanned by the corresponding Wilson coefficient and the decaying DM mass by analyzing the resulting astrophysical signals. While studying the gamma-ray signals from such decays we found that the Fermi-LAT observation of IGRB provides the strongest constraints in almost all the cases, except when photons are produced as the primary decay products with the DM mass exceeding a TeV, for which CTA has a better sensitivity. However, in all the cases, observations by the future radio telescope SKA will dig deeper into the DM parameter space for a wide range of DM masses.

Appendix A

Appendices

A.1 Mixing between charged fermions

In this appendix we illustrate how the charged component of the triplet fermion in our first model (with Z_2 odd fermion triplet and RH neutrino) can be made lighter than the neutral component. Let us introduce a vector-like SU(2) singlet charged fermion $\lambda_{L,R}$ and a triplet scalar Δ with $Y = 2$. If $\lambda_{L,R}$ is odd and Δ is even under the imposed Z_2 symmetry then the relevant part of the Lagrangian is

$$\mathcal{L} = M_\lambda \bar{\lambda}_L \lambda_R + Y_\lambda \, \mathrm{Tr} \left[\bar{\Sigma}^c_{3R} \, \Delta \, \lambda_R \right] + h.c, \tag{A.1.1}$$

where Σ_{3R} is defined in eqn. 3.2.1 and Δ is defined as

$$\Delta = \begin{bmatrix} \delta^+/\sqrt{2} & \delta^{++} \\ \delta^0 & -\delta^+/\sqrt{2}. \end{bmatrix} \tag{A.1.2}$$

Once the neutral component of the triplet scalar acquires a vev v_Δ the Yukawa term of the above Lagrangian will generate a mixing between $\lambda_{L,R}$ and $\Sigma_3^\pm$ and the charged fermion mass matrix will become

$$\mathcal{M}^\pm = \begin{bmatrix} M_\Sigma & v_\Delta Y_\lambda \\ v_\Delta Y_\lambda^\dagger & M_\lambda \end{bmatrix}, \tag{A.1.3}$$

where M_Σ is the mass of the fermion triplet as given in eqn. 3.2.2 and Y_λ is taken to be real for simplicity. The vev of the triplet scalar is restricted by the experimental observation of the ρ parameter and we assume $v_\Delta = 4$ GeV which is well within the current limit [276]. The eigenvalues of the mass matrix (eqn. A.1.1) will be

$$\frac{1}{2} \left[M_\Sigma + M_\lambda \pm \sqrt{(M_\Sigma - M_\lambda)^2 + 4 v_\Delta^2 \, Y_\lambda^2} \right]. \tag{A.1.4}$$

M_Σ (GeV) $\approx M_\psi$	M_λ (GeV)	Y_λ	Eigenvalues	
			Light(GeV) $\approx M_{\eta_3^\pm}$	Heavy (GeV)
850	2000	5	849.65	2000.35
	2500	5	849.76	2500.24
950	2000	5	949.62	2000.38
	2500	5	949.74	2500.26

Table A.1: Eigenvalues of the nearly degenerate charged and neutral fermions for few benchmark points after mixing between the triplet fermion and vector-like heavy charged fermion.

From the above equation it is evident that if $M_\lambda > M_\Sigma$ then the lightest state will be triplet dominant with a mass slightly smaller than M_Σ which for all practical purposes, can be identified as $\eta_3^\pm$. In Table. A.1 we have tabulated the exact eigenvalues for a few benchmark points. The masses of the triplet fermion M_Σ are kept at the same values as those used in our phenomenological analysis. We fix the illustrate Yukawa coupling to a value consistent with perturbativity. Evidently the mixing between charged fermions pulls down the mass of $\eta_3^\pm$ by about 250 MeV or more from M_Σ depending on the mass of the heavy vector-like fermion. This offsets the upward revision by appropriately 166 MeM via electromagnetic corrections, as given, for example in [21]. On the other hand, the neutral component of Σ_3 mixes only with the ν_s via tiny dimension-five operators and its mass will remain at M_Σ. Hence, the mass of $\eta_3^\pm$ remains below the neutral component mass for all the benchmark points shown in Table A.1.

A.2   Right-handed sneutrino as cold dark matter

The leading contributions to FIMP $\tilde{\nu}$ relic density stemming from the two-body decays of heavier superprticles are presented below:

$$\text{Higgsino}: \qquad \Gamma_{\tilde{H}_u^0 \to \tilde{\nu}\bar{\nu}_L} = \Gamma_{\tilde{H}_u^+ \to \tilde{\nu} l_L^+} = \frac{\beta^2\, y_\nu^2}{32\pi}\, \mu, \tag{A.2.1}$$

$$\text{Left} - \text{sneutrino}: \qquad \Gamma_{\tilde{\nu}_L \to \tilde{\nu} h} = \frac{\beta}{32\pi}\, \frac{A_\nu^2}{m_{\tilde{\nu}_L}}, \tag{A.2.2}$$

$$\Gamma_{\tilde{\nu}_L \to \tilde{\nu} Z} = \frac{\beta^3}{32\pi} \left[\frac{m_{\tilde{\nu}_L}^2}{m_{\tilde{\nu}_L}^2 - m_{\tilde{\nu}}^2}\right]^2 \frac{A_\nu^2}{m_{\tilde{\nu}_L}}, \tag{A.2.3}$$

$$\text{Left} - \text{slepton}: \qquad \Gamma_{\tilde{l}_L \to \tilde{\nu} W} = \frac{\beta^3}{32\pi} \left[\frac{m_{\tilde{l}_L}^2}{m_{\tilde{\nu}_L}^2 - m_{\tilde{\nu}}^2}\right]^2 \frac{A_\nu^2}{m_{\tilde{l}_L}}, \tag{A.2.4}$$

$$\text{Bino}: \qquad \Gamma_{\tilde{B} \to \tilde{\nu}\bar{\nu}_L} = \frac{\beta^2 g_Y^2}{64\pi} \left[\frac{A_\nu\, v}{m_{\tilde{\nu}_L}^2 - m_{\tilde{\nu}}^2}\right]^2 m_{\tilde{B}}, \tag{A.2.5}$$

$$\text{Wino}: \qquad \Gamma_{\tilde{W}^0 \to \tilde{\nu}\bar{\nu}_L} = \frac{\beta^2 g_W^2}{64\pi} \left[\frac{A_\nu\, v}{m_{\tilde{\nu}_L}^2 - m_{\tilde{\nu}}^2}\right]^2 m_{\tilde{W}}, \tag{A.2.6}$$

$$\Gamma_{\tilde{W}^+ \to \tilde{\nu} l_L^+} = \frac{\beta^2 g_W^2}{32\pi} \left[\frac{A_\nu\, v}{m_{\tilde{\nu}_L}^2 - m_{\tilde{\nu}}^2}\right]^2 m_{\tilde{W}}, \tag{A.2.7}$$

where $\beta = \left[1 - \dfrac{2(m_{\tilde{\nu}}^2 + m_y^2)}{m_x^2} + \dfrac{(m_{\tilde{\nu}}^2 - m_y^2)^2}{m_x^4 s}\right]^{1/2}$ for the decay $x \to \tilde{\nu}y$.

Therefore, freeze-in relic density of $\tilde{\nu}$ follows from eqn. 2.1.4 :

$$\Omega_{\tilde{\nu}}^{FI} h^2 = \frac{1.09 \times 10^{27}}{g_*^{3/2}} m_{\tilde{\nu}} \sum_i \frac{g_i \Gamma_i}{m_i^2}, \tag{A.2.8}$$

where i runs over all the superparticle species whose decay rates are shown in eqns. A.2.1-A.2.7.

A.3 Formulae for DM decays

A.3.1 Single-component dark matter

Decay to gauge bosons

The decay $\phi \to V V'$ is governed by the term

$$\frac{f_{VV'}}{\Lambda} \phi\, V_{\mu\nu} V'^{\mu\nu} \tag{A.3.1}$$

and the partial width is,

$$\begin{aligned}
\Gamma_{VV'} &= \frac{1}{2\pi} \left(\frac{f_{VV'}}{\Lambda}\right)^2 M^3 \sqrt{1 - \frac{2(m_V^2 + m_{V'}^2)}{M^2} + \frac{(m_V^2 - m_{V'}^2)^2}{M^4}} \\
&\quad \left[1 - \frac{2(m_V^2 + m_{V'}^2)}{M^2} + \frac{(m_V^4 + m_{V'}^4 + 4m_V^2 m_{V'}^2)}{M^4}\right].
\end{aligned} \tag{A.3.2}$$

Here,

$$f_{VV'} = \begin{cases}
f_{WW} & \text{for } V = W^+, V' = W^- \\
\dfrac{1}{\sqrt{2}} \left(\cos^2\theta_W f_{WW} + \sin^2\theta_W f_{BB}\right) & \text{for } V = Z, V' = Z \\
\cos\theta_W \sin\theta_W \left(f_{WW} - f_{BB}\right) & \text{for } V = Z, V' = \gamma \\
\dfrac{1}{\sqrt{2}} \left(\sin^2\theta_W f_{WW} + \cos^2\theta_W f_{BB}\right) & \text{for } V = \gamma, V' = \gamma
\end{cases} \tag{A.3.3}$$

Decay to fermions

The decay of ϕ to fermion pairs is parametrized as,

$$\frac{f_{ff}}{\Lambda} \phi \left(\bar{f}_L \gamma^\mu \partial_\mu f_L + \bar{f}_R \gamma^\mu \partial_\mu f_R\right) + \frac{f_{ffH}}{\Lambda} \phi \left[\bar{f}_L f_R H + h.c\right] \tag{A.3.4}$$

The decay width from the first term in Eqn. A.3.4,

$$\Gamma_{f\bar{f}} = N_c \frac{1}{8\pi} \left(\frac{f_{ff}}{\Lambda}\right)^2 m_f^2 M \left(1 - \frac{4m_f^2}{M^2}\right)^{3/2}. \tag{A.3.5}$$

and from the second term in Eqn. A.3.4,

$$\Gamma_{f\bar{f}} = N_c \frac{1}{16\pi} \left(\frac{f_{ffH}}{\Lambda}\right)^2 v^2 M \left(1 - \frac{4m_f^2}{M^2}\right)^{3/2}. \tag{A.3.6}$$

where $N_c = 3$ for quarks and $N_c = 1$ for leptons.

A.3.2 Multicomponent dark sector

Decay to gauge bosons

1. The decay $\phi_2 \to \phi_1 V V'$ is governed by

$$\frac{f_{VV'}}{\Lambda^2} \phi_2 \phi_1 V_{\mu\nu} V'^{\mu\nu} \tag{A.3.7}$$

The energy distribution of the vector boson V originating from $\phi_2 \to \phi_1 VV'$ is,

$$
\begin{aligned}
\frac{d\Gamma_{\phi_1 VV'}}{dx_v} &= \left(\frac{f_{VV'}}{\Lambda^2}\right)^2 \frac{M_2^5}{32\pi^3} \sqrt{x_v^2 - 4r_v^2}\, \lambda^{1/2}\left(\sqrt{1 + r_v^2 - x_v}\,,\, r_1,\, r_{v'}\right) \\
&\quad \left[2r_v^2 r_{v'}^2 + \frac{1}{12}\left\{3\frac{(x_v - 2r_v^2)^2}{(1 + r_v^2 - x_v)^2}(1 - r_1^2 + r_v^2 + r_{v'}^2 - x_v)^2 \right. \right.\\
&\quad \left. \left. + (x_v^2 - 4r_v^2)\lambda\left(\sqrt{1 + r_v^2 - x_v}\,,\, r_1,\, r_{v'}\right)\right\}\right]
\end{aligned}
\tag{A.3.8}
$$

where $r_{v(v')} = \dfrac{m_{v(v')}}{M_2}$, $r_1 = \dfrac{M_1}{M_2}$, $x_v = \dfrac{2E_v}{M_2}$ and $2\,r_v \leq x_v \leq (1 - r_1^2 + r_v^2 - r_{v'}^2 - 2r_1 r_{v'})$.

The kallen-lambda function is given by, $\lambda(a, b, c) = \left(1 - \dfrac{2(b^2 + c^2)}{a^2} + \dfrac{(b^2 - c^2)^2}{a^4}\right)$.

Here,

$$
f_{VV'} = \begin{cases}
f_{WW} & \text{for } V = W^+, V' = W^- \\
\dfrac{1}{\sqrt{2}}\left(\cos^2\theta_W f_{WW} + \sin^2\theta_W f_{BB}\right) & \text{for } V = Z, V' = Z \\
\cos\theta_W \sin\theta_W \left(f_{WW} - f_{BB}\right) & \text{for } V = Z, V' = \gamma \\
\dfrac{1}{\sqrt{2}}\left(\sin^2\theta_W f_{WW} + \cos^2\theta_W f_{BB}\right) & \text{for } V = \gamma, V' = \gamma
\end{cases}
\tag{A.3.9}
$$

2. Due to angular momentum conservation the decay $\phi_2 \to \phi_1\gamma$ is forbidden and the operator

$$\frac{f_B}{\Lambda^2}\left(\partial_\mu\phi_2\partial_\nu\phi_1 - \partial_\nu\phi_2\partial_\mu\phi_1\right)B_{\mu\nu} \tag{A.3.10}$$

can only trigger the decay $\phi_2 \to \phi_1 Z$.

The emitted Z-boson has a fixed energy $E_z = M_2/2\left(1 - r_1^2 + r_z^2\right)$ and the corresponding width is,

$$\Gamma_{\phi_1 Z} = \left(\frac{f_B}{\Lambda^2}\right)^2 M_2^3 \frac{\sin^2\theta_W m_z^2}{16\pi}\lambda^{3/2}\left(1, r_1, r_z\right) \tag{A.3.11}$$

Decay to fermions

The interactions are,

$$\frac{f_{ff}}{\Lambda^2}\phi_2\overset{\leftrightarrow}{\partial}_\mu\phi_1\,\bar{f}\gamma^\mu f + \frac{f_{ffH}}{\Lambda^2}\frac{v}{\sqrt{2}}\phi_2\phi_1\,\bar{f}f \tag{A.3.12}$$

For simplicity in our analysis we have taken only one operator at a time.

1. The differential distribution of the fermion due to first term of Eqn. A.3.12.

$$
\begin{aligned}
\frac{d\Gamma_{\phi_1 f\bar{f}}}{dx} &= N_c\left(\frac{f_{ff}}{\Lambda^2}\right)^2\frac{M_2^5}{16\,\pi^3}\Bigg[\sqrt{x^2-4\,r_f^2}\,\lambda^{1/2}\left(\sqrt{1+r_f^2-x},r_1,r_f\right)\\
&\quad \frac{2(1-r_1^2-x)(1+r_f^2-x)-(1-x)(2-x)(1-r_1^2+2r_f^2-x)}{\left(1+r_f^2-x\right)}\Bigg]
\end{aligned}
\tag{A.3.13}
$$

where $r_f=\dfrac{m_f}{M_2}, r_1=\dfrac{M_1}{M_2}$ and $x=\dfrac{2E_f}{M_2}$ with $2r_f\leq x\leq(1-r_1^2-2r_1r_f)$.

2. The differential energy distribution of the fermions for the second operator in Eqn. A.3.12 is,

$$
\begin{aligned}
\frac{d\Gamma_{\phi_1 f\bar{f}}}{dx} &= N_c\left(\frac{f_{ffH}}{\Lambda^2}\right)^2\frac{v^2 M_2^3}{512\pi^3}\Bigg[\sqrt{x^2-4\,r_f^2}\,\lambda^{1/2}\left(\sqrt{1+r_f^2-x},r_1,r_f\right)\\
&\quad \frac{x(1-r_1^2-x)+2r_f^2(-3+r_1^2+4x)-8r_f^4}{\left(1+r_f^2-x\right)}\Bigg]
\end{aligned}
\tag{A.3.14}
$$

where $r_f=\dfrac{m_f}{M_2}$, $r_1=\dfrac{M_1}{M_2}$, $x=\dfrac{2E_f}{M_2}$ and $2\,r_f\leq x\leq(1-r_1^2-2r_1r_f)$.

Here $N_c=3$ for quarks and $N_c=1$ for leptons.

Bibliography

[1] J. F. Donoghue, E. Golowich, and B. R. Holstein, *Dynamics of the standard model*, vol. 2. CUP, 2014.

[2] S. L. Glashow, *Partial Symmetries of Weak Interactions*, *Nucl. Phys.* **22** (1961) 579–588.

[3] S. Weinberg, *A Model of Leptons*, *Phys. Rev. Lett.* **19** (1967) 1264–1266.

[4] P. W. Higgs, *Broken symmetries, massless particles and gauge fields*, *Phys. Lett.* **12** (1964) 132–133.

[5] P. W. Higgs, *Broken Symmetries and the Masses of Gauge Bosons*, *Phys. Rev. Lett.* **13** (1964) 508–509.

[6] **CMS** Collaboration, S. Chatrchyan et al., *Observation of a New Boson at a Mass of 125 GeV with the CMS Experiment at the LHC*, *Phys. Lett. B* **716** (2012) 30–61, [arXiv:1207.7235].

[7] F. Zwicky, *On the Masses of Nebulae and of Clusters of Nebulae*, *Astrophys. J.* **86** (1937) 217–246.

[8] V. C. Rubin and W. K. Ford, Jr., *Rotation of the Andromeda Nebula from a Spectroscopic Survey of Emission Regions*, *Astrophys. J.* **159** (1970) 379–403.

[9] D. Clowe, M. Bradac, A. H. Gonzalez, M. Markevitch, S. W. Randall, C. Jones, and D. Zaritsky, *A direct empirical proof of the existence of dark matter*, *Astrophys. J. Lett.* **648** (2006) L109–L113, [astro-ph/0608407].

[10] **Planck** Collaboration, P. A. R. Ade et al., *Planck 2015 results. XIII. Cosmological parameters*, *Astron. Astrophys.* **594** (2016) A13, [arXiv:1502.01589].

[11] **BOSS** Collaboration, S. Alam et al., *The clustering of galaxies in the completed SDSS-III Baryon Oscillation Spectroscopic Survey: cosmological analysis of the DR12 galaxy sample*, *Mon. Not. Roy. Astron. Soc.* **470** (2017), no. 3 2617–2652, [arXiv:1607.03155].

[12] M. R. Lovell, C. S. Frenk, V. R. Eke, A. Jenkins, L. Gao, and T. Theuns, *The properties of warm dark matter haloes*, *Mon. Not. Roy. Astron. Soc.* **439** (2014) 300–317, [arXiv:1308.1399].

[13] R. Kennedy, C. Frenk, S. Cole, and A. Benson, *Constraining the warm dark matter particle mass with Milky Way satellites*, *Mon. Not. Roy. Astron. Soc.* **442** (2014), no. 3 2487–2495, [arXiv:1310.7739].

[14] G. Arcadi, M. Dutra, P. Ghosh, M. Lindner, Y. Mambrini, M. Pierre, S. Profumo, and F. S. Queiroz, *The waning of the WIMP? A review of models, searches, and constraints*, *Eur. Phys. J. C* **78** (2018), no. 3 203, [arXiv:1703.07364].

[15] G. Jungman, M. Kamionkowski, and K. Griest, *Supersymmetric dark matter*, *Phys. Rept.* **267** (1996) 195–373, [hep-ph/9506380].

[16] O. Lebedev, H. M. Lee, and Y. Mambrini, *Vector Higgs-portal dark matter and the invisible Higgs*, *Phys. Lett. B* **707** (2012) 570–576, [arXiv:1111.4482].

[17] O. Cata and A. Ibarra, *Dark Matter Stability without New Symmetries*, *Phys. Rev. D* **90** (2014), no. 6 063509, [arXiv:1404.0432].

[18] C. P. Burgess, M. Pospelov, and T. ter Veldhuis, *The Minimal model of nonbaryonic dark matter: A Singlet scalar*, *Nucl. Phys. B* **619** (2001) 709–728, [hep-ph/0011335].

[19] Y. G. Kim and K. Y. Lee, *The Minimal model of fermionic dark matter*, *Phys. Rev. D* **75** (2007) 115012, [hep-ph/0611069].

[20] A. De Simone, G. F. Giudice, and A. Strumia, *Benchmarks for Dark Matter Searches at the LHC*, *JHEP* **06** (2014) 081, [arXiv:1402.6287].

[21] M. Cirelli, N. Fornengo, and A. Strumia, *Minimal dark matter*, *Nucl. Phys. B* **753** (2006) 178–194, [hep-ph/0512090].

[22] M. Cirelli and A. Strumia, *Minimal Dark Matter: Model and results*, *New J. Phys.* **11** (2009) 105005, [arXiv:0903.3381].

[23] A. Chaudhuri, N. Khan, B. Mukhopadhyaya, and S. Rakshit, *Dark matter candidate in an extended type III seesaw scenario*, Phys. Rev. **D91** (2015) 055024, [arXiv:1501.05885].

[24] J. Bovy and S. Tremaine, *On the local dark matter density*, Astrophys. J. **756** (2012) 89, [arXiv:1205.4033].

[25] **XENON** Collaboration, E. Aprile et al., *Dark Matter Search Results from a One Ton-Year Exposure of XENON1T*, Phys. Rev. Lett. **121** (2018), no. 11 111302, [arXiv:1805.12562].

[26] **LUX** Collaboration, D. S. Akerib et al., *Results from a search for dark matter in the complete LUX exposure*, Phys. Rev. Lett. **118** (2017), no. 2 021303, [arXiv:1608.07648].

[27] **PandaX-II** Collaboration, X. Cui et al., *Dark Matter Results From 54-Ton-Day Exposure of PandaX-II Experiment*, Phys. Rev. Lett. **119** (2017), no. 18 181302, [arXiv:1708.06917].

[28] **DarkSide** Collaboration, P. Agnes et al., *Low-Mass Dark Matter Search with the DarkSide-50 Experiment*, Phys. Rev. Lett. **121** (2018), no. 8 081307, [arXiv:1802.06994].

[29] **CRESST** Collaboration, A. H. Abdelhameed et al., *First results from the CRESST-III low-mass dark matter program*, Phys. Rev. D **100** (2019), no. 10 102002, [arXiv:1904.00498].

[30] **PICO** Collaboration, C. Amole et al., *Dark Matter Search Results from the Complete Exposure of the PICO-60 C_3F_8 Bubble Chamber*, Phys. Rev. D **100** (2019), no. 2 022001, [arXiv:1902.04031].

[31] M. Schumann, *Direct Detection of WIMP Dark Matter: Concepts and Status*, J. Phys. G **46** (2019), no. 10 103003, [arXiv:1903.03026].

[32] **Fermi-LAT, DES** Collaboration, A. Albert et al., *Searching for Dark Matter Annihilation in Recently Discovered Milky Way Satellites with Fermi-LAT*, Astrophys. J. **834** (2017), no. 2 110, [arXiv:1611.03184].

[33] J. L. et al., *The integral experiment*, Nuclear Physics B - Proceedings Supplements **60** (1998), no. 3 69–79.

129

[34] **AGILE** Collaboration, M. Tavani et al., *The AGILE Mission*, Astron. Astrophys. **502** (2009) 995–1013, [arXiv:0807.4254].

[35] **H.E.S.S.** Collaboration, H. Abdallah et al., *Search for dark matter annihilations towards the inner Galactic halo from 10 years of observations with H.E.S.S*, Phys. Rev. Lett. **117** (2016), no. 11 111301, [arXiv:1607.08142].

[36] J. Holder et al., *VERITAS: Status and Highlights*, in *32nd International Cosmic Ray Conference*, 11, 2011. arXiv:1111.1225.

[37] J. Cortina, A. Armada, A. Biland, O. Blanch, M. Garczarczyk, F. Goebel, P. Majumdar, M. Mariotti, A. Moralejo, D. Paneque, R. Paoletti, and N. Turini, *Technical Performance of the MAGIC Telescope*, in *29th International Cosmic Ray Conference (ICRC29), Volume 5*, vol. 5 of *International Cosmic Ray Conference*, p. 359, Jan., 2005.

[38] O. Adriani et al., *Measurement of the flux of primary cosmic ray antiprotons with energies of 60-MeV to 350-GeV in the PAMELA experiment*, Pisma Zh. Eksp. Teor. Fiz. **96** (2012) 693–699.

[39] S.-J. Lin, X.-J. Bi, P.-F. Yin, and Z.-H. Yu, *Implications for dark matter annihilation from the AMS-02 $\bar{p}/p$ ratio*, arXiv:1504.07230.

[40] B.-Q. Lu and H.-S. Zong, *Limits on dark matter from AMS-02 antiproton and positron fraction data*, Phys. Rev. D **93** (2016), no. 10 103517, [arXiv:1510.04032].

[41] **CMS** Collaboration, A. M. Sirunyan et al., *Search for dark matter produced with an energetic jet or a hadronically decaying W or Z boson at $\sqrt{s} = 13$ TeV*, JHEP **07** (2017) 014, [arXiv:1703.01651].

[42] **CMS** Collaboration, *Search for dark matter in $Z + E_T^{\text{miss}}$ events using 12.9 fb^{-1} of 2016 data*, .

[43] **ATLAS** Collaboration, *Search for Dark Matter Produced in Association with a Higgs Boson decaying to $b\bar{b}$ at $\sqrt{s} = 13$ TeV with the ATLAS Detector using $79.8\,fb^{-1}$ of proton-proton collision data*, .

[44] **CMS** Collaboration, V. Khachatryan et al., *Searches for invisible decays of the Higgs boson in pp collisions at $\sqrt{s} = 7, 8,$ and 13 TeV*, JHEP **02** (2017) 135, [arXiv:1610.09218].

[45] **Particle Data Group** Collaboration, C. Patrignani et al., *Review of Particle Physics*, *Chin. Phys. C* **40** (2016), no. 10 100001.

[46] Y. Hochberg, E. Kuflik, T. Volansky, and J. G. Wacker, *Mechanism for Thermal Relic Dark Matter of Strongly Interacting Massive Particles*, *Phys. Rev. Lett.* **113** (2014) 171301, [arXiv:1402.5143].

[47] E. Kuflik, M. Perelstein, N. R.-L. Lorier, and Y.-D. Tsai, *Elastically Decoupling Dark Matter*, *Phys. Rev. Lett.* **116** (2016), no. 22 221302, [arXiv:1512.04545].

[48] L. J. Hall, K. Jedamzik, J. March-Russell, and S. M. West, *Freeze-In Production of FIMP Dark Matter*, *JHEP* **03** (2010) 080, [arXiv:0911.1120].

[49] **Fermi-LAT** Collaboration, M. Ackermann et al., *Searching for Dark Matter Annihilation from Milky Way Dwarf Spheroidal Galaxies with Six Years of Fermi Large Area Telescope Data*, *Phys. Rev. Lett.* **115** (2015), no. 23 231301, [arXiv:1503.02641].

[50] **ATLAS** Collaboration, *Search for new phenomena in events with jets and missing transverse momentum in p p collisions at $\sqrt{s}$ = 13 TeV with the ATLAS detector*, .

[51] **ATLAS** Collaboration, *Search for dark matter in association with an energetic photon in pp collisions at $s\sqrt{}$=13 TeV with the ATLAS detector*, .

[52] E. W. Kolb and M. S. Turner, *The Early Universe*, *Front. Phys.* **69** (1990) 1–547.

[53] J. L. Feng, A. Rajaraman, and F. Takayama, *Superweakly interacting massive particles*, *Phys. Rev. Lett.* **91** (2003) 011302, [hep-ph/0302215].

[54] G. Bélanger et al., *LHC-friendly minimal freeze-in models*, *JHEP* **02** (2019) 186, [arXiv:1811.05478].

[55] A. Biswas, S. Choubey, L. Covi, and S. Khan, *Explaining the 3.5 keV X-ray Line in a $L_\mu - L_\tau$ Extension of the Inert Doublet Model*, *JCAP* **1802** (2018), no. 02 002, [arXiv:1711.00553].

[56] J. Herms and A. Ibarra, *Probing multicomponent FIMP scenarios with gamma-ray telescopes*, *JCAP* **03** (2020) 026, [arXiv:1912.09458].

[57] G. Arcadi and L. Covi, *Minimal Decaying Dark Matter and the LHC*, *JCAP* **1308** (2013) 005, [arXiv:1305.6587].

[58] G. Arcadi, L. Covi, and F. Dradi, *LHC prospects for minimal decaying Dark Matter*, *JCAP* **1410** (2014), no. 10 063, [arXiv:1408.1005].

[59] M. Johansen, J. Edsjo, S. Hellman, and D. Milstead, *Long-lived stops in MSSM scenarios with a neutralino LSP*, *JHEP* **08** (2010) 005, [arXiv:1003.4540].

[60] A. V. Gladyshev, D. I. Kazakov, and M. G. Paucar, *Production of long-lived sleptons at LHC*, *Mod. Phys. Lett. A* **20** (2005) 3085–3094, [hep-ph/0509168].

[61] D. Choudhury, S. K. Gupta, and B. Mukhopadhyaya, *Right sneutrinos in a supergravity model and the signals of a stable stop at the Large Hadron Collider*, *Phys. Rev.* **D78** (2008) 015023, [arXiv:0804.3560].

[62] S. K. Gupta, B. Mukhopadhyaya, and S. K. Rai, *Right-chiral sneutrinos and long-lived staus: Event characteristics at the large hadron collider*, *Phys. Rev.* **D75** (2007) 075007, [hep-ph/0701063].

[63] J. L. Diaz-Cruz, J. R. Ellis, K. A. Olive, and Y. Santoso, *On the Feasibility of a Stop NLSP in Gravitino Dark Matter Scenarios*, *JHEP* **05** (2007) 003, [hep-ph/0701229].

[64] J. L. Feng, S. Su, and F. Takayama, *Supergravity with a gravitino LSP*, *Phys. Rev. D* **70** (2004) 075019, [hep-ph/0404231].

[65] A. G. Hessler, A. Ibarra, E. Molinaro, and S. Vogl, *Probing the scotogenic FIMP at the LHC*, *JHEP* **01** (2017) 100, [arXiv:1611.09540].

[66] **CMS** Collaboration, S. Chatrchyan et al., *Searches for long-lived charged particles in pp collisions at $\sqrt{s}$=7 and 8 TeV*, *JHEP* **07** (2013) 122, [arXiv:1305.0491].

[67] **ATLAS** Collaboration, G. Aad et al., *Searches for heavy long-lived charged particles with the ATLAS detector in proton-proton collisions at $\sqrt{s} = 8$ TeV*, *JHEP* **01** (2015) 068, [arXiv:1411.6795].

[68] **Particle Data Group** Collaboration, K. A. Olive et al., *Review of Particle Physics*, *Chin. Phys. C* **38** (2014) 090001.

[69] O. Cerri, S. Xie, C. Pena, and M. Spiropulu, *Identification of Long-lived Charged Particles using Time-Of-Flight Systems at the Upgraded LHC detectors*, *JHEP* **04** (2019) 037, [arXiv:1807.05453].

[70] K. Hamaguchi, Y. Kuno, T. Nakaya, and M. M. Nojiri, *A Study of late decaying charged particles at future colliders*, *Phys. Rev. D* **70** (2004) 115007, [hep-ph/0409248].

[71] K. Hamaguchi, M. M. Nojiri, and A. de Roeck, *Prospects to study a long-lived charged next lightest supersymmetric particle at the LHC*, *JHEP* **03** (2007) 046, [hep-ph/0612060].

[72] J. M. O'Meara, S. Burles, J. X. Prochaska, G. E. Prochter, R. A. Bernstein, and K. M. Burgess, *The Deuterium to Hydrogen Abundance Ratio Towards the QSO SDSS1558-0031*, *Astrophys. J. Lett.* **649** (2006) L61–L66, [astro-ph/0608302].

[73] M. Kawasaki, K. Kohri, and T. Moroi, *Hadronic decay of late - decaying particles and Big-Bang Nucleosynthesis*, *Phys. Lett. B* **625** (2005) 7–12, [astro-ph/0402490].

[74] Y. I. Izotov, T. X. Thuan, and G. Stasinska, *The primordial abundance of He-4: A self-consistent empirical analysis of systematic effects in a large sample of low-metallicity HII regions*, *Astrophys. J.* **662** (2007) 15–38, [astro-ph/0702072].

[75] J. Hisano, M. Kawasaki, K. Kohri, T. Moroi, and K. Nakayama, *Cosmic rays from dark matter annihilation and big-bang nucleosynthesis*, *Phys. Rev. D* **79** (Apr, 2009) 083522.

[76] K. Ishiwata, M. Kawasaki, K. Kohri, and T. Moroi, *Right-handed sneutrino dark matter and big-bang nucleosynthesis*, *Phys. Lett. B* **689** (2010) 163–168, [arXiv:0912.0781].

[77] K. Jedamzik, *Did something decay, evaporate, or annihilate during Big Bang nucleosynthesis?*, *Phys. Rev. D* **70** (2004) 063524, [astro-ph/0402344].

[78] N. Arkani-Hamed, D. P. Finkbeiner, T. R. Slatyer, and N. Weiner, *A Theory of Dark Matter*, *Phys. Rev. D* **79** (2009) 015014, [arXiv:0810.0713].

[79] J. Edsjo and P. Gondolo, *Neutralino relic density including coannihilations*, *Phys. Rev. D* **56** (1997) 1879–1894, [hep-ph/9704361].

[80] T. Han and R. Hempfling, *Messenger sneutrinos as cold dark matter*, *Phys. Lett. B* **415** (1997) 161–169, [hep-ph/9708264].

[81] L. J. Hall, T. Moroi, and H. Murayama, *Sneutrino cold dark matter with lepton number violation*, *Phys. Lett. B* **424** (1998) 305–312, [`hep-ph/9712515`].

[82] F. Chen, J. M. Cline, and A. R. Frey, *A New twist on excited dark matter: Implications for INTEGRAL, PAMELA/ATIC/PPB-BETS, DAMA*, *Phys. Rev. D* **79** (2009) 063530, [`arXiv:0901.4327`].

[83] D. P. Finkbeiner, T. R. Slatyer, N. Weiner, and I. Yavin, *PAMELA, DAMA, INTEGRAL and Signatures of Metastable Excited WIMPs*, *JCAP* **09** (2009) 037, [`arXiv:0903.1037`].

[84] K. R. Dienes, J. Kumar, B. Thomas, and D. Yaylali, *Dark-Matter Decay as a Complementary Probe of Multicomponent Dark Sectors*, *Phys. Rev. Lett.* **114** (2015), no. 5 051301, [`arXiv:1406.4868`].

[85] M. Pospelov and A. Ritz, *The galactic 511 keV line from electroweak scale WIMPs*, *Phys. Lett. B* **651** (2007) 208–215, [`hep-ph/0703128`].

[86] J. Knodlseder et al., *Early SPI / INTEGRAL contraints on the morphology of the 511 keV line emission in the 4th galactic quadrant*, *Astron. Astrophys.* **411** (2003) L457–L460, [`astro-ph/0309442`].

[87] P. Jean et al., *Early SPI / INTEGRAL measurements of 511 keV line emission from the 4th quadrant of the Galaxy*, *Astron. Astrophys.* **407** (2003) L55, [`astro-ph/0309484`].

[88] N. F. Bell, A. J. Galea, and R. R. Volkas, *A Model For Late Dark Matter Decay*, *Phys. Rev. D* **83** (2011) 063504, [`arXiv:1012.0067`].

[89] J. Diemand, M. Kuhlen, and P. Madau, *Dark matter substructure and gamma-ray annihilation in the Milky Way halo*, *Astrophys. J.* **657** (2007) 262–270, [`astro-ph/0611370`].

[90] B. Moore, T. R. Quinn, F. Governato, J. Stadel, and G. Lake, *Cold collapse and the core catastrophe*, *Mon. Not. Roy. Astron. Soc.* **310** (1999) 1147–1152, [`astro-ph/9903164`].

[91] J. F. Navarro, E. Hayashi, C. Power, A. Jenkins, C. S. Frenk, S. D. M. White, V. Springel, J. Stadel, and T. R. Quinn, *The Inner structure of Lambda-CDM halos*

3: *Universality and asymptotic slopes*, *Mon. Not. Roy. Astron. Soc.* **349** (2004) 1039, [astro-ph/0311231].

[92] G. Gentile, P. Salucci, U. Klein, D. Vergani, and P. Kalberla, *The Cored distribution of dark matter in spiral galaxies*, *Mon. Not. Roy. Astron. Soc.* **351** (2004) 903, [astro-ph/0403154].

[93] P. Salucci, A. Lapi, C. Tonini, G. Gentile, I. Yegorova, and U. Klein, *The Universal Rotation Curve of Spiral Galaxies. 2. The Dark Matter Distribution out to the Virial Radius*, *Mon. Not. Roy. Astron. Soc.* **378** (2007) 41–47, [astro-ph/0703115].

[94] E. Bulbul, M. Markevitch, A. Foster, R. K. Smith, M. Loewenstein, and S. W. Randall, *Detection of An Unidentified Emission Line in the Stacked X-ray spectrum of Galaxy Clusters*, *Astrophys. J.* **789** (2014) 13, [arXiv:1402.2301].

[95] N. Cappelluti, E. Bulbul, A. Foster, P. Natarajan, M. C. Urry, M. W. Bautz, F. Civano, E. Miller, and R. K. Smith, *Searching for the 3.5 keV Line in the Deep Fields with Chandra: the 10 Ms observations*, *Astrophys. J.* **854** (2018), no. 2 179, [arXiv:1701.07932].

[96] **Super-Kamiokande** Collaboration, H. Nishino et al., *Search for Proton Decay via p —> e+ pi0 and p —> mu+ pi0 in a Large Water Cherenkov Detector*, *Phys. Rev. Lett.* **102** (2009) 141801, [arXiv:0903.0676].

[97] T. Banks and N. Seiberg, *Symmetries and Strings in Field Theory and Gravity*, *Phys. Rev. D* **83** (2011) 084019, [arXiv:1011.5120].

[98] Y. Mambrini, S. Profumo, and F. S. Queiroz, *Dark Matter and Global Symmetries*, *Phys. Lett.* **B760** (2016) 807–815, [arXiv:1508.06635].

[99] D. Harlow and H. Ooguri, *Constraints on Symmetries from Holography*, *Phys. Rev. Lett.* **122** (2019), no. 19 191601, [arXiv:1810.05337].

[100] R. D. Peccei and H. R. Quinn, CP *conservation in the presence of pseudoparticles*, *Phys. Rev. Lett.* **38** (Jun, 1977) 1440–1443.

[101] F. D. Steffen, *Dark Matter Candidates - Axions, Neutralinos, Gravitinos, and Axinos*, *Eur. Phys. J. C* **59** (2009) 557–588, [arXiv:0811.3347].

[102] M. S. Turner, *Cosmic and local mass density of "invisible" axions*, *Phys. Rev. D* **33** (Feb, 1986) 889–896.

[103] G. G. Raffelt, *Stars as laboratories for fundamental physics: The astrophysics of neutrinos, axions, and other weakly interacting particles.* 5, 1996.

[104] L. Covi, H.-B. Kim, J. E. Kim, and L. Roszkowski, *Axinos as dark matter*, *JHEP* **05** (2001) 033, [hep-ph/0101009].

[105] L. Covi, J. E. Kim, and L. Roszkowski, *Axinos as cold dark matter*, *Phys. Rev. Lett.* **82** (1999) 4180–4183, [hep-ph/9905212].

[106] M. Bolz, W. Buchmuller, and M. Plumacher, *Baryon asymmetry and dark matter*, *Phys. Lett. B* **443** (1998) 209–213, [hep-ph/9809381].

[107] D. Gorbunov, A. Khmelnitsky, and V. Rubakov, *Is gravitino still a warm dark matter candidate?*, *JHEP* **12** (2008) 055, [arXiv:0805.2836].

[108] P. Dey, B. Mukhopadhyaya, S. Roy, and S. K. Vempati, *Constraints on Axino Warm Dark Matter from X-Ray Observation at the Chandra Telescope and SPI*, *JCAP* **05** (2012) 042, [arXiv:1108.1368].

[109] L. Covi and J. E. Kim, *Axinos as Dark Matter Particles*, *New J. Phys.* **11** (2009) 105003, [arXiv:0902.0769].

[110] F. Takayama and M. Yamaguchi, *Gravitino dark matter without R-parity*, *Phys. Lett. B* **485** (2000) 388–392, [hep-ph/0005214].

[111] A. Ibarra, D. Tran, and C. Weniger, *Indirect Searches for Decaying Dark Matter*, *Int. J. Mod. Phys. A* **28** (2013) 1330040, [arXiv:1307.6434].

[112] J. F. Navarro, C. S. Frenk, and S. D. M. White, *The Structure of cold dark matter halos*, *Astrophys. J.* **462** (1996) 563–575, [astro-ph/9508025].

[113] A. W. Graham, D. Merritt, B. Moore, J. Diemand, and B. Terzic, *Empirical models for Dark Matter Halos. I. Nonparametric Construction of Density Profiles and Comparison with Parametric Models*, *Astron. J.* **132** (2006) 2685–2700, [astro-ph/0509417].

[114] J. N. Bahcall and R. M. Soneira, *The Universe at faint magnetidues. 2. Models for the predicted star counts*, *Astrophys. J. Suppl.* **44** (1980) 73–110.

[115] A. Burkert, *The Structure of dark matter halos in dwarf galaxies*, *IAU Symp.* **171** (1996) 175, [`astro-ph/9504041`]. [Astrophys. J.447,L25(1995)].

[116] O. Y. Gnedin, A. V. Kravtsov, A. A. Klypin, and D. Nagai, *Response of dark matter halos to condensation of baryons: Cosmological simulations and improved adiabatic contraction model*, *Astrophys. J.* **616** (2004) 16–26, [`astro-ph/0406247`].

[117] M. Cirelli, G. Corcella, A. Hektor, G. Hutsi, M. Kadastik, P. Panci, M. Raidal, F. Sala, and A. Strumia, *PPPC 4 DM ID: A Poor Particle Physicist Cookbook for Dark Matter Indirect Detection*, *JCAP* **1103** (2011) 051, [`arXiv:1012.4515`]. [Erratum: JCAP1210,E01(2012)].

[118] M. Markevitch, A. H. Gonzalez, D. Clowe, A. Vikhlinin, L. David, W. Forman, C. Jones, S. Murray, and W. Tucker, *Direct constraints on the dark matter self-interaction cross-section from the merging galaxy cluster 1E0657-56*, *Astrophys. J.* **606** (2004) 819–824, [`astro-ph/0309303`].

[119] V. V. Khoze, A. D. Plascencia, and K. Sakurai, *Simplified models of dark matter with a long-lived co-annihilation partner*, *JHEP* **06** (2017) 041, [`arXiv:1702.00750`].

[120] S. Biswas and B. Mukhopadhyaya, *Chargino reconstruction in supersymmetry with long-lived staus*, *Phys. Rev.* **D81** (2010) 015003, [`arXiv:0910.3446`].

[121] S. Biswas and B. Mukhopadhyaya, *Neutralino reconstruction in supersymmetry with long-lived staus*, *Phys. Rev.* **D79** (2009) 115009, [`arXiv:0902.4349`].

[122] J. Heisig and J. Kersten, *Production of long-lived staus in the Drell-Yan process*, *Phys. Rev.* **D84** (2011) 115009, [`arXiv:1106.0764`].

[123] J. Heisig and J. Kersten, *Long-lived staus from strong production in a simplified model approach*, *Phys. Rev.* **D86** (2012) 055020, [`arXiv:1203.1581`].

[124] J. Heisig, J. Kersten, B. Panes, and T. Robens, *A survey for low stau yields in the MSSM*, *JHEP* **04** (2014) 053, [`arXiv:1310.2825`].

[125] J. Heisig, A. Lessa, and L. Quertenmont, *Simplified Models for Exotic BSM Searches*, *JHEP* **12** (2015) 087, [`arXiv:1509.00473`].

[126] S. Banerjee, G. Bélanger, B. Mukhopadhyaya, and P. D. Serpico, *Signatures of sneutrino dark matter in an extension of the CMSSM*, *JHEP* **07** (2016) 095, [`arXiv:1603.08834`].

[127] A. Abada, C. Biggio, F. Bonnet, M. B. Gavela, and T. Hambye, *Low energy effects of neutrino masses*, *JHEP* **12** (2007) 061, [arXiv:0707.4058].

[128] A. Abada, C. Biggio, F. Bonnet, M. B. Gavela, and T. Hambye, *mu → e gamma and tau → l gamma decays in the fermion triplet seesaw model*, *Phys. Rev.* **D78** (2008) 033007, [arXiv:0803.0481].

[129] C. Biggio and F. Bonnet, *Implementation of the Type III Seesaw Model in FeynRules/MadGraph and Prospects for Discovery with Early LHC Data*, *Eur. Phys. J.* **C72** (2012) 1899, [arXiv:1107.3463].

[130] P. Gondolo and G. Gelmini, *Cosmic abundances of stable particles: Improved analysis*, *Nucl. Phys.* **B360** (1991) 145–179.

[131] A. Biswas and A. Gupta, *Freeze-in Production of Sterile Neutrino Dark Matter in $U(1)_{B-L}$ Model*, *JCAP* **1609** (2016), no. 09 044, [arXiv:1607.01469]. [Addendum: JCAP1705,no.05,A01(2017)].

[132] **CMS** Collaboration, *Search for heavy stable charged particles with* 12.9 fb^{-1} *of 2016 data*, Tech. Rep. CMS-PAS-EXO-16-036, CERN, Geneva, 2016.

[133] E. Ma, *Verifiable radiative seesaw mechanism of neutrino mass and dark matter*, *Phys. Rev.* **D73** (2006) 077301, [hep-ph/0601225].

[134] N. Chakrabarty, D. K. Ghosh, B. Mukhopadhyaya, and I. Saha, *Dark matter, neutrino masses and high scale validity of an inert Higgs doublet model*, *Phys. Rev.* **D92** (2015), no. 1 015002, [arXiv:1501.03700].

[135] D. Borah and A. Gupta, *A New Viable Region of Inert Higgs Doublet Dark Matter Model with Scotogenic Extension*, arXiv:1706.05034.

[136] E. Molinaro, C. E. Yaguna, and O. Zapata, *FIMP realization of the scotogenic model*, *JCAP* **1407** (2014) 015, [arXiv:1405.1259].

[137] M. Sher, *Electroweak Higgs Potentials and Vacuum Stability*, *Phys. Rept.* **179** (1989) 273–418.

[138] S. Nie and M. Sher, *Vacuum stability bounds in the two Higgs doublet model*, *Phys. Lett.* **B449** (1999) 89–92, [hep-ph/9811234].

[139] P. M. Ferreira, R. Santos, and A. Barroso, *Stability of the tree-level vacuum in two Higgs doublet models against charge or CP spontaneous violation*, *Phys. Lett.* **B603** (2004) 219–229, [`hep-ph/0406231`]. [Erratum: Phys. Lett.B629,114(2005)].

[140] G. C. Branco, P. M. Ferreira, L. Lavoura, M. N. Rebelo, M. Sher, and J. P. Silva, *Theory and phenomenology of two-Higgs-doublet models*, *Phys. Rept.* **516** (2012) 1–102, [`arXiv:1106.0034`].

[141] A. Alloul, N. D. Christensen, C. Degrande, C. Duhr, and B. Fuks, *FeynRules 2.0 - A complete toolbox for tree-level phenomenology*, *Comput. Phys. Commun.* **185** (2014) 2250–2300, [`arXiv:1310.1921`].

[142] J. Alwall, R. Frederix, S. Frixione, V. Hirschi, F. Maltoni, O. Mattelaer, H. S. Shao, T. Stelzer, P. Torrielli, and M. Zaro, *The automated computation of tree-level and next-to-leading order differential cross sections, and their matching to parton shower simulations*, *JHEP* **07** (2014) 079, [`arXiv:1405.0301`].

[143] T. Sjostrand, S. Mrenna, and P. Z. Skands, *PYTHIA 6.4 Physics and Manual*, *JHEP* **05** (2006) 026, [`hep-ph/0603175`].

[144] **DELPHES 3** Collaboration, J. de Favereau, C. Delaere, P. Demin, A. Giammanco, V. Lemaître, A. Mertens, and M. Selvaggi, *DELPHES 3, A modular framework for fast simulation of a generic collider experiment*, *JHEP* **02** (2014) 057, [`arXiv:1307.6346`].

[145] J. Pumplin, D. R. Stump, J. Huston, H. L. Lai, P. M. Nadolsky, and W. K. Tung, *New generation of parton distributions with uncertainties from global QCD analysis*, *JHEP* **07** (2002) 012, [`hep-ph/0201195`].

[146] S. Catani, L. Cieri, G. Ferrera, D. de Florian, and M. Grazzini, *Vector boson production at hadron colliders: a fully exclusive QCD calculation at NNLO*, *Phys. Rev. Lett.* **103** (2009) 082001, [`arXiv:0903.2120`].

[147] C. Muselli, M. Bonvini, S. Forte, S. Marzani, and G. Ridolfi, *Top Quark Pair Production beyond NNLO*, *JHEP* **08** (2015) 076, [`arXiv:1505.02006`].

[148] J. M. Campbell, R. K. Ellis, and C. Williams, *Vector boson pair production at the LHC*, *JHEP* **07** (2011) 018, [`arXiv:1105.0020`].

[149] J. M. Campbell and R. K. Ellis, *$t\bar{t}W^{+-}$ production and decay at NLO*, *JHEP* **07** (2012) 052, [arXiv:1204.5678].

[150] **ATLAS** Collaboration, *Measurement of W and Z Boson Production Cross Sections in pp Collisions at root s = 13 TeV in the ATLAS Detector*, Tech. Rep. ATLAS-CONF-2015-039, CERN, Geneva, Aug, 2015.

[151] R. Ruiz, *QCD Corrections to Pair Production of Type III Seesaw Leptons at Hadron Colliders*, *JHEP* **12** (2015) 165, [arXiv:1509.05416].

[152] B. Fuks and R. Ruiz, *A comprehensive framework for studying W' and Z' bosons at hadron colliders with automated jet veto resummation*, *JHEP* **05** (2017) 032, [arXiv:1701.05263].

[153] M. Muhlleitner and M. Spira, *A Note on doubly charged Higgs pair production at hadron colliders*, *Phys. Rev.* **D68** (2003) 117701, [hep-ph/0305288].

[154] R. Essig, J. Mardon, and T. Volansky, *Direct Detection of Sub-GeV Dark Matter*, *Phys. Rev.* **D85** (2012) 076007, [arXiv:1108.5383].

[155] J. Alexander et al., *Dark Sectors 2016 Workshop: Community Report*, 2016. arXiv:1608.08632.

[156] **SENSEI** Collaboration, M. Crisler, R. Essig, J. Estrada, G. Fernandez, J. Tiffenberg, M. Sofo haro, T. Volansky, and T.-T. Yu, *SENSEI: First Direct-Detection Constraints on sub-GeV Dark Matter from a Surface Run*, arXiv:1804.00088.

[157] T. Asaka, K. Ishiwata, and T. Moroi, *Right-handed sneutrino as cold dark matter*, *Phys. Rev.* **D73** (2006) 051301, [hep-ph/0512118].

[158] T. Asaka, K. Ishiwata, and T. Moroi, *Right-handed sneutrino as cold dark matter of the universe*, *Phys. Rev.* **D75** (2007) 065001, [hep-ph/0612211].

[159] T. Falk, K. A. Olive, and M. Srednicki, *Heavy sneutrinos as dark matter*, *Phys. Lett.* **B339** (1994) 248–251, [hep-ph/9409270].

[160] C. Arina and N. Fornengo, *Sneutrino cold dark matter, a new analysis: Relic abundance and detection rates*, *JHEP* **11** (2007) 029, [arXiv:0709.4477].

[161] **PandaX-II** Collaboration, A. Tan et al., *Dark Matter Results from First 98.7 Days of Data from the PandaX-II Experiment*, *Phys. Rev. Lett.* **117** (2016), no. 12 121303, [arXiv:1607.07400].

[162] M. Chala, A. Delgado, G. Nardini, and M. Quiros, *A light sneutrino rescues the light stop*, *JHEP* **04** (2017) 097, [arXiv:1702.07359].

[163] F. Capozzi, E. Lisi, A. Marrone, and A. Palazzo, *Current unknowns in the three neutrino framework*, arXiv:1804.09678.

[164] S. P. Martin, *A Supersymmetry primer*, hep-ph/9709356. [Adv. Ser. Direct. High Energy Phys.18,1(1998)].

[165] G. Belanger, S. Kraml, and A. Lessa, *Light Sneutrino Dark Matter at the LHC*, *JHEP* **07** (2011) 083, [arXiv:1105.4878].

[166] B. Dumont, G. Belanger, S. Fichet, S. Kraml, and T. Schwetz, *Mixed sneutrino dark matter in light of the 2011 XENON and LHC results*, *JCAP* **1209** (2012) 013, [arXiv:1206.1521].

[167] S. Banerjee, P. S. B. Dev, S. Mondal, B. Mukhopadhyaya, and S. Roy, *Invisible Higgs Decay in a Supersymmetric Inverse Seesaw Model with Light Sneutrino Dark Matter*, *JHEP* **10** (2013) 221, [arXiv:1306.2143].

[168] C. Arina, M. E. C. Catalan, S. Kraml, S. Kulkarni, and U. Laa, *Constraints on sneutrino dark matter from LHC Run 1*, *JHEP* **05** (2015) 142, [arXiv:1503.02960].

[169] W. Abdallah, A. Hammad, A. Kasem, and S. Khalil, *Long-Lived BLSSM Particles at the LHC*, arXiv:1804.09778.

[170] I. Hinchliffe and F. E. Paige, *Measurements in gauge mediated SUSY breaking models at CERN LHC*, *Phys. Rev.* **D60** (1999) 095002, [hep-ph/9812233].

[171] A. Chatterjee, N. Chakrabarty, and B. Mukhopadhyaya, *Same-sign trileptons as a signal of sneutrino lightest supersymmetric partlcle*, *Phys. Lett.* **B754** (2016) 14–17, [arXiv:1411.7226].

[172] S. Biswas, *Reconstruction of the left-chiral tau-sneutrino in supersymmetry with a right-sneutrino as the lightest supersymmetric particle*, *Phys. Rev.* **D82** (2010) 075020, [arXiv:1002.4395].

[173] C. G. Lester and D. J. Summers, *Measuring masses of semiinvisibly decaying particles pair produced at hadron colliders*, *Phys. Lett.* **B463** (1999) 99–103, [hep-ph/9906349].

[174] A. Barr, C. Lester, and P. Stephens, *m(T2): The Truth behind the glamour*, *J. Phys.* **G29** (2003) 2343–2363, [hep-ph/0304226].

[175] M. Lattanzi and M. Gerbino, *Status of neutrino properties and future prospects - Cosmological and astrophysical constraints*, *Front.in Phys.* **5** (2018) 70, [arXiv:1712.07109].

[176] **MSSM Working Group** Collaboration, A. Djouadi et al., *The Minimal supersymmetric standard model: Group summary report*, hep-ph/9901246.

[177] G. Bélanger, F. Boudjema, A. Pukhov, and A. Semenov, *microMEGAs4.1: two dark matter candidates*, *Comput. Phys. Commun.* **192** (2015) 322–329, [arXiv:1407.6129].

[178] J. McDonald, *Thermally generated gauge singlet scalars as selfinteracting dark matter*, *Phys. Rev. Lett.* **88** (2002) 091304, [hep-ph/0106249].

[179] **ATLAS** Collaboration, M. Aaboud et al., *Measurement of the Higgs boson mass in the $H \to ZZ^* \to 4\ell$ and $H \to \gamma\gamma$ channels with $\sqrt{s} = 13$ TeV pp collisions using the ATLAS detector*, arXiv:1806.00242.

[180] **ATLAS, CMS** Collaboration, G. Aad et al., *Combined Measurement of the Higgs Boson Mass in pp Collisions at $\sqrt{s} = 7$ and 8 TeV with the ATLAS and CMS Experiments*, *Phys. Rev. Lett.* **114** (2015) 191803, [arXiv:1503.07589].

[181] **CMS** Collaboration, V. Khachatryan et al., *Precise determination of the mass of the Higgs boson and tests of compatibility of its couplings with the standard model predictions using proton collisions at 7 and 8 TeV*, *Eur. Phys. J.* **C75** (2015), no. 5 212, [arXiv:1412.8662].

[182] **ATLAS** Collaboration, G. Aad et al., *Measurements of the Higgs boson production and decay rates and coupling strengths using pp collision data at $\sqrt{s} = 7$ and 8 TeV in the ATLAS experiment*, *Eur. Phys. J.* **C76** (2016), no. 1 6, [arXiv:1507.04548].

[183] J. Bernon and B. Dumont, *Lilith: a tool for constraining new physics from Higgs measurements*, *Eur. Phys. J.* **C75** (2015), no. 9 440, [arXiv:1502.04138].

[184] P. Bechtle, O. Brein, S. Heinemeyer, O. Stal, T. Stefaniak, G. Weiglein, and k. E. Williams, HiggsBounds − 4: *Improved Tests of Extended Higgs Sectors against Exclusion Bounds from LEP, the Tevatron and the LHC*, Eur. Phys. J. C **74** (2014), no. 3 2693, [arXiv:1311.0055].

[185] M. Kawasaki, K. Kohri, and T. Moroi, *Big-Bang nucleosynthesis and hadronic decay of long-lived massive particles*, Phys. Rev. **D71** (2005) 083502, [astro-ph/0408426].

[186] M. Kawasaki, K. Kohri, T. Moroi, and Y. Takaesu, *Revisiting Big-Bang Nucleosynthesis Constraints on Long-Lived Decaying Particles*, Phys. Rev. **D97** (2018), no. 2 023502, [arXiv:1709.01211].

[187] **ATLAS** Collaboration, M. Aaboud et al., *Search for squarks and gluinos in final states with jets and missing transverse momentum using 36 fb^{-1} of $\sqrt{s}$=13 TeV pp collision data with the ATLAS detector*, arXiv:1712.02332.

[188] **CMS** Collaboration, A. M. Sirunyan et al., *Search for new phenomena with the M_{T2} variable in the all-hadronic final state produced in proton–proton collisions at $\sqrt{s} = 13$ TeV*, Eur. Phys. J. **C77** (2017), no. 10 710, [arXiv:1705.04650].

[189] D. L. Rainwater, D. Zeppenfeld, and K. Hagiwara, *Searching for $H \rightarrow \tau^+\tau^-$ in weak boson fusion at the CERN LHC*, Phys. Rev. **D59** (1998) 014037, [hep-ph/9808468].

[190] P. Konar, K. Kong, K. T. Matchev, and M. Park, *Dark Matter Particle Spectroscopy at the LHC: Generalizing M(T2) to Asymmetric Event Topologies*, JHEP **04** (2010) 086, [arXiv:0911.4126].

[191] M. L. Mangano, M. Moretti, F. Piccinini, and M. Treccani, *Matching matrix elements and shower evolution for top-quark production in hadronic collisions*, JHEP **01** (2007) 013, [hep-ph/0611129].

[192] T. Sjöstrand, S. Ask, J. R. Christiansen, R. Corke, N. Desai, P. Ilten, S. Mrenna, S. Prestel, C. O. Rasmussen, and P. Z. Skands, *An Introduction to PYTHIA 8.2*, Comput. Phys. Commun. **191** (2015) 159–177, [arXiv:1410.3012].

[193] M. Cacciari, G. P. Salam, and G. Soyez, *The Anti-k(t) jet clustering algorithm*, JHEP **04** (2008) 063, [arXiv:0802.1189].

[194] M. Cacciari, G. P. Salam, and G. Soyez, *FastJet User Manual*, Eur. Phys. J. **C72** (2012) 1896, [arXiv:1111.6097].

143

[195] R. D. Ball et al., *Parton distributions with LHC data, Nucl. Phys.* **B867** (2013) 244–289, [arXiv:1207.1303].

[196] W. Beenakker, R. Hopker, and M. Spira, *PROSPINO: A Program for the production of supersymmetric particles in next-to-leading order QCD*, hep-ph/9611232.

[197] *Reconstruction, Energy Calibration, and Identification of Hadronically Decaying Tau Leptons in the ATLAS Experiment for Run-2 of the LHC*, Tech. Rep. ATL-PHYS-PUB-2015-045, CERN, Geneva, Nov, 2015.

[198] **MoEDAL** Collaboration, N. E. Mavromatos and V. A. Mitsou, *Physics reach of MoEDAL at LHC: magnetic monopoles, supersymmetry and beyond, EPJ Web Conf.* **164** (2017) 04001, [arXiv:1612.07012].

[199] **MoEDAL** Collaboration, B. Acharya et al., *The Physics Programme Of The MoEDAL Experiment At The LHC, Int. J. Mod. Phys.* **A29** (2014) 1430050, [arXiv:1405.7662].

[200] A. Ghosh, T. Mondal, and B. Mukhopadhyaya, *Right sneutrino with $\Delta L = 2$ masses as nonthermal dark matter, Phys. Rev.* **D99** (2019), no. 3 035018, [arXiv:1807.04964].

[201] M. Srednicki, S. Theisen, and J. Silk, *Cosmic Quarkonium: A Probe of Dark Matter, Phys. Rev. Lett.* **56** (1986) 263. [Erratum: Phys. Rev. Lett.56,1883(1986)].

[202] L. Bergstrom and H. Snellman, *Observable Monochromatic Photons From Cosmic Photino Annihilation, Phys. Rev.* **D37** (1988) 3737–3741.

[203] L. Bergstrom, *Radiative Processes in Dark Matter Photino Annihilation, Phys. Lett.* **B225** (1989) 372–380.

[204] R. Flores, K. A. Olive, and S. Rudaz, *Radiative Processes in Lsp Annihilation, Phys. Lett.* **B232** (1989) 377–382.

[205] T. Bringmann, L. Bergstrom, and J. Edsjo, *New Gamma-Ray Contributions to Supersymmetric Dark Matter Annihilation, JHEP* **01** (2008) 049, [arXiv:0710.3169].

[206] C. Garcia-Cely and A. Ibarra, *Novel Gamma-ray Spectral Features in the Inert Doublet Model, JCAP* **1309** (2013) 025, [arXiv:1306.4681].

[207] P. B. Pal and L. Wolfenstein, *Radiative Decays of Massive Neutrinos*, *Phys. Rev.* **D25** (1982) 766.

[208] A. Ibarra, A. S. Lamperstorfer, and J. Silk, *Dark matter annihilations and decays after the AMS-02 positron measurements*, *Phys. Rev.* **D89** (2014), no. 6 063539, [`arXiv:1309.2570`].

[209] C. El Aisati, M. Gustafsson, and T. Hambye, *New Search for Monochromatic Neutrinos from Dark Matter Decay*, *Phys. Rev.* **D92** (2015), no. 12 123515, [`arXiv:1506.02657`].

[210] L. Canetti, M. Drewes, T. Frossard, and M. Shaposhnikov, *Dark Matter, Baryogenesis and Neutrino Oscillations from Right Handed Neutrinos*, *Phys. Rev.* **D87** (2013) 093006, [`arXiv:1208.4607`].

[211] M. Garny, A. Ibarra, D. Tran, and C. Weniger, *Gamma-Ray Lines from Radiative Dark Matter Decay*, *JCAP* **1101** (2011) 032, [`arXiv:1011.3786`].

[212] R. Essig, E. Kuflik, S. D. McDermott, T. Volansky, and K. M. Zurek, *Constraining Light Dark Matter with Diffuse X-Ray and Gamma-Ray Observations*, *JHEP* **11** (2013) 193, [`arXiv:1309.4091`].

[213] V. Silveira and A. Zee, *SCALAR PHANTOMS*, *Phys. Lett.* **161B** (1985) 136–140.

[214] J. McDonald, *Gauge singlet scalars as cold dark matter*, *Phys. Rev.* **D50** (1994) 3637–3649, [`hep-ph/0702143`].

[215] C. E. Yaguna, *The Singlet Scalar as FIMP Dark Matter*, *JHEP* **08** (2011) 060, [`arXiv:1105.1654`].

[216] J. F. Navarro, C. S. Frenk, and S. D. M. White, *A Universal density profile from hierarchical clustering*, *Astrophys. J.* **490** (1997) 493–508, [`astro-ph/9611107`].

[217] L. Bouchet, E. Jourdain, J. P. Roques, A. Strong, R. Diehl, F. Lebrun, and R. Terrier, *INTEGRAL SPI All-Sky View in Soft Gamma Rays: Study of Point Source and Galactic Diffuse Emissions*, *Astrophys. J.* **679** (2008) 1315, [`arXiv:0801.2086`].

[218] G. Weidenspointner, M. Varendorff, K. Bennett, H. Bloemen, W. Hermsen, S. C. Kappadath, G. G. Lichti, J. Ryan, and V. Schönfelder, *The Cdg Spectrum from 0.8-30*

MeV Measured with COMPTEL Based on a Physical Model of the Instrumental Background, Astrophysical Letters and Communications **39** (Jan, 1999) 193.

[219] A. W. Strong, I. V. Moskalenko, and O. Reimer, *Diffuse galactic continuum gamma rays. A Model compatible with EGRET data and cosmic-ray measurements*, Astrophys. J. **613** (2004) 962–976, [astro-ph/0406254].

[220] **Fermi-LAT** Collaboration, M. Ackermann et al., *The spectrum of isotropic diffuse gamma-ray emission between 100 MeV and 820 GeV*, Astrophys. J. **799** (2015) 86, [arXiv:1410.3696].

[221] T. Asaka, K. Ishiwata, and T. Moroi, *Right-handed sneutrino as cold dark matter of the universe*, AIP Conf. Proc. **903** (2007) 16–23. [,16(2007)].

[222] S. Gopalakrishna, A. de Gouvea, and W. Porod, *Right-handed sneutrinos as nonthermal dark matter*, JCAP **0605** (2006) 005, [hep-ph/0602027].

[223] S. Banerjee, G. Bélanger, A. Ghosh, and B. Mukhopadhyaya, *Long-lived stau, sneutrino dark matter and right-slepton spectrum*, JHEP **09** (2018) 143, [arXiv:1806.04488].

[224] K.-Y. Choi, J. Kim, and O. Seto, *Thermal production of light Dirac right-handed sneutrino dark matter*, Phys. Dark Univ. **22** (2018) 96–100, [arXiv:1808.00764].

[225] F. Gabbiani, E. Gabrielli, A. Masiero, and L. Silvestrini, *A Complete analysis of FCNC and CP constraints in general SUSY extensions of the standard model*, Nucl. Phys. **B477** (1996) 321–352, [hep-ph/9604387].

[226] G. D'Ambrosio, G. F. Giudice, G. Isidori, and A. Strumia, *Minimal flavor violation: An Effective field theory approach*, Nucl. Phys. **B645** (2002) 155–187, [hep-ph/0207036].

[227] M. Antonelli et al., *Flavor Physics in the Quark Sector*, Phys. Rept. **494** (2010) 197–414, [arXiv:0907.5386].

[228] A. J. Buras, M. V. Carlucci, S. Gori, and G. Isidori, *Higgs-mediated FCNCs: Natural Flavour Conservation vs. Minimal Flavour Violation*, JHEP **10** (2010) 009, [arXiv:1005.5310].

[229] A. Cuoco, J. Heisig, M. Korsmeier, and M. Krämer, *Constraining heavy dark matter with cosmic-ray antiprotons*, *JCAP* **1804** (2018) 004, [arXiv:1711.05274].

[230] **Fermi-LAT** Collaboration, M. Ackermann et al., *The Fermi Galactic Center GeV Excess and Implications for Dark Matter*, *Astrophys. J.* **840** (2017), no. 1 43, [arXiv:1704.03910].

[231] M. Regis, L. Richter, and S. Colafrancesco, *Dark matter in the Reticulum II dSph: a radio search*, *JCAP* **1707** (2017), no. 07 025, [arXiv:1703.09921].

[232] A. Natarajan, J. B. Peterson, T. C. Voytek, K. Spekkens, B. Mason, J. Aguirre, and B. Willman, *Bounds on Dark Matter Properties from Radio Observations of Ursa Major II using the Green Bank Telescope*, *Phys. Rev.* **D88** (2013) 083535, [arXiv:1308.4979].

[233] C. Blanco and D. Hooper, *Constraints on Decaying Dark Matter from the Isotropic Gamma-Ray Background*, *JCAP* **1903** (2019), no. 03 019, [arXiv:1811.05988].

[234] **AMS** Collaboration, M. Aguilar et al., *Precision Measurement of the Proton Flux in Primary Cosmic Rays from Rigidity 1 GV to 1.8 TV with the Alpha Magnetic Spectrometer on the International Space Station*, *Phys. Rev. Lett.* **114** (2015) 171103.

[235] **AMS** Collaboration, M. Aguilar et al., *Electron and Positron Fluxes in Primary Cosmic Rays Measured with the Alpha Magnetic Spectrometer on the International Space Station*, *Phys. Rev. Lett.* **113** (2014) 121102.

[236] **H.E.S.S.** Collaboration, A. Abramowski et al., *Diffuse Galactic gamma-ray emission with H.E.S.S*, *Phys. Rev.* **D90** (2014), no. 12 122007, [arXiv:1411.7568].

[237] **H.E.S.S.** Collaboration, A. Abramowski et al., *Search for dark matter annihilation signatures in H.E.S.S. observations of Dwarf Spheroidal Galaxies*, *Phys. Rev.* **D90** (2014) 112012, [arXiv:1410.2589].

[238] **IceCube** Collaboration, M. G. Aartsen et al., *Search for neutrinos from decaying dark matter with IceCube*, *Eur. Phys. J.* **C78** (2018), no. 10 831, [arXiv:1804.03848].

[239] D. J. H. Chung, E. W. Kolb, and A. Riotto, *Superheavy dark matter*, *Phys. Rev. D* **59** (Nov, 1998) 023501.

[240] V. Kuzmin and I. Tkachev, *Ultrahigh-energy cosmic rays, superheavy long living particles, and matter creation after inflation*, *JETP Lett.* **68** (1998) 271–275, [hep-ph/9802304].

[241] V. Kuzmin and I. Tkachev, *Matter creation via vacuum fluctuations in the early universe and observed ultrahigh-energy cosmic ray events*, *Phys. Rev. D* **59** (1999) 123006, [hep-ph/9809547].

[242] E. W. Kolb, D. J. H. Chung, and A. Riotto, *WIMPzillas!*, *AIP Conf. Proc.* **484** (1999), no. 1 91–105, [hep-ph/9810361].

[243] D. J. H. Chung, E. W. Kolb, A. Riotto, and I. I. Tkachev, *Probing Planckian physics: Resonant production of particles during inflation and features in the primordial power spectrum*, *Phys. Rev. D* **62** (2000) 043508, [hep-ph/9910437].

[244] V. A. Kuzmin and I. I. Tkachev, *Ultrahigh-energy cosmic rays and inflation relics*, *Phys. Rept.* **320** (1999) 199–221, [hep-ph/9903542].

[245] D. J. H. Chung, P. Crotty, E. W. Kolb, and A. Riotto, *On the Gravitational Production of Superheavy Dark Matter*, *Phys. Rev. D* **64** (2001) 043503, [hep-ph/0104100].

[246] K. Kannike, A. Racioppi, and M. Raidal, *Super-heavy dark matter – Towards predictive scenarios from inflation*, *Nucl. Phys. B* **918** (2017) 162–177, [arXiv:1605.09378].

[247] M. G. Baring, T. Ghosh, F. S. Queiroz, and K. Sinha, *New Limits on the Dark Matter Lifetime from Dwarf Spheroidal Galaxies using Fermi-LAT*, *Phys. Rev.* **D93** (2016), no. 10 103009, [arXiv:1510.00389].

[248] A. Viana, H. Schoorlemmer, A. Albert, V. de Souza, J. P. Harding, and J. Hinton, *Searching for Dark Matter in the Galactic Halo with a Wide Field of View TeV Gamma-ray Observatory in the Southern Hemisphere*, *JCAP* **1912** (2019), no. 12 061, [arXiv:1906.03353].

[249] R. Braun, A. Bonaldi, T. Bourke, E. Keane, and J. Wagg, *Anticipated performance of the square kilometre array – phase 1 (ska1)*, 2019.

[250] A. Kar, S. Mitra, B. Mukhopadhyaya, and T. R. Choudhury, *Heavy dark matter particle annihilation in dwarf spheroidal galaxies: radio signals at the SKA telescope*, arXiv:1905.11426.

[251] A. Kar, S. Mitra, B. Mukhopadhyaya, and T. R. Choudhury, *Can Square Kilometre Array phase 1 go much beyond the LHC in supersymmetry search?*, *Phys. Rev.* **D99** (2019), no. 2 021302, [arXiv:1808.05793].

[252] T. R. Slatyer, *Indirect Detection of Dark Matter*, in *Proceedings, Theoretical Advanced Study Institute in Elementary Particle Physics : Anticipating the Next Discoveries in Particle Physics (TASI 2016): Boulder, CO, USA, June 6-July 1, 2016*, pp. 297–353, 2018. arXiv:1710.05137.

[253] B. Grzadkowski, M. Iskrzynski, M. Misiak, and J. Rosiek, *Dimension-Six Terms in the Standard Model Lagrangian*, *JHEP* **10** (2010) 085, [arXiv:1008.4884].

[254] A. Ghosh, A. Ibarra, T. Mondal, and B. Mukhopadhyaya, *Gamma-ray signals from multicomponent scalar dark matter decays*, *JCAP* **2001** (2020), no. 01 011, [arXiv:1909.13292].

[255] G. Belanger, F. Boudjema, P. Brun, A. Pukhov, S. Rosier-Lees, P. Salati, and A. Semenov, *Indirect search for dark matter with micrOMEGAs2.4*, *Comput. Phys. Commun.* **182** (2011) 842–856, [arXiv:1004.1092].

[256] J. Bovy, D. W. Hogg, and H.-W. Rix, *Galactic Masers and the Milky Way Circular Velocity*, *Astrophys. J.* **704** (2009) 1704–1709, [arXiv:0907.5423].

[257] S. Gillessen, F. Eisenhauer, S. Trippe, T. Alexander, R. Genzel, F. Martins, and T. Ott, *Monitoring stellar orbits around the Massive Black Hole in the Galactic Center*, *Astrophys. J.* **692** (2009) 1075–1109, [arXiv:0810.4674].

[258] T. A. Porter and A. Strong, *A New estimate of the Galactic interstellar radiation field between 0.1 microns and 1000 microns*, in *29th International Cosmic Ray Conference*, vol. 4, pp. 77–80, 7, 2005. astro-ph/0507119.

[259] T. Delahaye, R. Lineros, F. Donato, N. Fornengo, and P. Salati, *Positrons from dark matter annihilation in the galactic halo: Theoretical uncertainties*, *Phys. Rev. D* **77** (2008) 063527, [arXiv:0712.2312].

[260] F. Donato, N. Fornengo, D. Maurin, and P. Salati, *Antiprotons in cosmic rays from neutralino annihilation*, Phys. Rev. D **69** (2004) 063501, [`astro-ph/0306207`].

[261] M. Cirelli, E. Moulin, P. Panci, P. D. Serpico, and A. Viana, *Gamma ray constraints on Decaying Dark Matter*, Phys. Rev. D **86** (2012) 083506, [`arXiv:1205.5283`].

[262] W. Liu, X.-J. Bi, S.-J. Lin, and P.-F. Yin, *Constraints on dark matter annihilation and decay from the isotropic gamma-ray background*, Chin. Phys. C **41** (2017), no. 4 045104, [`arXiv:1602.01012`].

[263] S. Colafrancesco, S. Profumo, and P. Ullio, *Detecting dark matter WIMPs in the Draco dwarf: A multi-wavelength perspective*, Phys. Rev. **D75** (2007) 023513, [`astro-ph/0607073`].

[264] J. Diemand, M. Zemp, B. Moore, J. Stadel, and M. Carollo, *Cusps in cold dark matter haloes*, Mon. Not. Roy. Astron. Soc. **364** (2005) 665, [`astro-ph/0504215`].

[265] A. Geringer-Sameth, S. M. Koushiappas, and M. Walker, *Dwarf galaxy annihilation and decay emission profiles for dark matter experiments*, Astrophys. J. **801** (2015), no. 2 74, [`arXiv:1408.0002`].

[266] J. Choquette, *Constraining Dwarf Spheroidal Dark Matter Halos With The Galactic Center Excess*, Phys. Rev. **D97** (2018), no. 4 043017, [`arXiv:1705.09676`].

[267] A. Kar, S. Mitra, B. Mukhopadhyaya, T. R. Choudhury, and S. Tingay, *Constraints on dark matter annihilation in dwarf spheroidal galaxies from low frequency radio observations*, [`arXiv:1907.00979`].

[268] G. Beck and S. Colafrancesco, *A Multi-frequency analysis of dark matter annihilation interpretations of recent anti-particle and γ-ray excesses in cosmic structures*, JCAP **1605** (2016), no. 05 013, [`arXiv:1508.01386`].

[269] S. Colafrancesco, S. Profumo, and P. Ullio, *Multi-frequency analysis of neutralino dark matter annihilations in the Coma cluster*, Astron. Astrophys. **455** (2006) 21, [`astro-ph/0507575`].

[270] A. McDaniel, T. Jeltema, S. Profumo, and E. Storm, *Multiwavelength Analysis of Dark Matter Annihilation and RX-DMFIT*, JCAP **09** (2017) 027, [`arXiv:1705.09384`].

[271] K. Spekkens, B. S. Mason, J. E. Aguirre, and B. Nhan, *A Deep Search for Extended Radio Continuum Emission From Dwarf Spheroidal Galaxies: Implications for Particle Dark Matter*, *Astrophys. J.* **773** (2013) 61, [arXiv:1301.5306].

[272] M. Regis, L. Richter, S. Colafrancesco, S. Profumo, W. J. G. de Blok, and M. Massardi, *Local Group dSph radio survey with ATCA – II. Non-thermal diffuse emission*, *Mon. Not. Roy. Astron. Soc.* **448** (2015), no. 4 3747–3765, [arXiv:1407.5482].

[273] **CTA Consortium** Collaboration, M. Actis et al., *Design concepts for the Cherenkov Telescope Array CTA: An advanced facility for ground-based high-energy gamma-ray astronomy*, *Exper. Astron.* **32** (2011) 193–316, [arXiv:1008.3703].

[274] **CTA Consortium** Collaboration, A. Morselli, *The Dark Matter Programme of the Cherenkov Telescope Array*, *PoS* **ICRC2017** (2018) 921, [arXiv:1709.01483]. [35,921(2017)].

[275] K. Griest and M. Kamionkowski, *Unitarity limits on the mass and radius of dark-matter particles*, *Phys. Rev. Lett.* **64** (Feb, 1990) 615–618.

[276] A. Arhrib, R. Benbrik, M. Chabab, G. Moultaka, M. C. Peyranere, L. Rahili, and J. Ramadan, *The Higgs Potential in the Type II Seesaw Model*, *Phys. Rev.* **D84** (2011) 095005, [arXiv:1105.1925].